AVERAGE CURRENT-MODE CONTROL AND CHARGE CONTROL FOR PWM CONVERTERS

by

Wei Tang

Dissertation submitted to the Faculty of the

Virginia Polytechnic Institute and State University

in partial fulfillment of the requirements for the degree of

Doctor of Philosophy

in

Electrical Engineering

APPROVED:

Fred C. Lee

Fred C. Lee , Chairman

Richard A. Arndt

Dusan Borojevic

Dan Chen

Dan Y. Chen

Milan M. Jovanovic

Octerber, 1994

Blacksburg, Virginia

c.2

AVERAGE CURRENT-MODE CONTROL AND CHARGE CONTROL FOR PWM CONVERTERS

by

Wei Tang

Fred C. Lee , Chairman

Electrical Engineering

(ABSTRACT)

Two control schemes for PWM converters, average current-mode (ACM) control and charge control, are studied in this dissertation. The small-signal models are derived for continuous-conduction mode PWM converters employing these two controls. Sampled-data modeling is applied to the current loop modeling, and the obtained models are accurate up to half the switching frequency. The relationships between current loop instability and converter operating conditions for both controls are found for the first time. The derived models are verified by both time-domain simulations and experiments. The models can be used for both voltage loop and current loop analysis and designs. Comprehensive design guidelines for PWM converters with both controls are also provided. The small-signal characteristics of these two controls are compared with those of peak current-mode control.

The applications of ACM control and charge control to power factor correction (PFC) circuits are studied. Charge control is applied to continuous-conduction

mode flyback converter to achieve a single-stage PFC. The current loop instability in PFC circuit and its effect on the input EMI filter design are investigated. The trade-off between the current loop stability margin and line current distortion is also discussed.

Acknowledgements

I would like to express my deep and sincere gratitude for my advisor, Dr. Fred C. Lee for his guidance and support during my doctoral studies and research. I also would like to thank my committee members, Dr. Richard Arndt, Dr. Dusan Borojevic, Dr. Dan Y. Chen, and Dr. Milan M. Jovanovic, for their valuable suggestions and comments on my dissertation.

I would like to express my sincere appreciation to Dr. Raymond B. Ridley for his valuable help during the course of this work.

I thank all my fellow students at Virginia Power Electronics Center and my friends at Virginia Tech., I shall remember you for the good time we spent together.

I thank Ms. Tammy Hiner and Ms. Teresa Shaw for their help and Ms. Joanna Banach for editing this dissertation.

I would also like to thank my former university advisor, Professor X. S. Cai, for his constant encouragement.

I am deeply grateful to my father, Yue Tang, late mother, Yun Huang, and sister, Lily Tang, for their love and support.

Finally, I would like to thank my wife, Dr. Zhujun Li, for her love, support, and understanding, and it is to her this dissertation is dedicated.

This work was supported by Lambda Electronics Inc., Digital Electronics Corp., and the Virginia Center for Innovative Technology.

Table of Contents

List of Illustrations

1. INTRODUCTION

1.1 Background

There are a variety of switching converter control schemes which use the inductor current as the control signal, and all of them could be considered current-mode controls [1-11]. Current-mode controls have many advantages over voltage-mode control, such as good dynamic performance, inherent current limiting, and current sharing abilities.

One of the earlier current-mode control schemes is the peak current-mode (PCM) control [1,2]. It uses the peak inductor current as the feedback control

signal. In the control implementation, the switch current is sensed instead of the inductor current, since for PWM converter the peak switch current is equal to the peak inductor current, and sensing the switch current is easier and more efficient than sensing the inductor current. Many efforts have been made to analyze and design this control, which makes it the most popular current-mode control scheme. PCM control is often used to improve the dynamic performance of dc-dc converter as well as provide peak current limiting and sharing functions. One main drawback of PCM control is the poor noise immunity in the current sensing loop, which disturbs the normal operation of the system if no precaution is taken.

Standardized control module (SCM) control [3,4,5] feedbacks the ac ripple of the inductor current by integrating the voltage across the inductor. It achieves the same dynamic performance as PCM control, and the switching noise is eliminated by the integrator in the feedback loop. But the overcurrent protection and the current sharing ability are diminished, since the feedback signal does not include the peak or average inductor current information.

Average current-mode (ACM) control [6,8] utilizes the average inductor current as the control signal. In order to obtain the average inductor current, an integrator-lead network (current compensator) is added to the inductor current feedback loop. The duty cycle is controlled by the error between the average inductor current and the control voltage. ACM control is useful for applications where the average inductor current needs to be controlled, such

as boost PFC or battery charger control. The switching noise problem in PCM control does not exist in ACM control, since the high-frequency noise is filtered by the current compensator.

The main drawback of ACM control is that the inductor current needs to be sensed. Usually, a resistor is used to sense the inductor current. But if the value of the resistor is large, it introduces excessive power dissipation. If the value of the resistor is too small, the amplitude of the sensed signal is small, which results in low signal-to-noise ratio.

The PWM conductance control [7] has the same function as ACM control. The implementations of these two controls are basically the same, except that the modulator implementations of the two controls are different. ACM control modulates the trailing edge of the PWM pulse, while PWM conductance control modulates both edges of the PWM pulse.

The charge of the inductor current during the on-time or the off-time is another quantity which can be used as the feedback control signal. In [9] the output charge of a boost converter (equal to the charge of the off-time inductor current) is used as the feedback control signal. The implementation of the charge control given in [9] is complicated. It senses the inductor current by a resistor, and the sensed current is processed by an electronic circuit in order to get the needed charge. A simpler implementation of charge control can be found in [10,11]. A current transformer is used to sense the on-time inductor

current, and a capacitor is used to obtain the charge of the sensed current. The capacitor is discharged in every cycle so that the per cycle charge is controlled.

The main feature of charge control is the ability to control the average value of the pulsating currents (switch current or diode current) of a PWM converter. Charge control also has average current sharing and cycle-by-cycle average current limiting abilities. The main drawback of charge control is that its current loop instability is both line- and load-dependent, which limits its application to converters with wide operation ranges.

Up to now, the work on the small-signal modeling of current-mode control has been focused mainly on PCM and SCM controls [12-20]. The small-signal model for PCM control developed by Ridley [17, 18] combines the simplicity of popular continuous-time models and the accuracy of a sampled-data model. The model is accurate up to half the switching frequency, and it can explain all of the observed phenomena of PCM control.

A few results can be found on the small-signal modeling of ACM and charge controls [8,9,21,22]. Most of the approaches are based on the average modeling concept. The low-frequency model of buck converter with PWM conductance control can be found in [21], which reveals the single low-frequency pole characteristic in the control-to-output gain. The average model of PCM control [14] is applied to ACM control in [8]. Since the current

loop gain high-frequency characteristic in [14] is not correct, the current loop gain given by [8] cannot be used to predict the current loop stability of ACM control. The small-signal analysis of charge control by Capel [9] is also focused on voltage loop low-frequency characteristics. It reveals the single low-frequency pole characteristic in the control-to-output voltage transfer function. Since the analysis is based on averaging concept, it cannot predict the current loop instability in charge control. Kislovski studied the current loop stability of charge control in time domain [22]. By comparing the inductor current perturbations in two successive cycles, the current loop stability criterion is found. The obtained results are approximate and numerical (in the form of design curves). They are inconvenient for both analysis and design.

1.2 Motivation and Objective of the Research

ACM control has been widely used in controlling boost PFC circuit and battery charger of the solar array power system. Due to the lack of an accurate small-signal model, the design of the control is far from optimized. The analysis results of PCM control are sometimes used directly for ACM control without any justification [8]. As will be seen later, the small-signal behaviors of ACM control are quite different from those of PCM control. For example, the current loop of PCM control becomes unstable when duty cycle is larger than

fifty percent, while the current loop of ACM control becomes unstable for both small and large duty cycles, if the current compensator is not properly designed. A small-signal model which gives both voltage and current loop small-signal characteristics up to half the switching frequency is needed for designing the control correctly.

Charge control can be used for applications in which the average switch current needs to be controlled, such as buck and flyback PFC circuits. Charge control has not been used as widely as other current-mode controls. One reason for that is the lack of the understanding of its small-signal characteristics. The current loop stability of charge control is both line- and load-dependent. It is impossible to obtain an optimum design without knowing the small-signal characteristics of the control.

The objective of the research is to conduct a complete study for both ACM and charge controls. The small-signal modeling technique for PCM control devised by Ridley can be used to derive the complete small-signal models for both ACM and charge controls. The emphasis of the analysis is placed on finding the relationships between current loop instability and converter operation conditions, so that the optimum design for the current feedback loop can be achieved. Other small-signal characteristics of these two controls will also be investigated and compared with those of PCM control in this study. It is also intended to study the issues related to the applications of ACM and charge controls to PFC circuit, such as the effect of the current loop instability on EMI

filter design, ways to avoid this instability, and the line current distortions introduced by different control schemes.

1.3 Outline of the Dissertation

The modeling and analysis of ACM control are discussed in Chapter II. The complete small-signal model of ACM control for all PWM dc-dc converters is derived. The relationship between current loop stability and converter operation conditions, as well as current loop compensation, is found for the first time. Based on the small-signal analysis, comprehensive design guidelines are provided. The model experimental verifications are also included in Chapter II

The modeling and analysis of PWM dc-dc converter employing charge control are covered in Chapter III. The derived model successfully predicts the current loop instability and its relationship to line voltage and load current of PWM converters. Based on small-signal analysis, the current loop design guidelines are obtained. The model is also verified by experiments.

The application of ACM and charge control in PFC circuits is studied in Chapter IV. Charge control has been applied to CCM flyback converter to obtain a single-stage PFC circuit. The merits and limitations of CCM flyback

PFC are discussed. The effect of the current loop instability on PFC system is studied, and the design procedures to eliminate subharmonic oscillation while still satisfying line current distortion requirement are also given in Chapter IV.

Chapter V summarizes the entire dissertation work.

2. MODELING AND ANALYSIS OF AVERAGE CURRENT-MODE CONTROL

2.1 Introduction

The main feature of ACM control is its ability to control the average value of the inductor current of a PWM converter. There are many applications in which the average inductor current of the converter needs to be controlled, such as boost PFC circuits, battery charger of a solar array power system, etc.. With PCM control, the peak inductor current of the converter is controlled. But for the same peak inductor current, the average inductor current is different if the

duty cycle is different, which means PCM control cannot accurately control average inductor current. ACM control possesses the main advantages of PCM control, such as short circuit protection and current sharing for parallel applications. It also overcomes some limitations of PCM control, such as switching noise problem and inability to optimize the current feedback loop.

The problems existing in PCM control and ways of overcoming them with ACM control are described in Section 2.2. The small-signal modeling process is presented in 2.3. The derived model is accurate up to half the switching frequency, which is necessary for the current loop design. In 2.4, the small-signal characteristics of ACM control are studied and compared with those of PCM control. The subharmonic oscillation phenomenon, which is common in all current-mode control, is also addressed. Based on the small-signal analysis performed in 2.4, comprehensive design guidelines for ACM control are established in 2.5. The small-signal model was verified by a testboard buck converter, and the experimental results are presented in 2.6.

2.2 Motivations

PCM control has been widely used for more than one decade. It has the following advantages: a) improved dynamic performance of the switching converter; b) inherent peak current limiting; c) current sharing for parallel applications. The circuit diagram of PCM control is shown in Fig. 2.1.

Several limitations exist in PCM control. PCM control cannot accurately control average inductor current because the current loop low-frequency gain is not high, as shown in Fig. 2.2. There is no integrator in the inductor current feedback loop; hence, dc error exists between the average inductor current and the control reference. The other limitation of PCM control is its poor noise immunity. For PCM control, the desired operation is as follows: the switch is turned on by the clock signal at the beginning of the cycle; the switch turns off when the peak inductor current reaches the control voltage. The switch turns on again when the next clock signal comes in. The sensed switch current usually contains switching noise. If the noise signal reaches control voltage before the peak inductor current, the switch is turned off prematurely.

To increase the low-frequency gain of the current loop gain, an integrator is needed in the current feedback loop. But simply adding an integrator greatly reduces the current loop crossover frequency, as shown in Fig. 2.2. Hence, a low frequency zero is needed to extend the current loop crossover. In certain

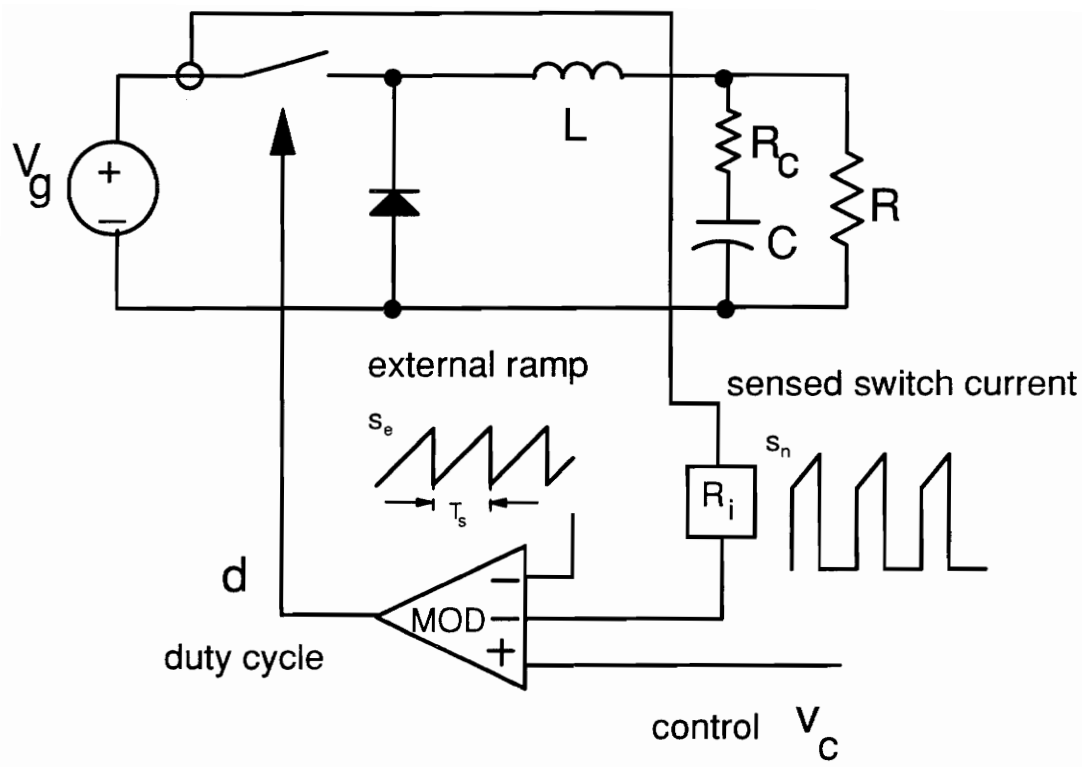

Figure 2.1. Peak current-mode control scheme: *In this control scheme, the peak inductor current is sensed by a current transformer. The switching noise picked by the current sensing network may turn off the switch before the peak inductor current reaches the control voltage, v_c.*

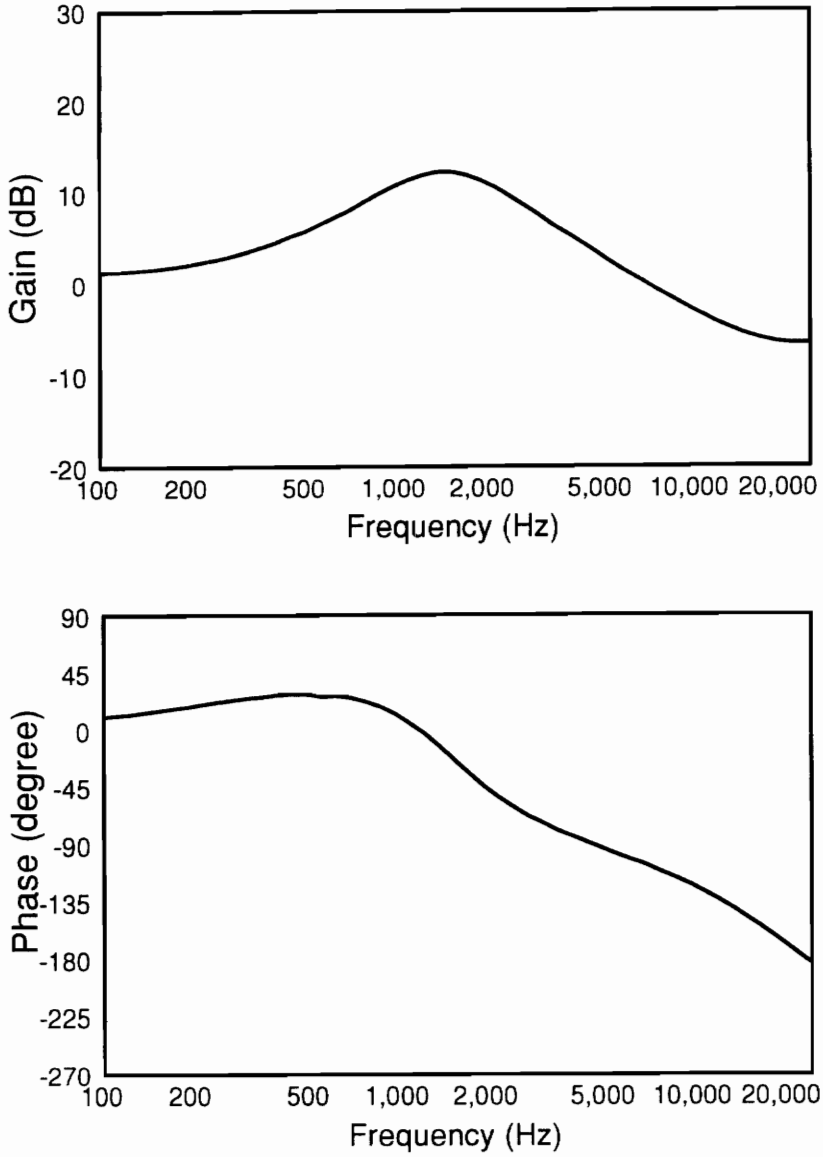

Figure 2.2. Current loop gain of PCM control: *Because there is only a dc gain in the current feedback loop, the low-frequency gain of the current loop is very low. It introduces dc error between the average inductor current and the control.*

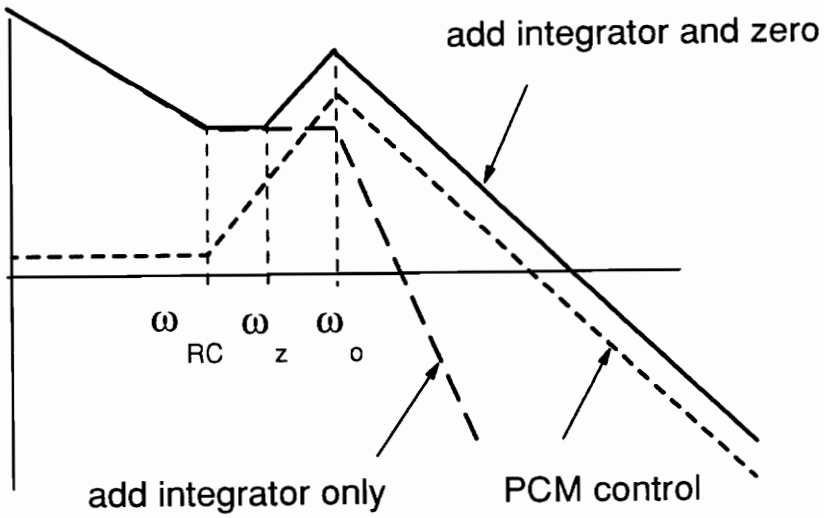

Figure 2.3. Ideal way to shape the current loop gain: *An integrator is added to boost the low-frequency gain. Adding only an integrator reduces the current loop crossover frequency; hence, a zero is needed to extend the current loop crossover frequency.*

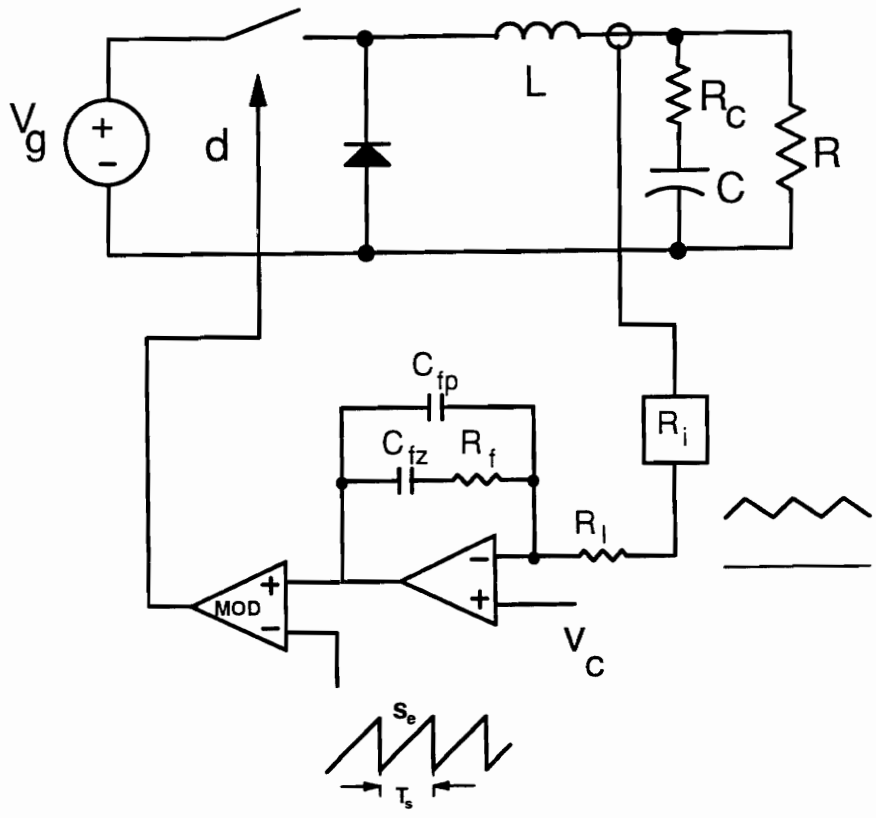

Figure 2.4. Average current-mode control scheme: *The inductor current is usually sensed by a resistor in series with the inductor. The sensed current goes to a compensation network before it is inputted to the modulator. The function of the ramp here is more like that of the sawtooth ramp in voltage-mode control.*

applications, a high frequency pole is added to filter the switching ripple of the sensed inductor current. By adding such a compensation network in the current loop, the ACM control scheme is formed. The circuit diagram of a buck converter with ACM control is shown in Fig. 2.4.

ACM control has been widely used because of the mentioned advantages, but due to the lack of an accurate small-signal model, its design is far from optimal. Usually, the average model of PCM control is directly applied to ACM control [8]. As will be seen later, the small-signal characteristics of the two controls are quite different. In the next section, a complete small-signal model is derived for ACM control, which gives accurate predictions up to half the switching frequency.

2.3 Small-Signal Modeling

2.3.1 Current Loop Modeling

In the early stage of current-mode control modeling, the sampled-and-hold effect in the current feedback loop is ignored. The current loop feedback is modeled only with a gain term, which is simply the current sensing gain of the circuit [13, 14]. The resulting low-frequency average models cannot correctly

predict the instability in the current loop because the current loop instability occurs at a much higher frequency.

Sample-data modeling technique [15, 16] has successfully provided a small-signal model for PCM control, which can accurately predict the instability in the current loop. One important small-signal property of PCM control predicted by sample-data modeling technique, is that its current loop gain always has -180 degrees phase lag at half the switching frequency. The current loop gain of PCM control derived in [16] contains infinite pairs of poles. It is of little use until the sampled-and-hold effect is approximated by a sampling gain, $H_e(s)$, which has the following simple form [18]:

$$H_e(s) \simeq 1 + \frac{s}{\omega_n Q_z} + \frac{s^2}{\omega_n^2}, \tag{2.1a}$$

$$Q_z = -\frac{2}{\pi}, \tag{2.1b}$$

$$\omega_n = \frac{\pi}{T_s}. \tag{2.1c}$$

The modeling approach for PCM control [18] is extended here to derive the small-signal model for ACM control. Differing from PCM control, the current feedback loop of ACM control contains a compensation network, $G_c(s)$:

$$G_c(s) = \frac{\omega_i(1 + \frac{s}{\omega_z})}{s(1 + \frac{s}{\omega_p})}, \tag{2.2a}$$

where

$$\omega_i = \frac{1}{R_i (C_{fp} + C_{fz})}, \tag{2.2b}$$

$$\omega_z = \frac{1}{R_f C_{fz}}, \tag{2.2c}$$

$$\omega_p = \frac{C_{fz} + C_{fp}}{R_f C_{fz} C_{fp}}. \tag{2.2d}$$

The first step for the current loop modeling is to modify the current loop model of PCM control. First, the current loop compensator block, $G_c(s)$, is added to the current loop. Secondly, the sampling gain, $H_e(s)$, in PCM control is replaced by the gain block, $H'_e(s)$, since the current compensator may affect this gain block. The modified current loop model is shown in Fig. 2.5, and all the blocks in Fig. 2.5 need to be determined.

The integrator-zero pair of $G_c(s)$ only affects the low-frequency characteristic of the current loop gain; it has no effect on the high-frequency characteristic of the feedback loop. To study the effect of the high-frequency pole, ω_p, on the current feedback loop, the following experiment is performed. ω_p, is added to

the current loop of the PCM control, and its position is changed from one tenth of the switching frequency (the switching frequency of the experiment converter is 45 kHz) to infinite. It is found though the experiment that the phase lag of the current loop gain always exhibits a 180^0 phase shift at half the switching frequency, no matter where ω_p is placed, as shown in Fig. 2.6, which is due to the sampled-and-hold nature of the current feedback loop. If ω_p is placed beyond half the switching frequency, it has no effect on the high-frequency gain and phase characteristics of the current loop gain. Since the purpose of the high-frequency pole is to eliminate high-frequency noise, it is usually placed around half the switching frequency. Then, ACM and PCM control have same high-frequency characteristics in the current loop. It means that the sampling gain, $H_e(s)$, used in PCM control, can be used to replace $H'_e(s)$ of ACM control by simply removing ω_p from the current loop. The low-frequency gain characteristics are also affected by ω_p, since the modulator gain is a function of ω_p. This effect will be included in the modulator gain.

If ω_p is placed before half the switching frequency, it cannot be removed from the current loop. Then the sampling gain of ACM control needs to be derived. The discrete sampling gain of PCM control is approximated by a continuous-time transfer function in [18]. For ACM control, to derive the discrete sampling gain and to approximate it are extremely difficult, and there may not exist a simple continuous-time transfer function for the sampling gain of ACM control.

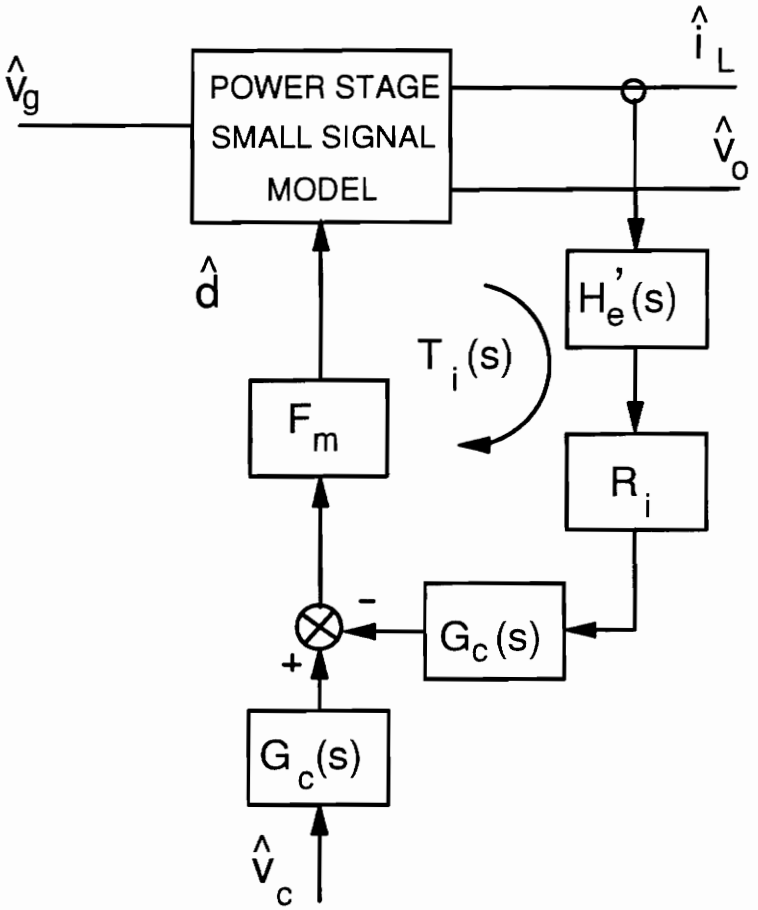

Figure 2.5. Assumed current loop model for ACM control: *F_m is the modulator gain, $H'_e(s)$ represents the sampled-and-hold effect in current loop, R_i is the current gain which transfers current into voltage, and $G_c(s)$ is the transfer function of the current compensator. Since v_c is also an input of the current compensator, $G_c(s)$ also exists in the voltage loop.*

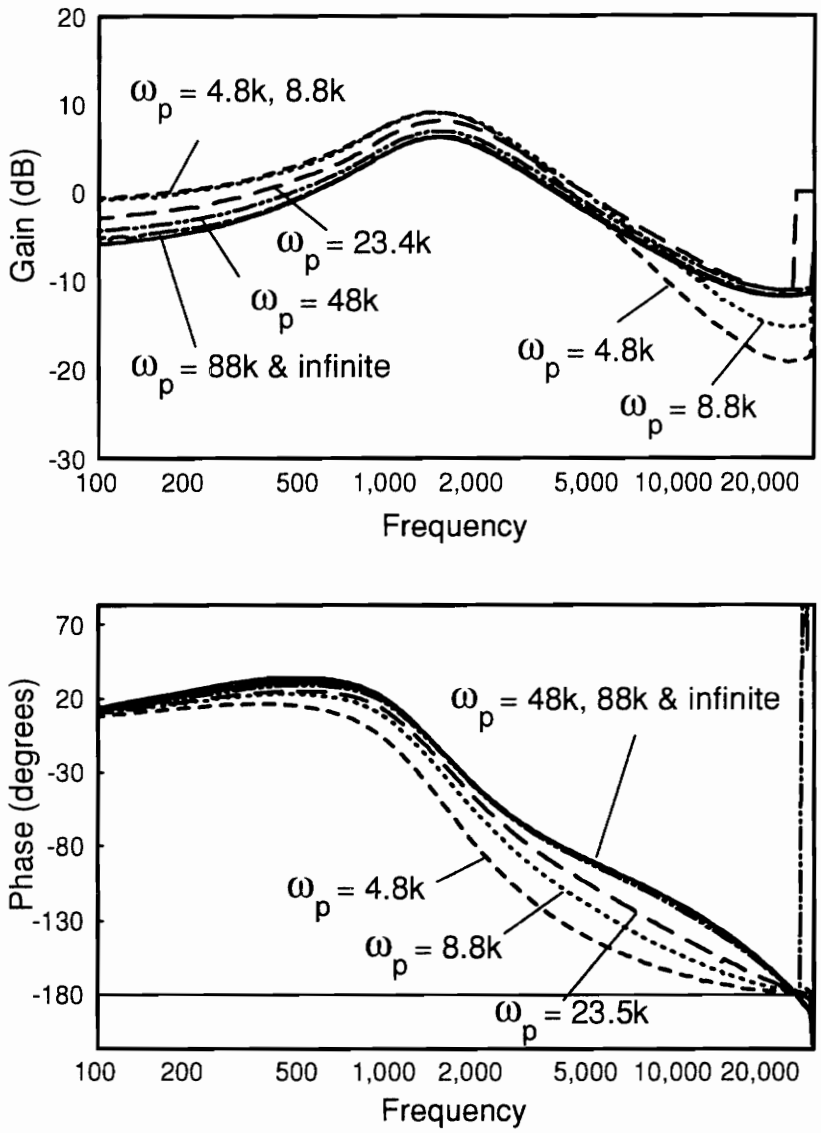

Figure 2.6. Measurement of the current loop gain with a high-frequency pole: *The switching frequency of the experiment converter is 45 kHz. The position of ω_p has no effect on the high-frequency characteristics of PCM control if it is placed after half the switching frequency. ω_p affects the low-frequency gain characteristics, since the modulator gain is a function of ω_p.*

2.3.2 Modulator Gain

In PCM control, both external ramp and sensed switch current are inputs of the modulator, as shown in Fig. 2.7(a), so the modulator gain is determined by the sum of the slopes of the two waveforms. The modulator gain of PCM control is [18]:

$$F_m = \frac{1}{(S_e + S_n)\, T_s}, \tag{2.3}$$

where S_e is the slope of the external ramp, S_n is the sensed inductor current on-time slope, and T_s is the switching period.

The modulator and its inputs of ACM control are shown in Fig. 2.7 (b). From Fig. 2.7 (b), it can be seen that the inductor current waveform of the PWM converter has been filtered by the compensator. The output of the current compensator, $\tilde{i}_L(t)$, is the input of the modulator. Hence, the modulator gain is determined by the sawtooth ramp slope, S_e, and the slope of $\tilde{i}_L(t)$, at turn-on time, S'_n:

$$F_m = \frac{1}{(S_e + S'_n)\, T_s}. \tag{2.4}$$

S'_n is derived in Appendix A, and it has a uniform expression for all PWM converters:

$$S'_n = S_n \xi, \tag{2.5a}$$

where

$$\xi = \omega_i DT_s + \omega_i \left(\frac{1}{\omega_z} - \frac{1}{\omega_p}\right)\left(1 - e^{-\omega_p DT_s}\right). \tag{2.5b}$$

Now the current loop model derivation is completed, and the model is shown in Fig. 2.8, where:

$$G_i(s) = \frac{\omega_i \left(1 + \frac{s}{\omega_z}\right)}{s}. \tag{2.6}$$

2.3.3 Feedback and Feedforward Gain

Although the current compensator is a low-pass network, the switching ripple at the output of the compensator is still comparable to the external ramp size, as shown in Fig. 2.9. Since the compensator output, $\tilde{i}_L$, is a function of the input and output voltages, the duty cycle is affected by the perturbations of the input and output voltages [18].

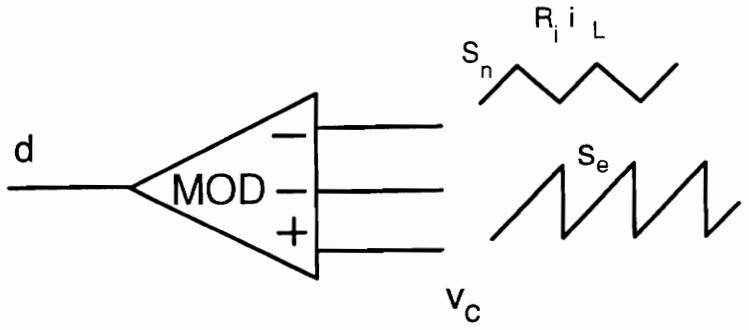

(a) modulator of PCM control

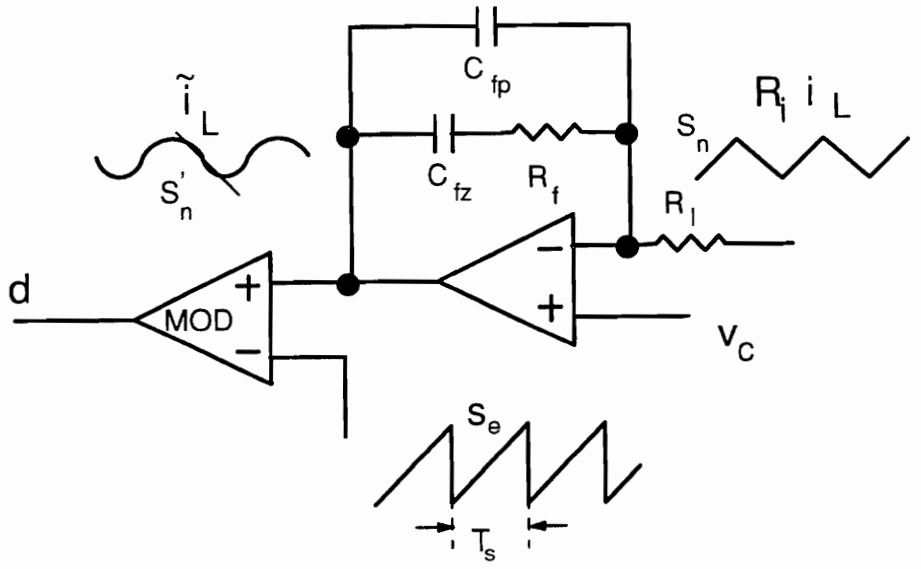

(b) modulator of ACM control

Figure 2.7. Modulator of PCM and ACM controls: *S_e is the slope of the external ramp in PCM control and the slope of sawtooth ramp in ACM control; S_n is the sensed inductor current on time slope; S'_n is the slope of $\tilde{i}_L$ at turn-on time.*

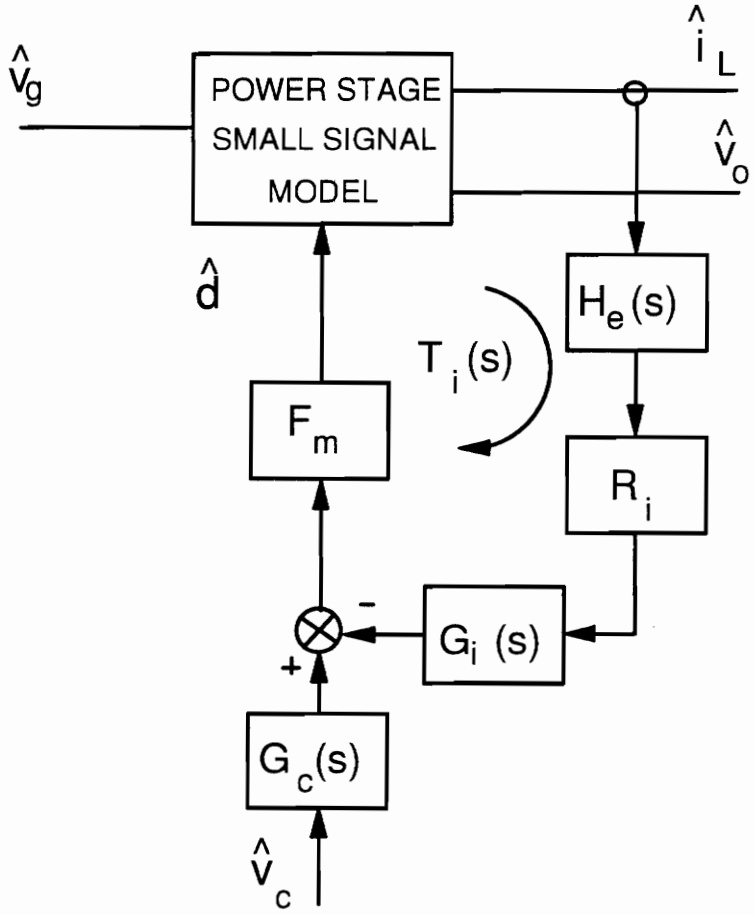

Figure 2.8. Derived current loop model: *The sampling gain, $H_e(s)$, used in PCM control is used here to represent the sampled-and-hold effect in the current loop. The high-frequency pole ω_p disappears from the current loop if it is placed beyond half the switching frequency. But it still exists in the voltage loop. The modulator gain, F_m, is also a function of the current compensator parameters.*

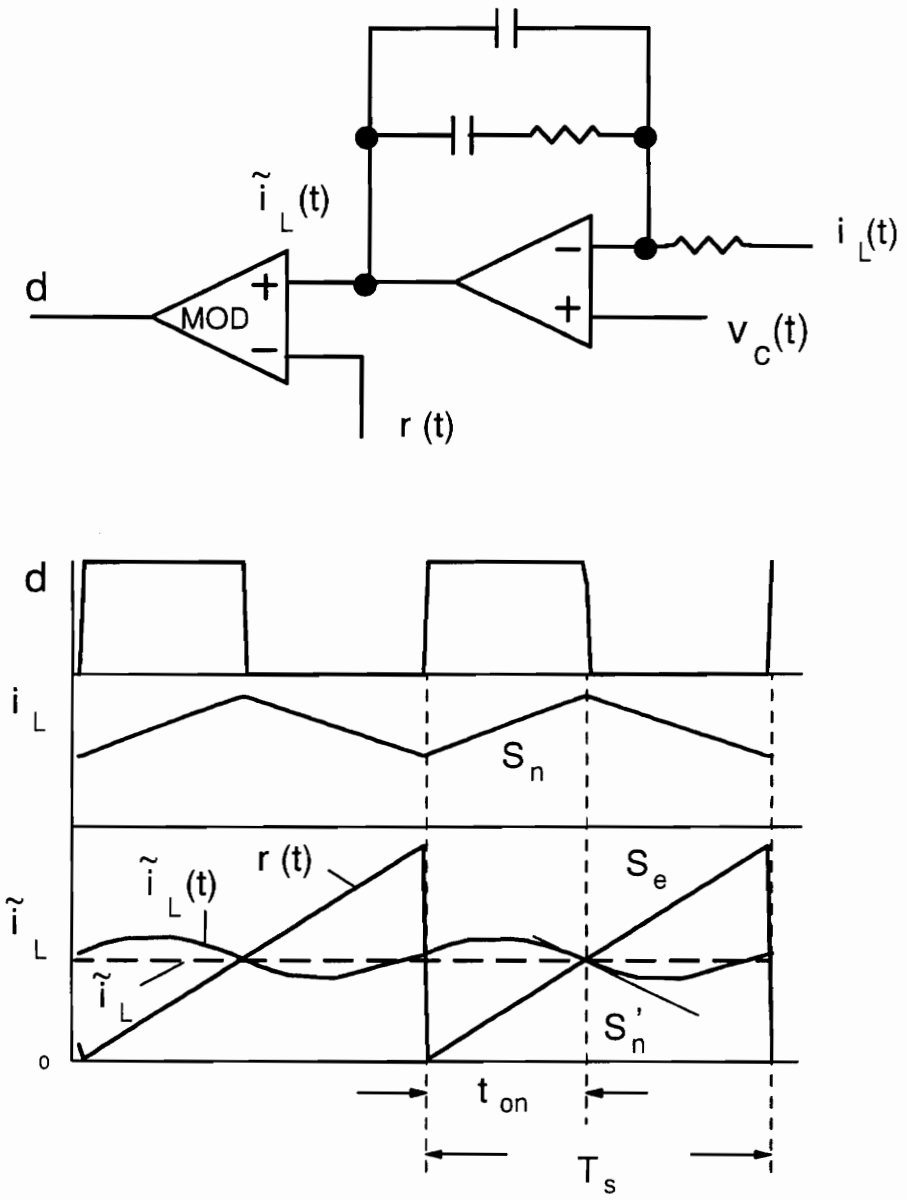

Figure 2.9. The input waveforms of the modulator: *Although a current compensator exists in the current loop, the ripple of the current compensator output, which is a function of the input and output voltages, is still comparable to the sawtooth ramp.*

Since the feedforward and feedback gain are merely constant gain, for simplicity one can assume that the compensator is replaced by a constant gain K. From Fig. 2.9 the following relation is obtained:

$$\tilde{i}_L = -K(R_i i_L - v_c), \tag{2.7}$$

where $\tilde{i}_L$, i_L, and v_c denote the average value of the exact time waveform $\tilde{i}_L(t)$, $i_L(t)$, and $v_c(t)$, respectively.

From the steady-state waveforms of ACM control, shown in Fig. 2.9, the following relationship can be obtained:

$$\tilde{i}_L = S_e\, dT_s. \tag{2.8}$$

Substituting Eq. (2.8) to Eq. (2.7):

$$K(R_i i_L - v_c) = -S_e dT_s. \tag{2.9}$$

Equation (2.9) gives the relation between the average inductor current and input and output voltages. By perturbing Eq. (2.9) with respect to input and output voltages, the input voltage and output voltage to inductor current transfer functions can be obtained.

The effect of the input and output voltage perturbations on the duty cycle can be modeled by the feedback and feedforward gain terms, k_r and k_f, from the input and output voltages [14, 18], as shown in Fig. 2.10, where at low

frequency the $G_i(s)$ and $G_c(s)$ are replaced by the high dc gain, K, and $H_e(s)$ equals one. The same transfer functions can also be obtained from the model shown in Fig. 2.10, with k_r and k_f as the unknowns. By comparing these transfer functions, k_r and k_f are obtained.

The detailed derivations for k_f, k_r, can be found in Appendix A. The feedback and feedforward gains for three basic PWM converters are listed in Table 2.1.

Table 1. Feedforward and Feedback Gains for Average Current-Mode Control

	BUCK	BOOST	BUCK/BOOST
k_f	$-\frac{R_i D D' T_s}{L}\xi$	$-\frac{R_i D' T_s}{L}\xi$	$-\frac{R_i D D' T_s}{L}\xi$
k_r	$\frac{R_i D' T_s}{L}\xi$	$\frac{R_i D'^2 T_s}{L}\xi$	$\frac{R_i D'^2 T_s}{L}\xi$

2.3.4 Complete Small-Signal Model

Since the error voltage from the voltage loop is also inputted to the current compensator, the current loop compensator $G_c(s)$ also exists in the voltage feedback loop. And due to the existence of the low pass filter in the converter power stage, the voltage loop does not behave as a sampling system; hence the compensator high-frequency pole, ω_p, does exist in the voltage loop. The

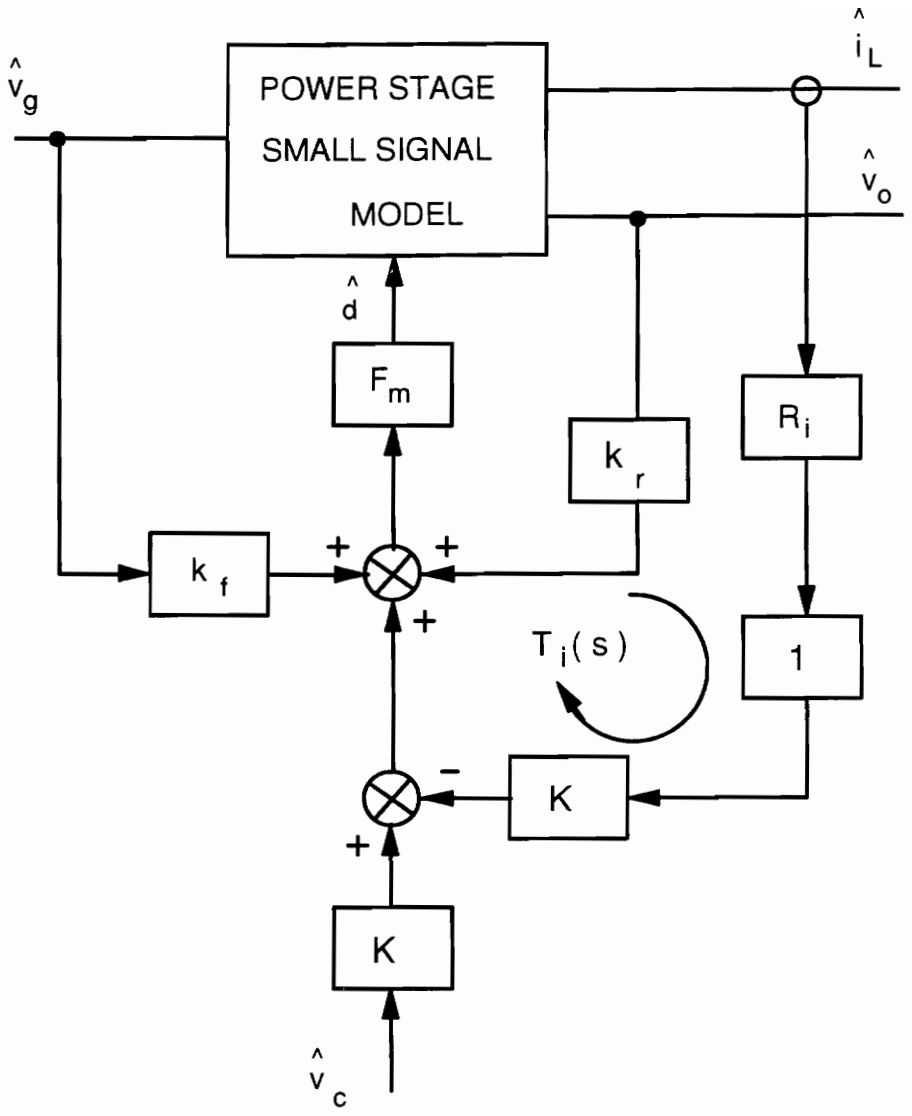

Figure 2.10. Modeling the effect of the input and output voltage perturbations: *At very low frequency, the sampling gain, $H_e(s)$, is replaced by one, and both $G_i(s)$ and $Gc(s)$ are replaced by a high dc gain K. The input and output voltages to inductor current gains can be obtained from the model, with k_f and k_r as the unknowns.*

complete small-signal model of PWM converter with ACM control is shown in Fig. 2.11.

2.4 Small-Signal Characteristics

The derived small-signal model can be used to generate the small-signal characteristics for all PWM converters with ACM control. The approximate expressions for these characteristics can also be derived from the model. These analytical expressions are very helpful in gaining physical insight and facilitate the design.

In this section, the small-signal characteristics of PWM converter with ACM control are studied. The current loop stability and its relation to converter operation conditions are investigated. The small-signal characteristics are generated with buck converter as the power stage. The corresponding analytical expressions of these characteristics are also derived. The characteristics are compared with those of PCM control.

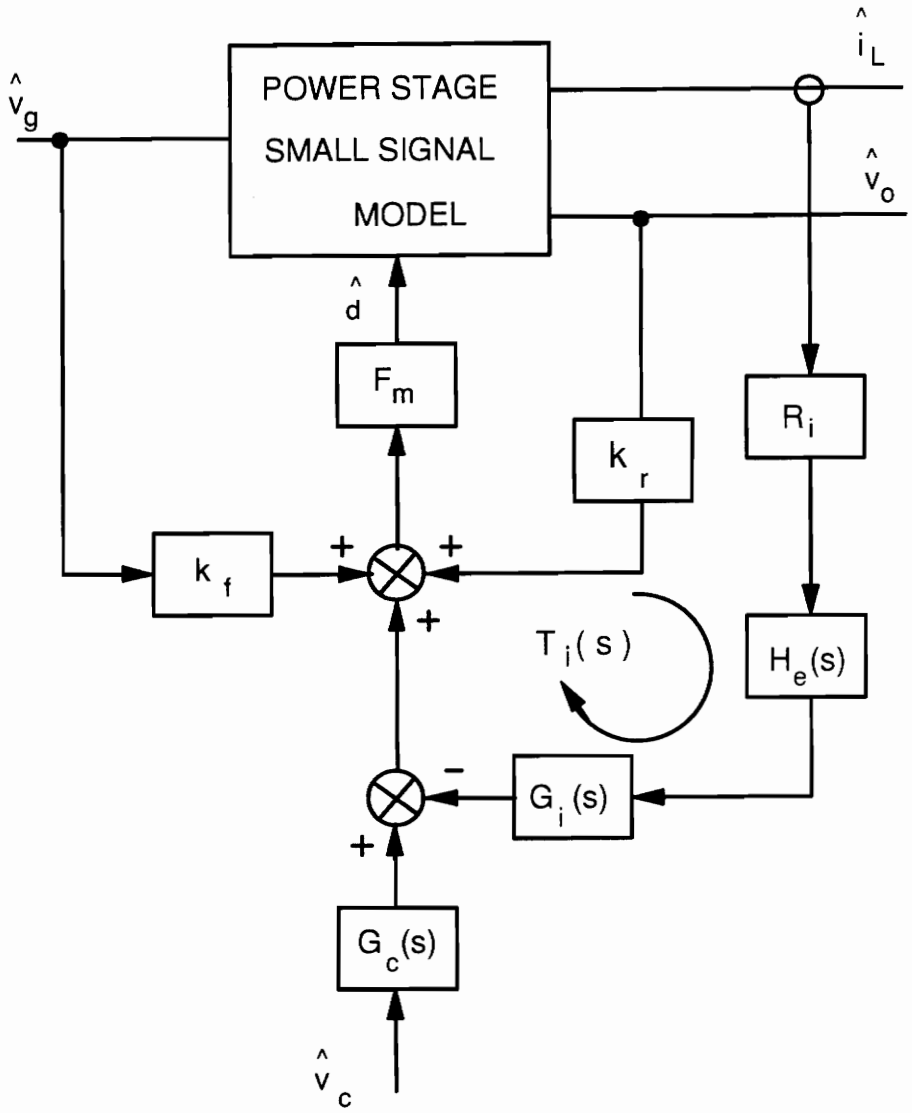

Figure 2.11. Complete small-signal model for ACM control: *F_m is the modulator gain, $H_e(s)$ represents the sampled-and-hold effect in current loop, R_i is the current gain which transfers current signal into voltage signal, while k_r and k_f represent the feedback and feedforward functions due to the current feedback.*

2.4.1 Current Loop Gain

Current loop gain is defined as the loop gain measured at the output of the duty cycle modulator with the current loop closed. It determines the stability of the current loop and the characteristics of the subsystem after current loop is closed. Ignoring the gain term k_r, the approximate expression for the current loop gain, $T_i(s)$, is given in by:

$$T_i(s) \simeq F_m R_i G_i(s) G_{id}(s) H_e(s). \tag{2.10}$$

$H_e(s)$, F_m, and $G_i(s)$ are given by Eqs. (2.1), (2.4), and (2.6), respectively. $G_{id}(s)$ is the power stage duty cycle-to-inductor current transfer function.

Since only high-frequency characteristic determines the current loop stability, the high-frequency expression of Eq. (2.10) is derived. When the perturbation frequency is larger than the filter resonant frequency and smaller than half the switching frequency, we have:

$$G_{id}(s) \simeq \frac{V_{ap}}{s L}, \tag{2.11}$$

and

$$G_i(s) \simeq \frac{\omega_i}{\omega_z}. \tag{2.12}$$

Substituting Eqs. (2.4), (2.11), and (2.12) into Eq. (2.10), the high-frequency approximation of $T_i(s)$ is obtained:

$$T_i^h(s) \simeq \frac{F_s}{D'\xi + \frac{S_e L}{R_i V_{ap}}} \frac{\omega_i}{\omega_z} \frac{H_e(s)}{s} = \frac{K_I}{s} H_e(s) \tag{2.13}$$

When K_I is smaller than half the switching frequency, the current loop crossover frequency equals K_I. If K_I is sufficiently smaller than half the switching frequency, the current loop has 90 degrees phase margin, since $H_e(s)$ contributes little phase lag at the frequencies which are much lower than half the switching frequency. If K_I is larger than half the switching frequency, the gain characteristic of the current loop is larger than one at half the switching frequency and the phase lag equals -180 degrees. Hence, the current loop is unstable when K_I is larger than half the switching frequency.

K_I is a function of the duty cycle, the external ramp slope, and the current compensator parameters:

$$K_I = \frac{F_s}{D'\xi + \frac{S_e L}{R_i V_{ap}}} \frac{\omega_i}{\omega_z} \tag{2.14}$$

where

$$\xi = \omega_i D T_s + \omega_i \left(\frac{1}{\omega_z} - \frac{1}{\omega_p} \right) \left(1 - e^{-\omega_p D T_s}\right). \tag{2.15}$$

For a buck converter, when the duty cycle, D, approaches zero, V_{ap} approaches infinite, and ξ approaches zero, hence, K_I approaches infinite. It indicates that the current loop tends to be unstable for small duty cycle.

When the duty cycle, D, approaches one, the K_I of a buck converter becomes:

$$K_I = \frac{F_s R_i V_o}{S_e L} \cdot \frac{\omega_i}{\omega_z} \tag{2.16}$$

By properly selecting the current loop compensator parameters or the external ramp slope, the K_I given in Eq. 2.16 can be smaller than half the switching frequency.

The current loop gains of the ACM-controlled buck converter, with different duty cycles, are shown in Fig. 2.12. It can be seen that when the duty cycle is small (D=0.2), the gain characteristic does not intersect the zero dB line; hence, the current loop is unstable. when the duty cycle, D, increases, the gain characteristic intersects the zero dB line and the current loop has more than 30 degrees phase margin. For the purpose of the comparison, the current loop gains of PCM control, with D as the running parameters, are generated and shown in Fig. 2.13, For PCM control, the current loop phase margin reduces as the duty cycle increases.

The relationship between the duty cycle and the current loop stability of ACM control is found for the first time through the small-signal analysis. According

to the current loop gain shown in Fig. 2.12, for the specific design, the current loop is stable at $D = 0.42$ and $D = 0.71$; it is unstable at $D = 0.2$. This result is quite different from PCM control. To verify the small-signal predictions, the time-domain simulation is performed. The simulation results are shown in Fig. 2.14. The simulation results confirm the small-signal predictions.

Since the gain of the current loop gain at high-frequency is also a function of both current compensator parameters and the sawtooth ramp slope, all of them affect the current loop stability margin. It gives a lot of options for the current feedback loop optimum design.

2.4.2 Control-to-Output Voltage Gain

The control-to-output gain is defined as the control voltage to output voltage transfer function with the current loop closed. Together with voltage loop compensator, it forms the outer loop gain of the system. Hence, the control-to-output gain directly affects the overall system stability and closed loop dynamic performance. Figure 2.15 shows the transfer function with different line and load conditions. For the purpose of comparison, the same transfer function for PCM control is also plotted and shown in Fig. 2.16. In both cases, the buck converter is used as the power stage. It can be seen from Figs. 2.15 and 2.16 that the low-frequency characteristics of both controls are

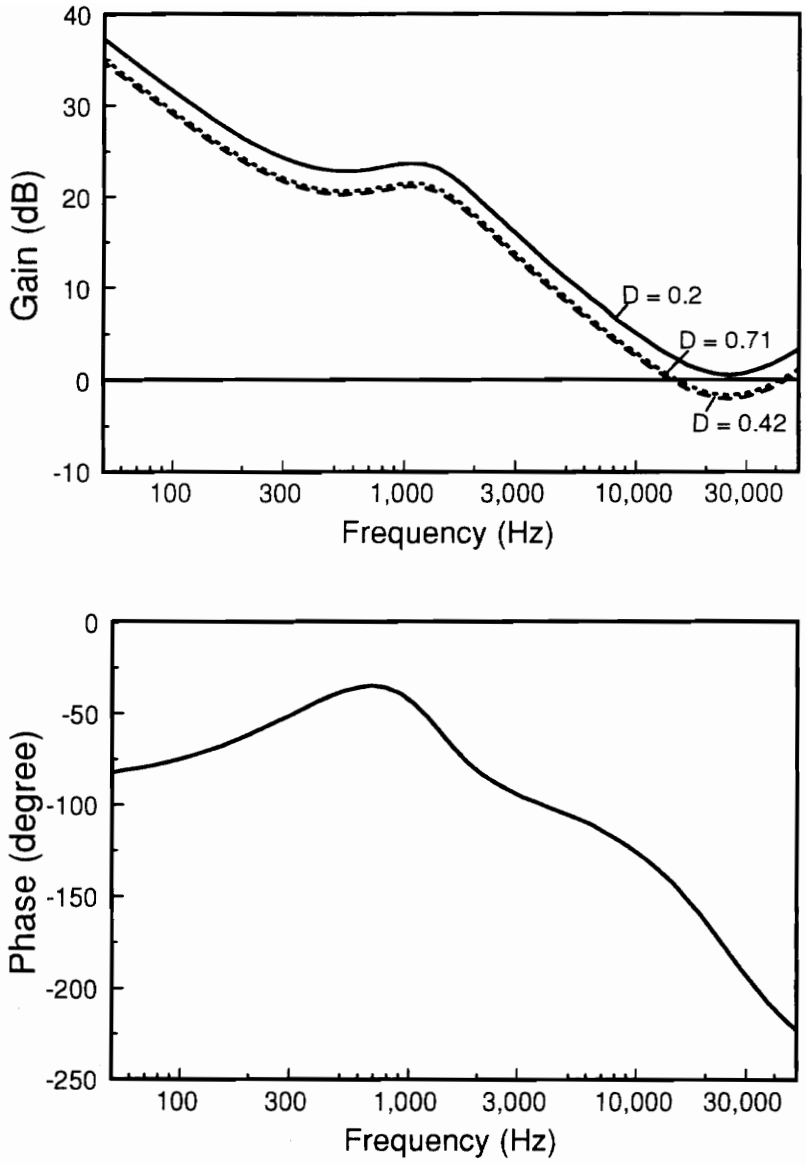

Figure 2.12. Current loop gain of ACM control with duty cycle as the running parameter: *As the duty cycle increases, the gain characteristic is first shifted up, and then shifted down. This is due to the nonlinear relation between F_m and the duty cycle. When $D = 0.2$, the gain characteristic does not intersect the zero dB line, which means that the current loop does not have any phase and gain margins.*

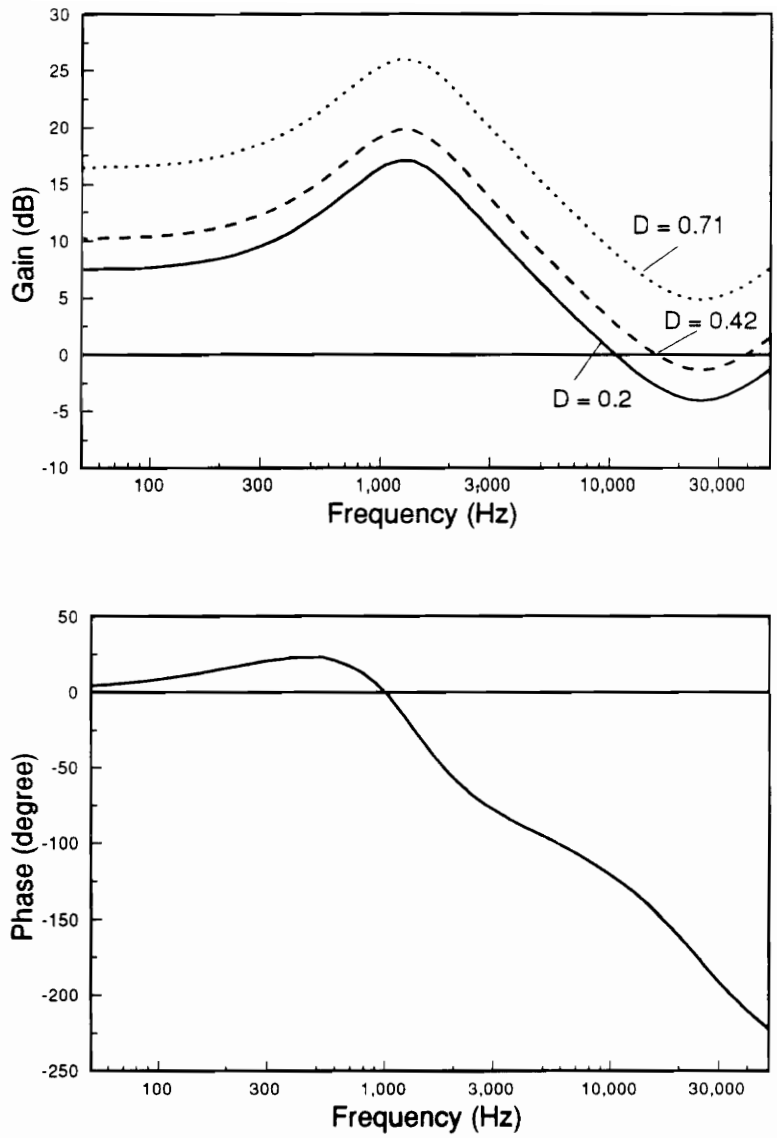

Figure 2.13. Current loop gain of PCM control with duty cycle as the running parameter: *As the duty cycle increases, the gain characteristic is shifted up monotonously, which results in a decrease in current loop stability margin.*

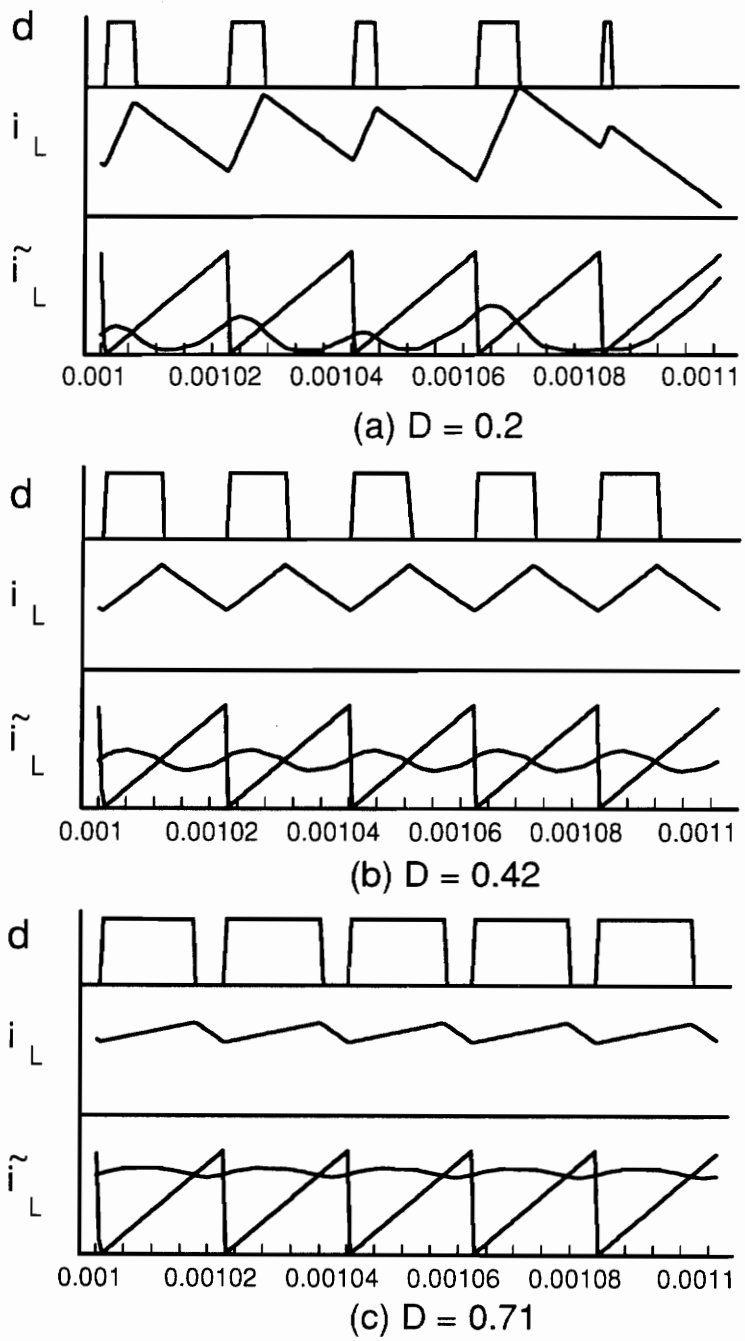

Figure 2.14. Open loop time domain simulation results of ACM control: *When $D = 0.2$, the open loop system is unstable. The subharmonic oscillation has no fixed pattern because the current loop gain is a nonlinear function of the duty cycle. The current loop is stable for a larger duty cycle.*

almost same. Both controls have a pair of double poles at half the switching frequency. However, the effects of the duty cycle on the damping of the double pole are different, which means that the current loop stability margin and its relation with duty cycle are different for these two controls. For ACM control, the current compensator pole, ω_p, also exists in control-to-output gain. When buck converter is the power stage, the approximate expression of control-to-output gain of ACM control is given as follows:

$$\frac{\hat{v}_o}{\hat{v}_c} \simeq \frac{R}{R_i} \frac{(1 + s R_c C)}{[1 + s R (C + C_x)] (1 + \frac{s}{\omega_p})} F_h(s), \tag{2.17}$$

where

$$C_x = \frac{1}{F_m V_g \omega_i R_i}, \tag{2.18}$$

and

$$F_h(s) = \frac{1}{1 + \frac{s}{\omega_n Q_p} + \frac{s^2}{\omega_n^2}}, \tag{2.19a}$$

where

$$\omega_n = \frac{\pi}{T_s} = \frac{\omega_s}{2}, \tag{2.19b}$$

$$Q_p = \frac{1}{\pi(m'_c D' \frac{\omega_z}{\omega_i} - \frac{1}{2})}, \tag{2.19c}$$

and

$$m'_c = \xi + \frac{S_e}{S_n}. \tag{2.19d}$$

Q_p is the damping factor of the double pole, $F_h(s)$, centered at half the switching frequency. Q_p can be used to predict the current loop instability. When Q_p is large, the peaking of $F_h(s)$ is large; the current loop has less phase margin [18].

The derivation of Q_p for all PWM converters can be found in Appendix A. The Q_p given in Eq. (2.19c,d) is general for all PWM converters. It can be seen that Q_p is a function of line voltage, the sawtooth ramp slope, and the current compensator parameters. If the current compensator is removed from current loop, the damping factor of ACM control is converged to the damping factor of PCM control [18]:

$$Q_p^{PCM} = \frac{1}{\pi(m_c D' - \frac{1}{2})}, \tag{2.20a}$$

where

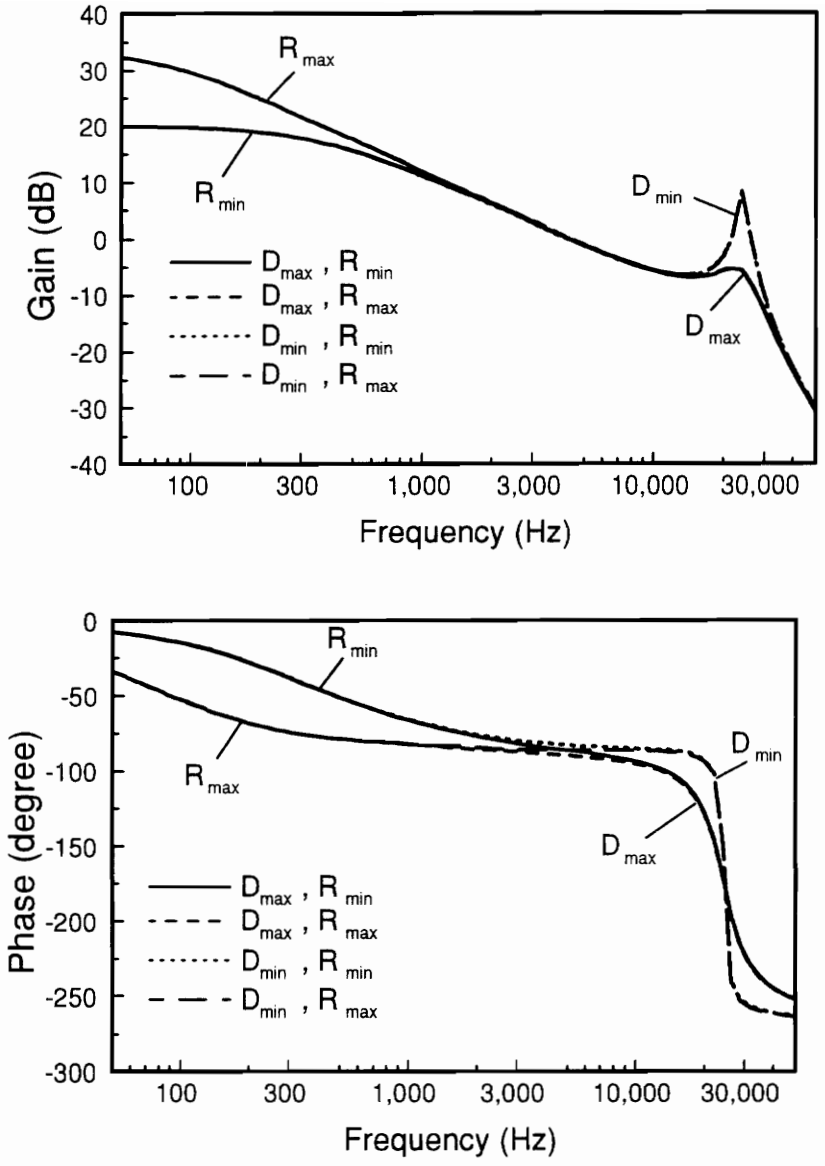

Figure 2.15. Control-to-output voltage gain with different operation conditions: *There is only a single pole in the low frequency characteristic. The damping of the double pole at half the switching frequency is affected by the line voltage, and high line is corresponding to light damping.*

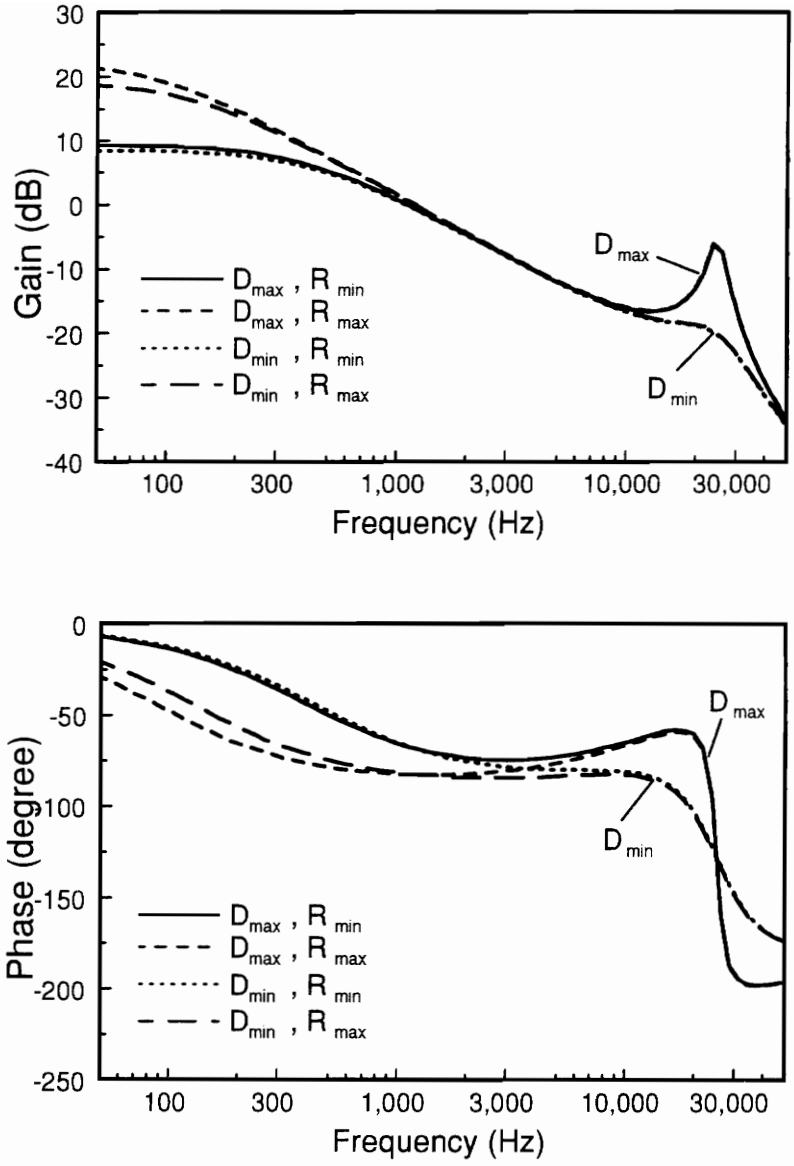

Figure 2.16. Control-to-output voltage transfer function of PCM control: *The high-frequency characteristic is affected by the line voltage, but the trend is opposed to ACM control. Here, large duty cycle corresponds to large peaking. The line voltage also slightly affects the low-frequency characteristics.*

$$m_c = 1 + \frac{S_e}{S_n}. \qquad (2.20b)$$

It can be seen from Eq. (2.20) that for PCM control only the external ramp slope affects Q_p^{PCM}. While in ACM control, Q_p is affected by the ramp slope, S_e, as well as the current compensator parameters. It means that in ACM control not only the ramp slope but also the current compensator can be used to compensate the current loop instability. Compared to PCM control, the current loop design of ACM control is more complicated. A comprehensive current loop design procedure for ACM control is given in Section 2.5.

2.4.3 Control-to-Inductor Current Gain

The control-to-inductor current gain is defined as the control voltage to average inductor current transfer function with current loop closed. This gain shows the ability of the system to control the average inductor current. The control-to-inductor current gains of both ACM and PCM controls are shown in Fig. 2.17, with buck converter as the power stage. The gain characteristic of ACM control, shown in Fig. 2.17 (a), is flat almost up to half the switching frequency, and is only determined by the current sensing gain, R_i, which does not change with line and load conditions. The gain characteristic of PCM

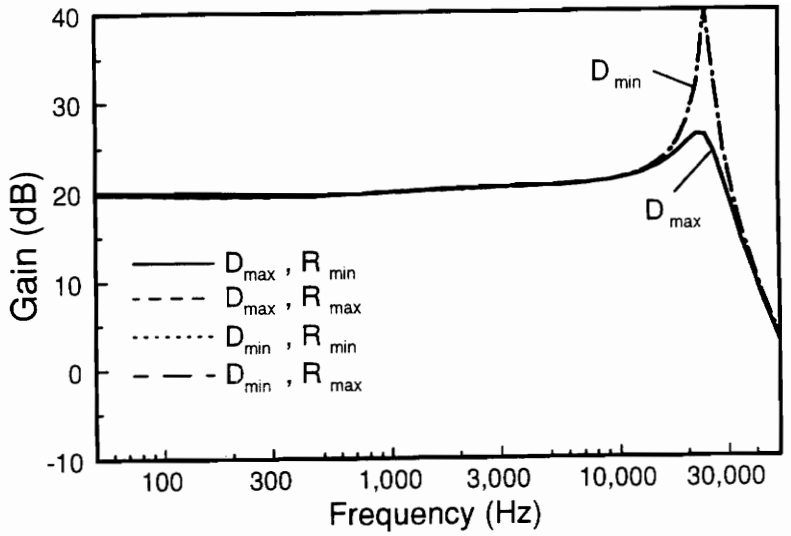

(a) ACM control

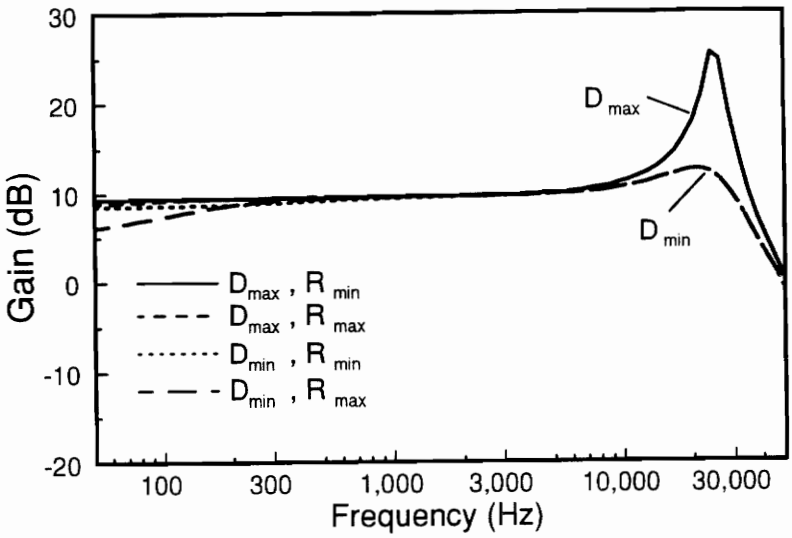

(b) PCM control

Figure 2.17. The control-to-inductor current gain of PCM and ACM control: *The gain characteristics of PCM control vary with the operation conditions. The gain characteristic of ACM control does not vary with the operation conditions; it is flat up to half the switching frequency.*

control, on the other hand, is not flat, and it varies with the line voltage and the load resistance, as shown in Fig. 2.17 (b). When the gain characteristic is uneven, the control variable will be distorted from a varying control reference.

2.4.4 Audiosusceptibility

The audiosusceptibility of a current-mode controlled converter is the input voltage to output voltage transfer function with the current loop closed. The audiosusceptibility of a PWM converter is reduced by current feedback loop. The higher the current loop gain, the lower the audiosusceptibility of a current-mode controlled converter. Since the low-frequency current loop gain of ACM control is much higher than that of PCM control, the low-frequency audiosusceptibility of ACM control is much lower than that of PCM control.

For a buck converter, the inductor current feedback also brings negative feedforward from input voltage, which further reduces its audiosusceptibility [18]. In PCM control case, the audiosusceptibility of a buck converter can be totally cancelled if the external ramp is selected equal to half of the inductor current off-time slope [18]. The expression of the audiosusceptibility of a buck converter with ACM control is derived from the small-signal model shown in Fig. 2.11:

$$\frac{\hat{v}_o}{\hat{v}_g} = \frac{R(k_f + \frac{D}{F_m V_g})}{R_i} \quad \frac{1}{G_i(s)} \quad \frac{(1 + sR_cC)}{[1 + sR(C + C_x)]} \quad F_h(s). \tag{2.21}$$

$G_i(s)$ and $F_h(s)$ are given by Eqs. (2.6) and (2.19). It can be seen from Eq. (2.21) that the dc gain cancellation also exists, since k_f is negative for a buck converter. Substituting the expressions of k_f and F_m into Eq. (2.21), it becomes as follows:

$$\frac{\hat{v}_o}{\hat{v}_g} = \frac{RD^2T_sS_e}{R_iV_o} \quad \frac{1}{G_i(s)} \quad \frac{(1 + sR_cC)}{[1 + sR(C + C_x)]} \quad F_h(s). \tag{2.22}$$

It can be seen from Eq. (2.22) that the audiosusceptibility of a buck converter cannot be totally cancelled since S_e cannot be chosen as zero in ACM control. The audiosusceptibility is affected by S_e, and S_e should be as small as possible from the audiosusceptibility point of view. The audiosusceptibilities of a buck converter with ACM and PCM controls are shown in Fig. 2.18 (a) and (b), respectively.

2.4.5 Output Impedance

The output impedance of a current-mode controlled converter is the output current to output voltage transfer function with current loop closed. The output

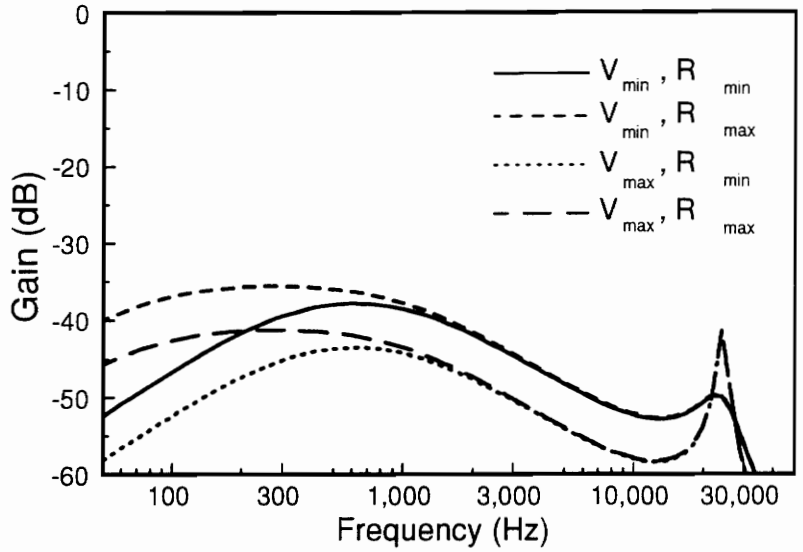

(a) ACM control

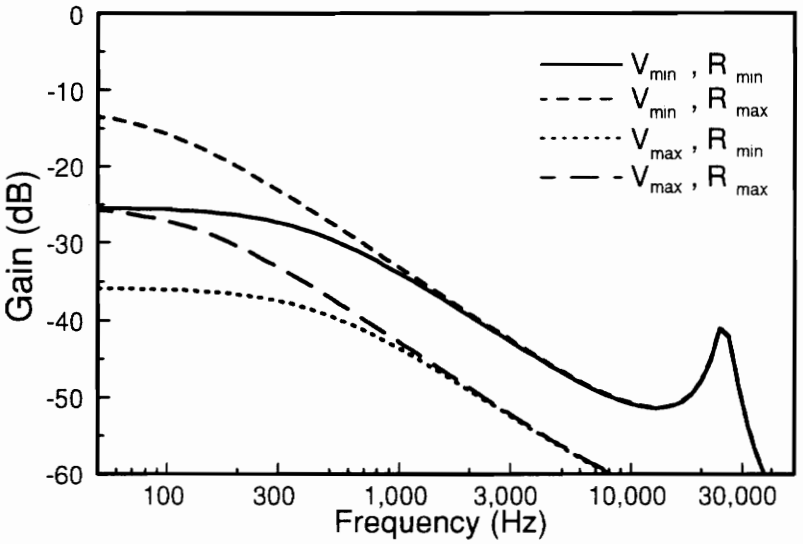

(b) PCM control

Figure 2.18. Audiosusceptibilities of ACM and PCM controls: *The inherent input voltage feedforward reduces the audio of a buck converter with ACM or PCM control. Due to the higher low-frequency gain in the current loop, the low-frequency audio of the buck converter with ACM control is further reduced.*

impedances of a buck converter with ACM and PCM controls are shown in Fig. 2.19 (a) and (b), respectively. Closing the current feedback loop has a strong effect on the output impedance of the converter. For voltage-mode control, the output impedance is very small at low-frequency, so the system behaves like a voltage source. For PCM and ACM control, the low-frequency output impedances are mainly determined by converter load resistance. The high low-frequency output impedance is a potential drawback of current-mode controls. The natural voltage-source characteristics of voltage-mode control, where the output voltage is relatively insensitive to load current, are not retained. Feedback of the inductor current creates a soft current source and a corresponding increase in impedance. Fortunately, a high outer loop gain can usually be used to attenuate the closed loop output impedance to a very low value.

2.5 *Experimental Verifications*

A buck converter was built to verify the accuracy of the derived small-signal model. The predictions are generated by PSPICE simulation. To measure the current loop gain, a digital modulator [24] was used to ensure that the correct sampled-data loop gain was obtained. All other measurements were performed with conventional analog measurement schemes.

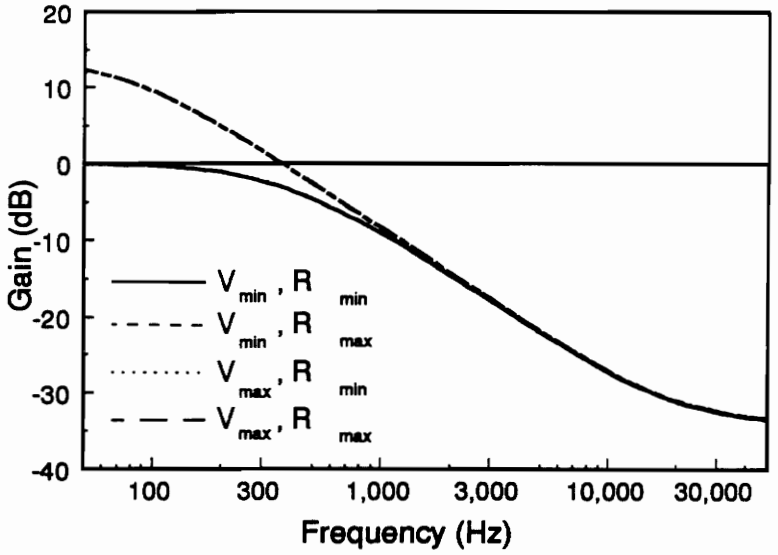

(a) ACM control

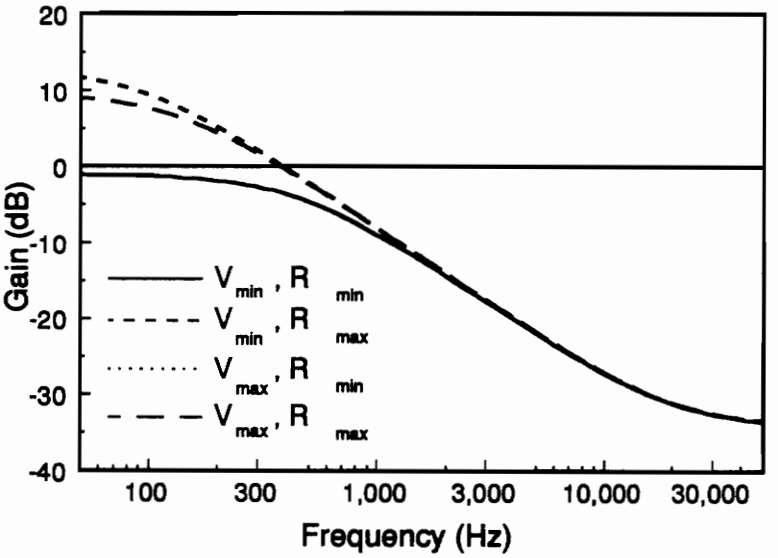

(b) PCM control

Figure 2.19. Output impedances of ACM and PCM controls: *The output impedances of ACM and PCM controls are almost same to each other. The low-frequency output impedances are determined by the load resistance, which are much higher than that for voltage-mode control.*

The measured and predicted current loop gains are shown in Fig. 2.20. Both the gain and phase measurements agree very well with predictions up to half of the switching frequency. The control-to-output voltage and control-to-inductor current gains, measured with the current loop closed, are shown in Fig. 2.21 and Fig. 2.22, respectively. The measurements again show a very good correlation with the theoretical results. The peak of the gains at half the switching frequency clearly shows the existence of two complex poles. The measured and predicted results of the audio susceptibility of the buck converter with current loop closed are shown in Fig. 2.23. Again, the measurement and prediction agree very well.

2.6 Design Guidelines

The current loop design of ACM control involves selecting the sawtooth ramp slope, S_e, and designing the current compensator, $G_c(s)$.

The function of the sawtooth ramp is similar to that of the ramp used in voltage-mode control. Here, the error between the control voltage and the average inductor current is compared with the sawtooth ramp to determine the turn-off time of the switch. Unlike voltage-mode control, the magnitude of the

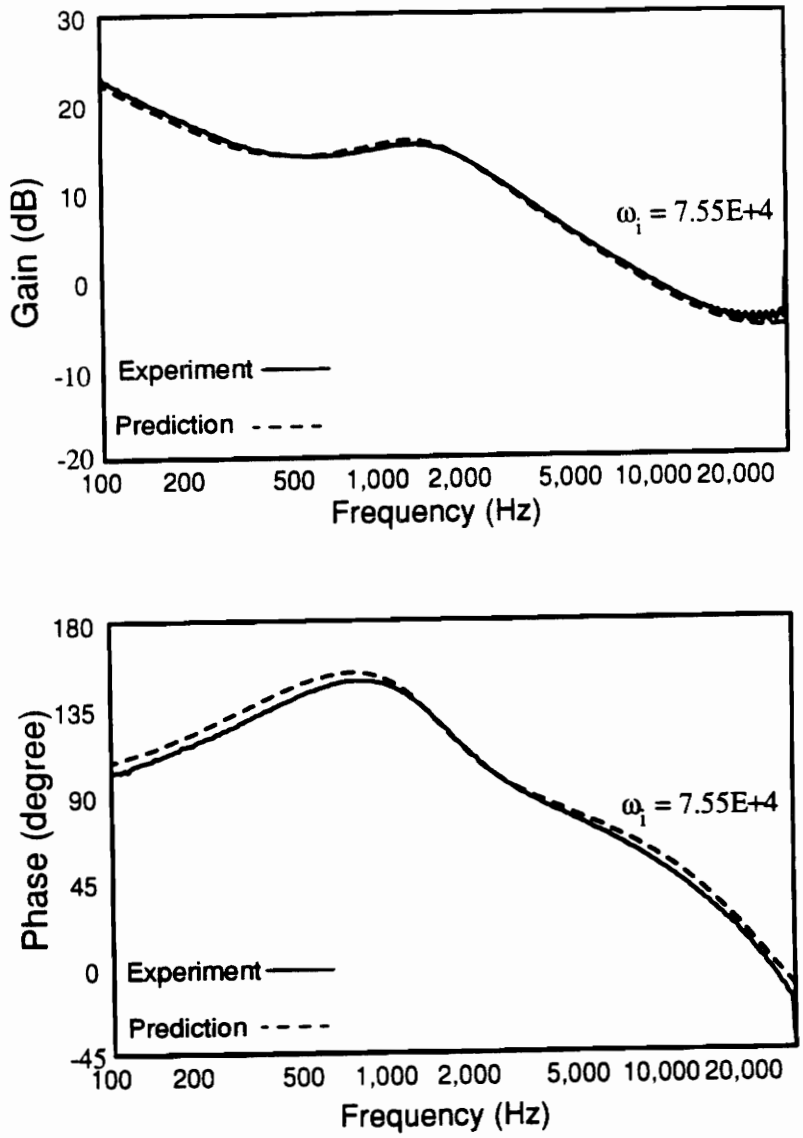

Figure 2.20. Measurement and prediction of the current loop gain for buck converter: *The solid line represents measurement, and the dashed line represents prediction. The switching frequency of the converter is 45 kHz.*

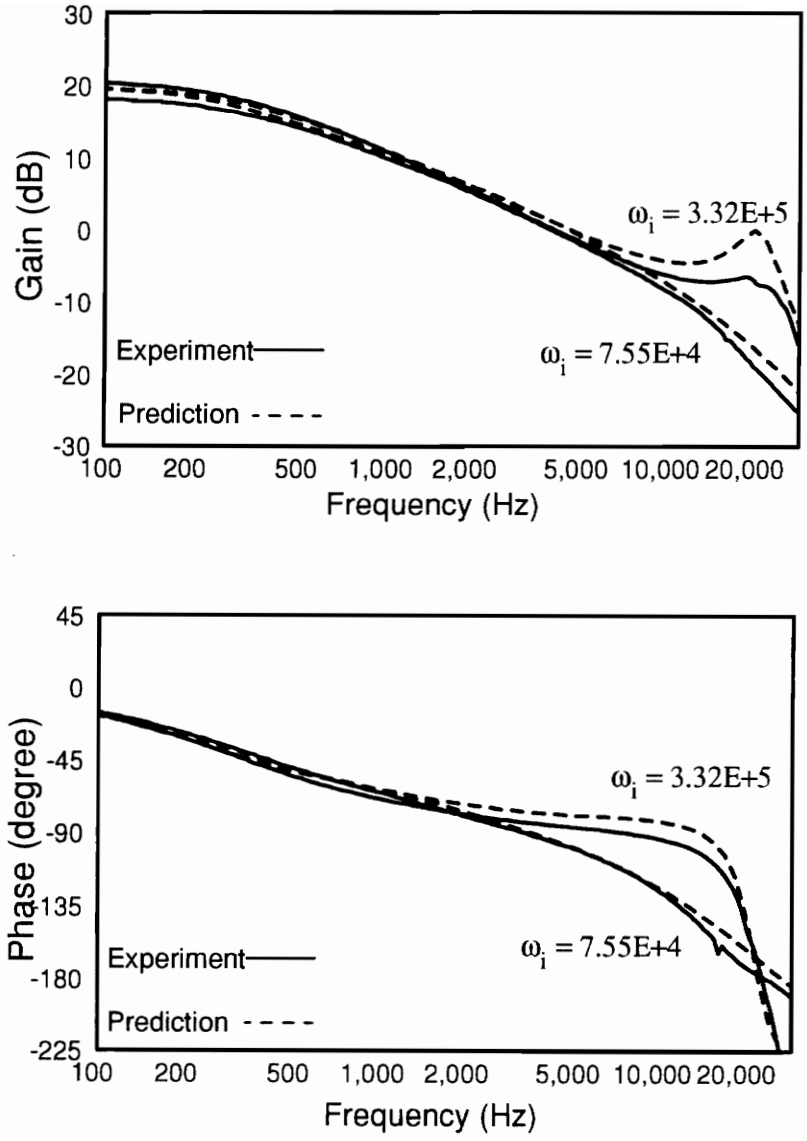

Figure 2.21. Measurement and prediction of control-to-output gain for buck converter: *The solid line represents measurement, and the dashed line represents prediction. The switching frequency of the converter is 45 kHz.*

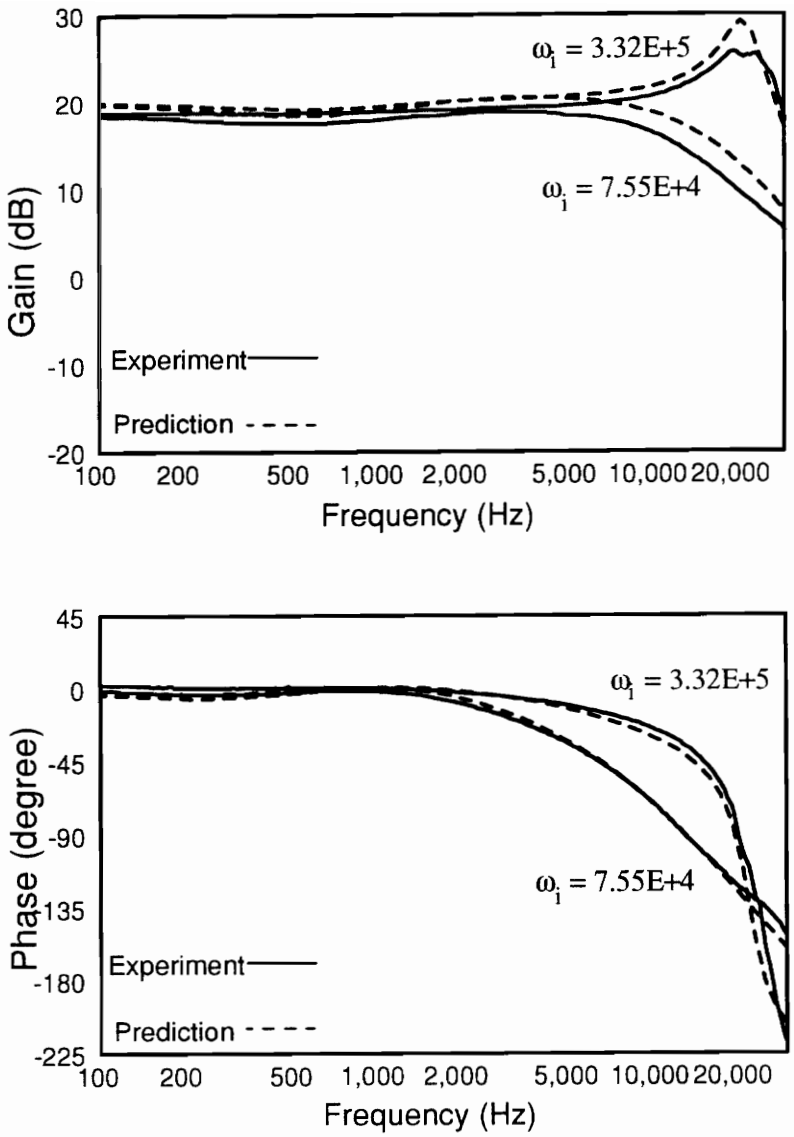

Figure 2.22. Measurement and prediction of the control-to-inductor current gain for a: *The solid line represents measurement, and the dashed line represents prediction. The switching frequency of the converter is 45 kHz.*

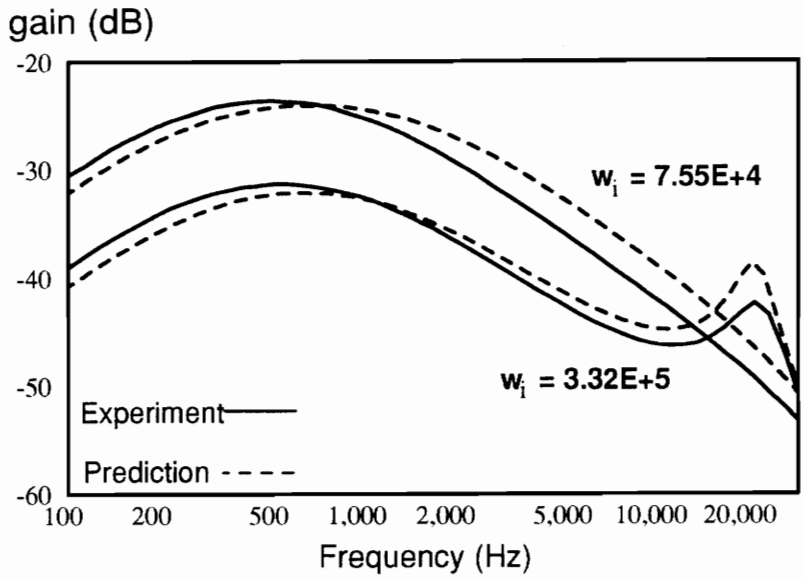

Figure 2.23. Measurement and prediction of the audio susceptibility for buck convert er: *The solid line represents measurement, and the dashed line represents prediction. The switching frequency of the converter is 45 kHz.*

ripple in the error voltage of ACM control is very high, as shown in Fig. 2.24. The sawtooth ramp slope should be large enough to prevent the error voltage intersecting the ramp more than once.

The current compensator has three parameters that need to be designed, the integrator gain, ω_i, the zero position, ω_z, and the pole position ω_p. To prevent minus two slope in the current loop gain, ω_z is placed before power stage resonant frequency, ω_o. Usually, ω_z is selected to be one third of ω_o:

$$\omega_z = \frac{1}{3}\omega_o; \tag{2.23}$$

ω_p is used to filter the switching ripple of the inductor current. If it is too small, it introduces large phase lag into both voltage and current loops. If it is larger than switching frequency, it has no filtering effect on the switching ripple. Hence, it is usually placed at half the switching frequency:

$$\omega_p = \frac{\omega_s}{2}. \tag{2.24}$$

After S_e, ω_z, and ω_p are determined, ω_i needs to be determined according to current loop stability requirement. The damping factor, Q_p, qiven by Eq. (2.13e) also indicates the current loop stability margin, and choosing $Q_p \leq 1$ gives proper current loop stability margin [18]. By letting $Q_p \leq 1$, we have:

$$D'(\xi + \frac{S_e}{S_n})\ \frac{\omega_z}{\omega_i} \geq \frac{1}{2} + \frac{1}{\pi}. \tag{2.25}$$

ω_i is solved from above equation:

$$\omega_i \leq \frac{S_e D' \omega_z}{S_n[\frac{1}{2} + \frac{1}{\pi} - DD'\omega_z T_s - D'(1 - \frac{\omega_z}{\omega_p})(1 - e^{-\omega_p DT_s})]}. \qquad (2.26)$$

Since the current loop phase margin is smaller when duty cycle is either very large or very small, as explained in Sec. 2.4.1, equation (2.26) should be satisfied for both D_{max} and D_{min}.

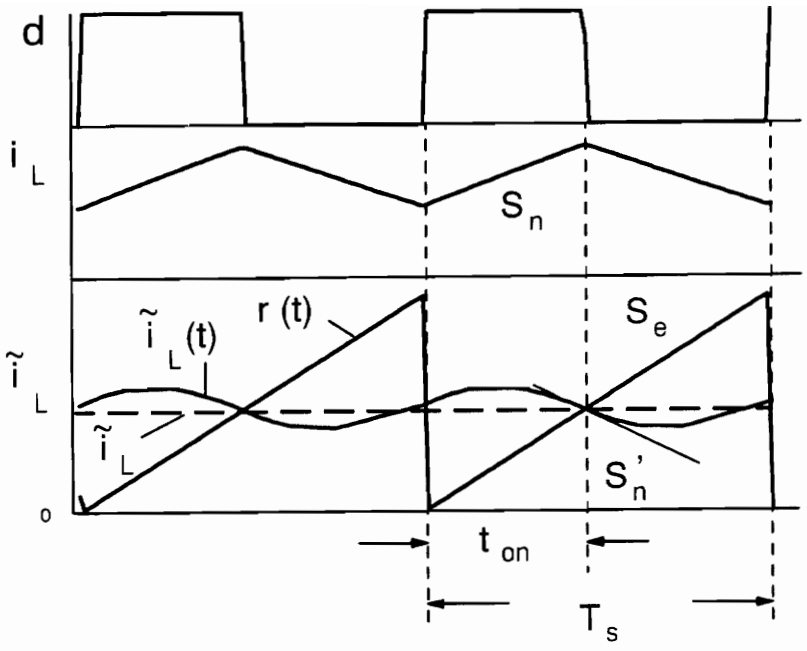

Figure 2.24. Selecting sawtooth ramp slope: *To insure the proper operation, the increment of the sawtooth ramp during the off-time should be larger than Δi_L. If Δi_L is larger than $S_e D' T_s$, i_L may intersect the ramp twice in one switching cycle, which will turn on the switch before the clock comes.*

2.7 Summary

The main feature of ACM control is its ability to control the average inductor current of a PWM converter. Due to this property, it can be applied to control a boost converter as the power factor correction circuit, or to control a buck converter as the battery charger of a spacecraft power system. The main difference between PCM and ACM controls is that ACM control has a high low-frequency gain in the current loop, which eliminates the dc error between average inductor current and the control. ACM control also eliminates the switching noise existing in the current sensing network of the PCM control.

The derived small-signal model is accurate up to half the switching frequency, which is necessary for the current loop design. The relationship between current loop instability and line voltage is found for the first time. Unlike PCM control, this relationship is not monotonic, and the current loop becomes unstable more easily when the duty cycle is either very small or very large. These findings are confirmed by time-domain simulations. The voltage loop stability margins of ACM and PCM controls are almost the same, due to their similar low-frequency control-to-output voltage characteristics. The audiosusceptibility of a converter with ACM control is smaller than that of one with PCM control. But in the buck converter case, totally cancelling audiosusceptibility with an external ramp is impossible for ACM control.

Based on the small-signal analysis, current loop design guidelines are proposed. To insure the proper operation, the sawtooth ramp slope should be larger than the sensed inductor current off-time slope, but over selecting S_e increases the audiosusceptibility of the converter. Subharmonic oscillation can be avoided by properly selecting the integrator gain of the current loop compensator according to both low line and high line operations.

The accuracy of the small-signal model for ACM control is confirmed with the measurements of a buck converter.

3. MODELING AND ANALYSIS OF CHARGE CONTROL

3.1 Introduction

The main feature of charge control is its ability to control the average switch current of a PWM converter. There are many applications in which the average switch current of a PWM converter needs to be controlled, such as buck or flyback PFC circuit. The existing control methods, such as PCM and ACM controls, have limitations on controlling this quantity.

In PCM control, the peak switch current is sensed and controlled. However, the average value of the switch current in one switching cycle cannot be represented by its peak value, whether the converter is operating in CCM or DCM. ACM control can control the average inductor current of a PWM converter. But when it is used to control the average switch current, the current loop crossover frequency is limited by the zero existing in the duty cycle-to-switch current transfer function [8]. Small current loop crossover results in the current being distorted from the control. The detailed discussions of this issue will be presented in Chapter IV, when ACM and charge controls are compared for flyback PFC application.

Like other current-mode controls, charge control also provides current sharing and limiting functions. Unlike PCM control, charge control has excellent noise immunity, since it uses the integration of the switch current as the control signal. There are certain advantages associated with charge control which do not exist in other current-mode controls, For example, charge control can be applied to converters, such as multi-resonant converters, where both PCM and ACM controls fail to control them [25].

The operation principle of charge control is studied in 3.2, and a complete small-signal model is derived. Subharmonic oscillation is found through small-signal analysis, and the relationship between the subharmonic oscillation and line/load condition of charge control is defined for the first time. This finding is verified by time-domain simulations. A design guideline

which can help avoid subharmonic oscillation for a given line/load range is provided. Finally, the small-signal model developed is confirmed experimentally.

3.2 Principle of Operation

The control scheme of charge control is illustrated in Fig. 3.1. The active switch in the power stage turns on at the beginning of each cycle, and the switch current is integrated to obtain its total charge. When the voltage across C_T reaches the control voltage, v_c, the switch in the power stage turns off, and the switch across capacitor C_T turns on to discharge C_T. C_T is totally discharged before the next switching cycle starts. Hence, the total charge of the switch current in one cycle, which is proportional to the average value of the switch current, is controlled. The steady-state waveforms of a buck converter employing charge control are shown in Fig. 3.2.

Subharmonic oscillation can be observed when a charge-controlled PWM converter operates at light load. As shown in Fig. 3.3, the switch turns on at time t = 0, and the initial value of inductor current is I_1. As the inductor current increases, the charge on capacitor C_T also increases. When v_T reaches the control voltage, v_c, the switch turns off, and the inductor current decreases.

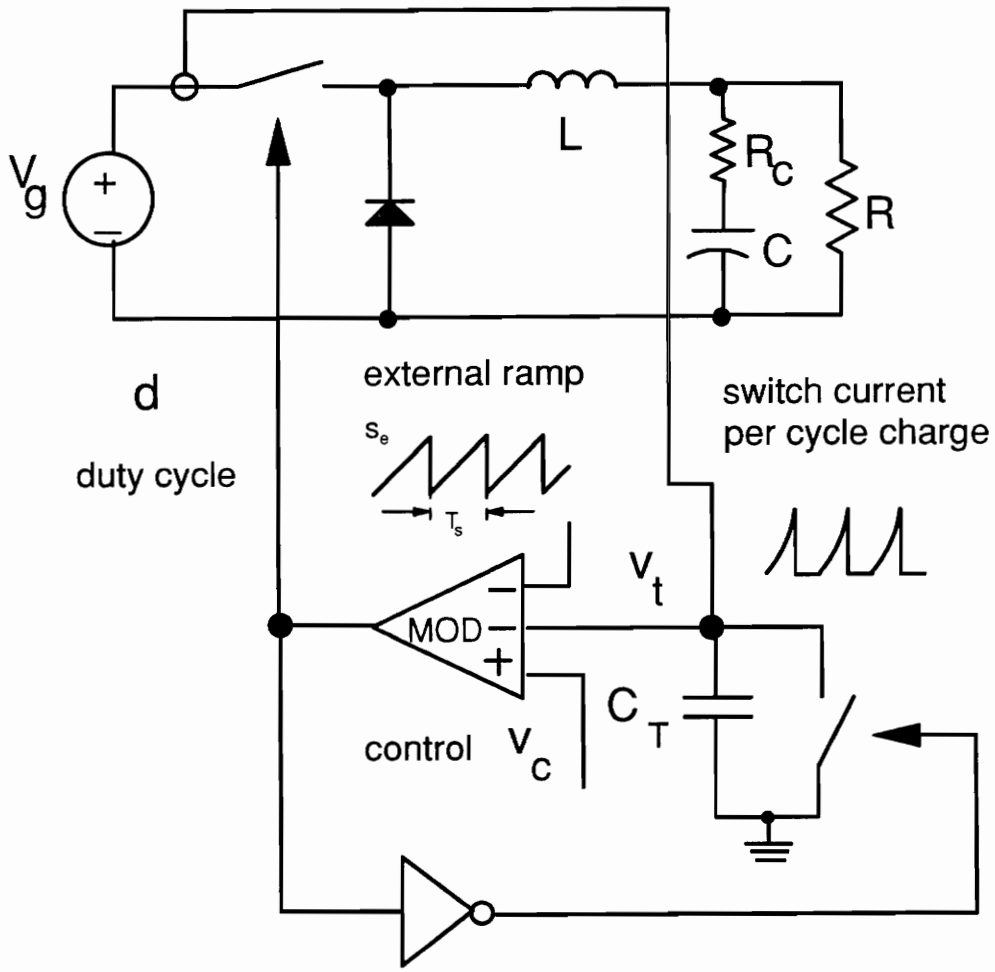

Figure 3.1. Control scheme of charge control: *In this control scheme, the switch current is sensed and charged to capacitor C_T. C_T is totally discharged before the next cycle, so the obtained feedback signal is the switch current charge of each cycle.*

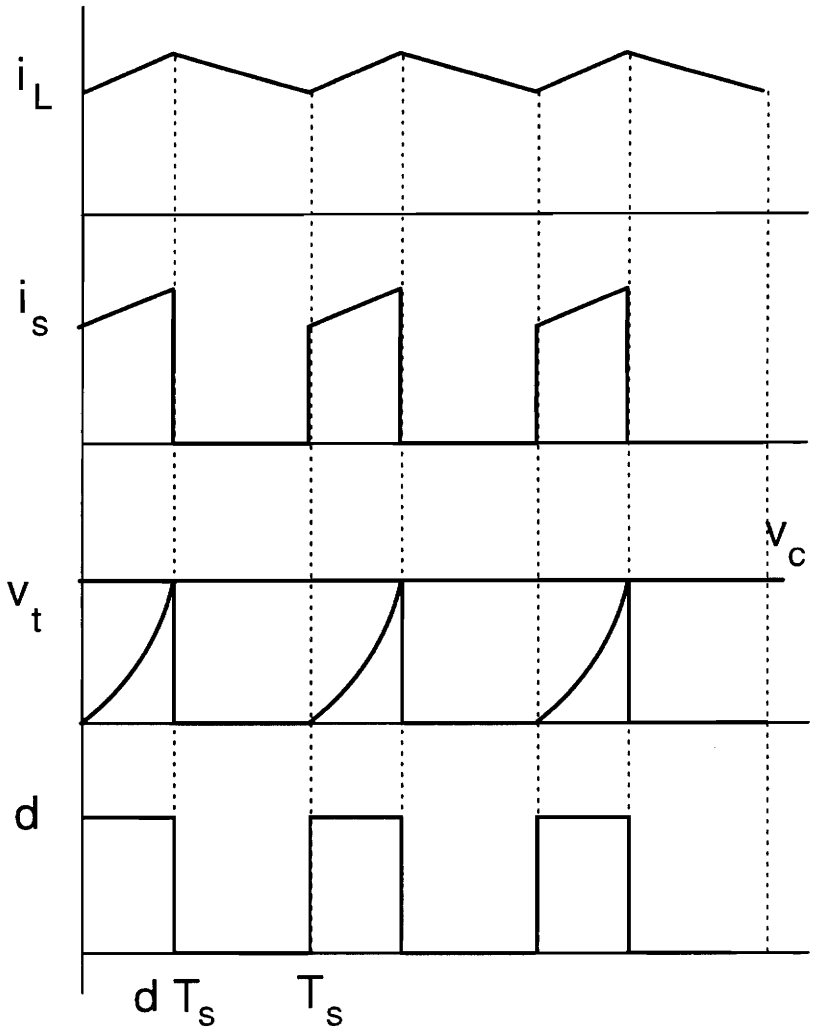

Figure 3.2. Steady-state waveforms of charge control: *i_L is the inductor current. i_s is the switch current. v_t is the charge of the switch current. When it reaches control voltage v_c, the main switch turns off.*

The switch is turned on again by the clock before the inductor current falls to I_1. Because $I_2 > I_1$, less time is required for v_T to reach v_c in the next cycle. Hence, an oscillation occurs in the system, with an oscillation frequency equal to half the switching frequency.

3.3 Small-Signal Modeling

3.3.1 Current Loop Modeling

In charge control, the switch current (equal to the on-time inductor current) is integrated and compared with the control voltage derived from the voltage feedback loop. Assuming that a perturbation in inductor current, $\hat{i}_L(k)$, is introduced at time $t = t_k + DT_s$, this perturbation affects the next switching instant, causing a perturbation in the switching time, $\hat{d}_{k+1}T_s$. Figure 3.4 shows the propagation of the perturbations. The steady-state waveforms are represented by solid lines, and the perturbed waveforms are represented by dotted lines. The perturbations on the input and output voltages and the control signal are assumed to be zero.

The relation between $\hat{i}_L(k)$ and $\hat{d}_{k+1}$ is derived as follows:

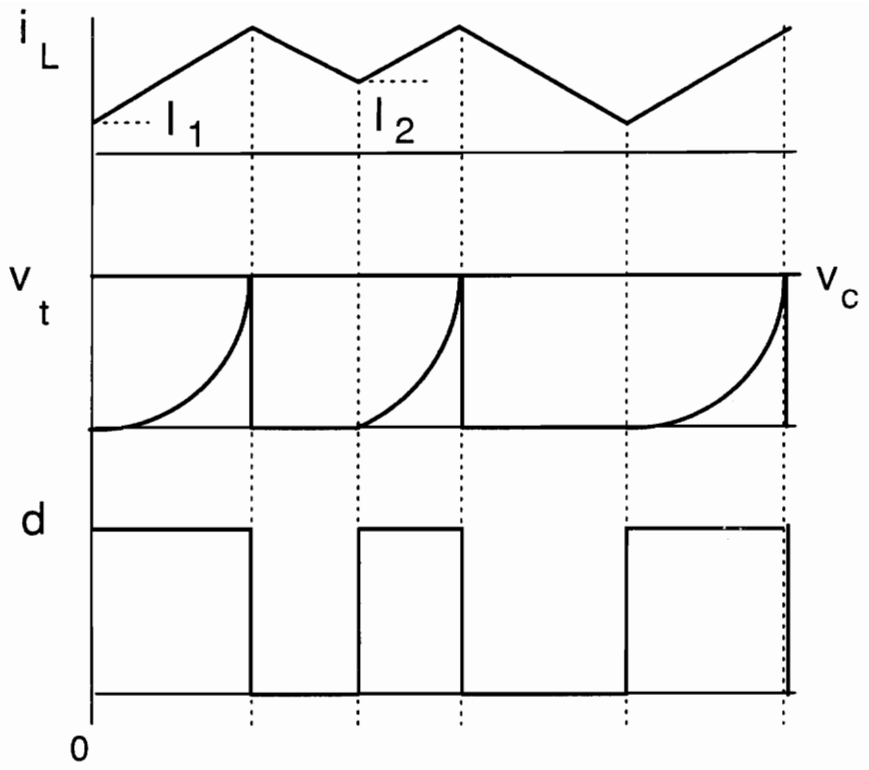

Figure 3.3. Subharmonic oscillation at light load: *With a small inductor current turn-on time value, it takes a longer time for v_t to reach v_c., and the turn on clock comes again before the inductor current discharges to I_1. Since I_2 is larger than I_1, it takes less time for v_t to reach the same control, v_c.*

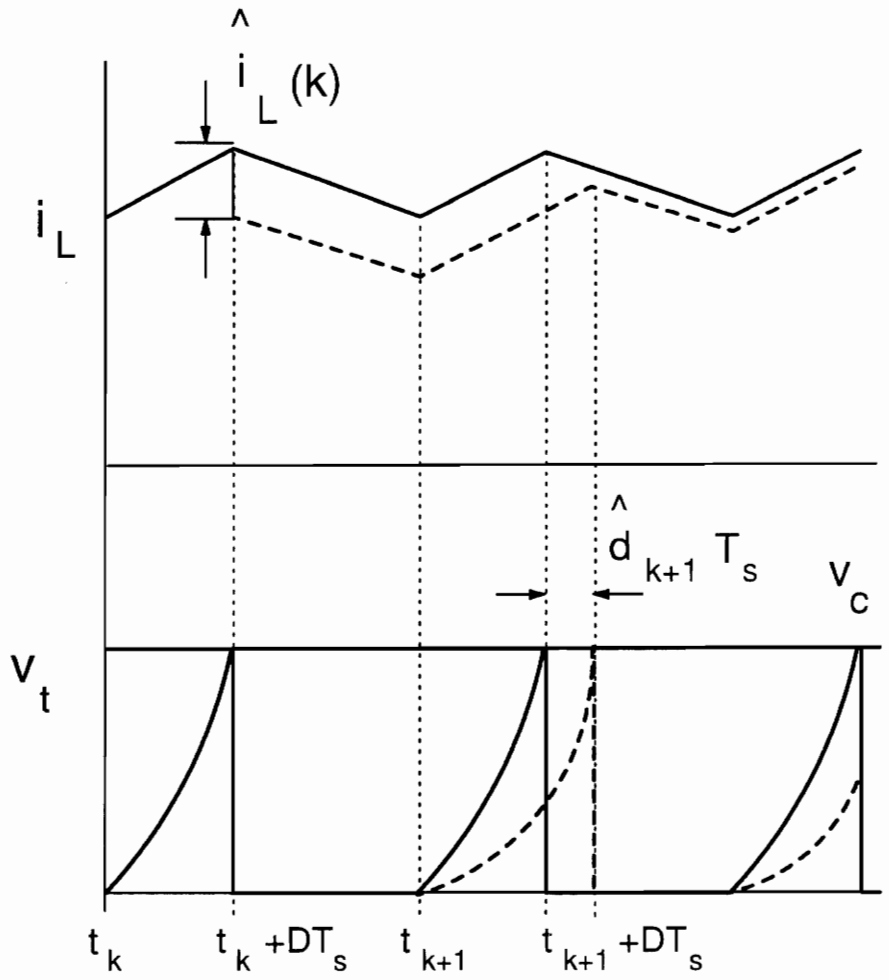

Figure 3.4. Propagation of the perturbations in charge control: *A perturbation in inductor current at $t = t_k + DT_s$ produces a perturbation in the on-time at $t = t_{k+1} + DT_s$. The perturbation of the inductor current is held for almost one switching cycle.*

$$\int_{t_k}^{t_k+DT_s} i_L(t)dt = \int_{t_{k+1}}^{t_{k+1}+(D+\hat{d}_{k+1})T_s} \left[i_L(t) + \hat{i}_L(k)\right]dt =$$

$$= \int_{t_{k+1}}^{t_{k+1}+DT_s} i_L(t)dt + \int_{t_{k+1}+DT_s}^{t_{k+1}+(D+\hat{d}_{k+1})T_s} i_L(t)dt +$$

$$+ \int_{t_{k+1}}^{t_{k+1}+DT_s} \hat{i}_L(k)dt + \int_{t_{k+1}+DT_s}^{t_{k+1}+(D+\hat{d}_{k+1})T_s} \hat{i}_L(k)dt. \qquad (3.1)$$

In the steady state,

$$\int_{t_k}^{t_k+DT_s} i_L(t)dt = \int_{t_{k+1}}^{t_{k+1}+DT_s} i_L(t)dt, \qquad (3.2)$$

since $\hat{d}_{k+1} << D$,

$$\int_{t_{k+1}+DT_s}^{t_{k+1}+(D+\hat{d}_{k+1})T_s} i_L(t)\,dt \simeq I_{Lp}\,\hat{d}_{k+1}T_s, \qquad (3.3)$$

where I_{Lp} is the peak inductor current. Since $\hat{i}_L(k)$ is a constant at [t_{k+1}, $t_{k+1} + DT_s$], then:

$$\int_{t_{k+1}}^{t_{k+1}+DT_s} \hat{i}_L(k)dt = DT_s\hat{i}_L(k). \qquad (3.4)$$

Substituting Eq. (3.2), Eq. (3.3), and Eq. (3.4) into Eq. (3.1):

$$\hat{i}_L(k) = -\frac{I_{Lp}}{D}\hat{d}_{k+1} \tag{3.5}$$

Equation (3.5) shows that the change in inductor current depends upon the change of the duty cycle. The duty cycle $\hat{d}$ is the sampled input, and the variable $\hat{i}_L(k)$ is the 'held' variable of the system, which remains constant from time $t_k + DT_s$ to time $t_{k+1} + DT_s$. Since the relation between i_L and d is discrete, the z-transformation is used. The correct z-transformation representation is:

$$\hat{i}_L(z) = -\frac{I_{Lp}}{D} z\,\hat{d}(z). \tag{3.6}$$

The corresponding sampled continuous-time expression [18] is:

$$\hat{i}_L(s) = -\frac{I_{Lp}}{D} e^{sT_s} \frac{(1 - e^{-sT_s})}{sT_s}\hat{d}(s). \tag{3.7}$$

It can be seen from Eq. (3.7) that if there is a perturbation in the inductor current, a perturbation in the duty cycle is produced. Hence, in the small-signal sense, there exists an equivalent inductor current feedback loop in charge control. The transfer function of the feedback loop is given by Eq. (3.7). To model the current feedback loop, the small-signal model shown in Fig. 3.5 is used. The inductor current-to-duty cycle transfer function can be derived from Fig. 3.5:

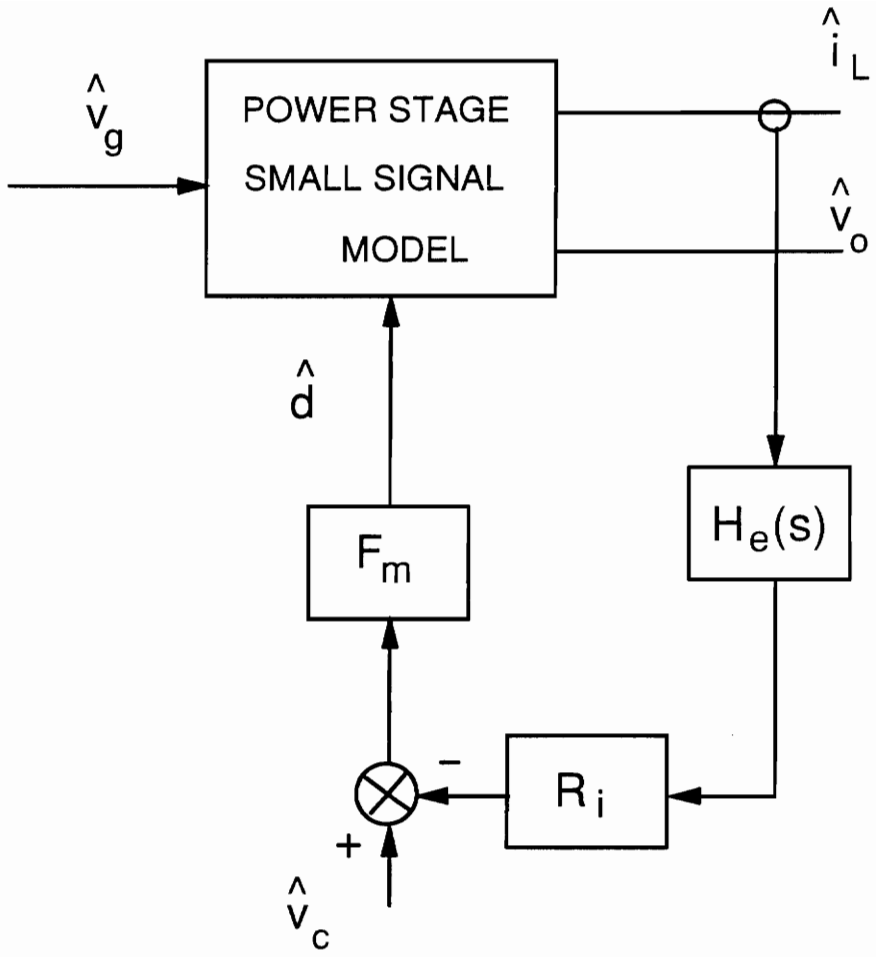

Figure 3.5. Small-signal model of the current feedback loop of charge control: *F_m is the modulator gain, $H_e(s)$ represents the sampled-and-hold effect in the current loop. R_i is the current gain which converts current signal to voltage signal.*

$$\frac{\hat{d}(s)}{\hat{i}_L(s)} = -F_m R_i H_e(s). \tag{3.8}$$

By comparing Eq. (3.7) and (3.8), we have:

$$F_m R_i = \frac{D}{I_{Lp}} \tag{3.9}$$

$$H_e(s) = \frac{sT_s}{e^{sT_s} - 1}. \tag{3.10}$$

F_m and R_i are the modulator gain and the equivalent current gain, respectively. $H_e(s)$ represents the sampled-and-hold effect in the current loop, which has the same expression as the sampling gain in PCM control [18]. A continuous-time expression is as follows [18]:

$$H_e(s) = 1 + \frac{s}{\omega_n Q_z} + \frac{s^2}{\omega_n^2}, \tag{3.11}$$

where

$$\omega_n = \frac{\pi}{T_s}, \tag{3.12}$$

$$Q_z = -\frac{2}{\pi}. \tag{3.13}$$

3.3.2 Modulator and Equivalent Current Gains

The modulator gain, F_m, can be derived from the input and output waveforms of the modulator. As shown in Fig. 3.6, it is assumed that a perturbation on the control voltage, $\hat{v}_c(k)$, is introduced to the system at time t_o, it produces a perturbation on the on-time , $\hat{d}_k T_s$. Assuming no perturbations on the line and output voltages, we have:

$$\hat{v}_c(k) = \frac{1}{C_T} \int_{t_k + DT_s}^{t_k + (D + \hat{d}_k)T_s} [i_L(t) + \hat{i}_L(k)]dt. \tag{3.14}$$

By ignoring the product of the perturbations term:

$$F_m = \frac{\hat{d}_k}{\hat{v}_c(k)} = \frac{C_T}{I_{Lp}\, T_s}. \tag{3.15}$$

By comparing Eqs. (3.9) and (3.15), the equivalent current gain is obtained:

$$R_i = \frac{DT_s}{C_T}. \tag{3.16}$$

The current gain, R_i, is a function of line voltage.

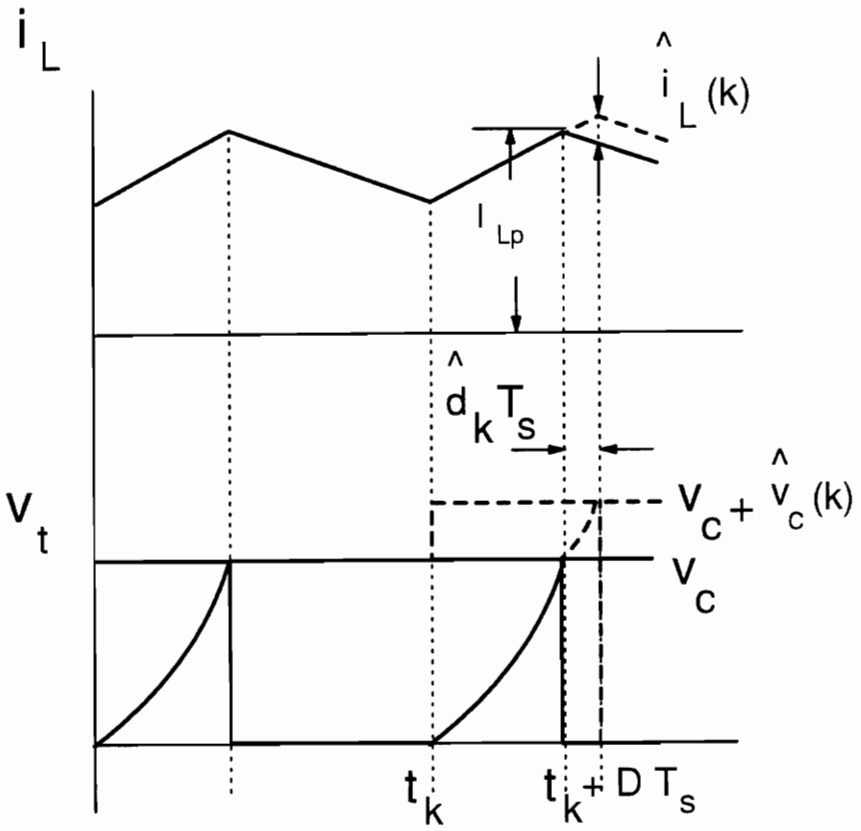

Figure 3.6. Derivation of the modulator gain: *Assuming there is a perturbation on the control voltage, v_c, at time t_o, it produces a perturbation on the duty cycle d. The modulator gain F_m is the ratio of the duty cycle perturbation, $\hat{d}$, to the control voltage perturbation, $\hat{v}_c$*

3.3.3 Feedback and Feedforward Gains

In charge control, the charge of the switch current in one cycle is used as the feedback control signal to modulate the duty cycle. Since the charge is a function of the input and output voltages, the duty cycle is perturbed if the input or output voltage is perturbed. Figure 3.7 shows how the duty cycle of a buck converter with charge control is affected by an input voltage perturbation, assuming that such a perturbation appears at time $t = t_o$. The slope of the switching current is then changed immediately, as shown in the dotted line. v_t takes less time to reach the same control voltage, v_c, than in the previous cycle, which introduces a perturbation on the duty cycle. This means that a line voltage increment produces an immediate duty cycle decrement. To model the effects of the perturbations of input as well as output voltages on the duty cycle, feedback and feedforward gain terms from input and output voltages are employed.

To study the relationship between the perturbations of input and output voltages and the duty cycle perturbation, the relation between control voltage and inductor current is found from Fig. 3.2:

$$v_c(t) = \frac{1}{C_T} \int_0^{dT_s} i_L(t)\, dt. \tag{3.17}$$

By averaging Eq. (3.17):

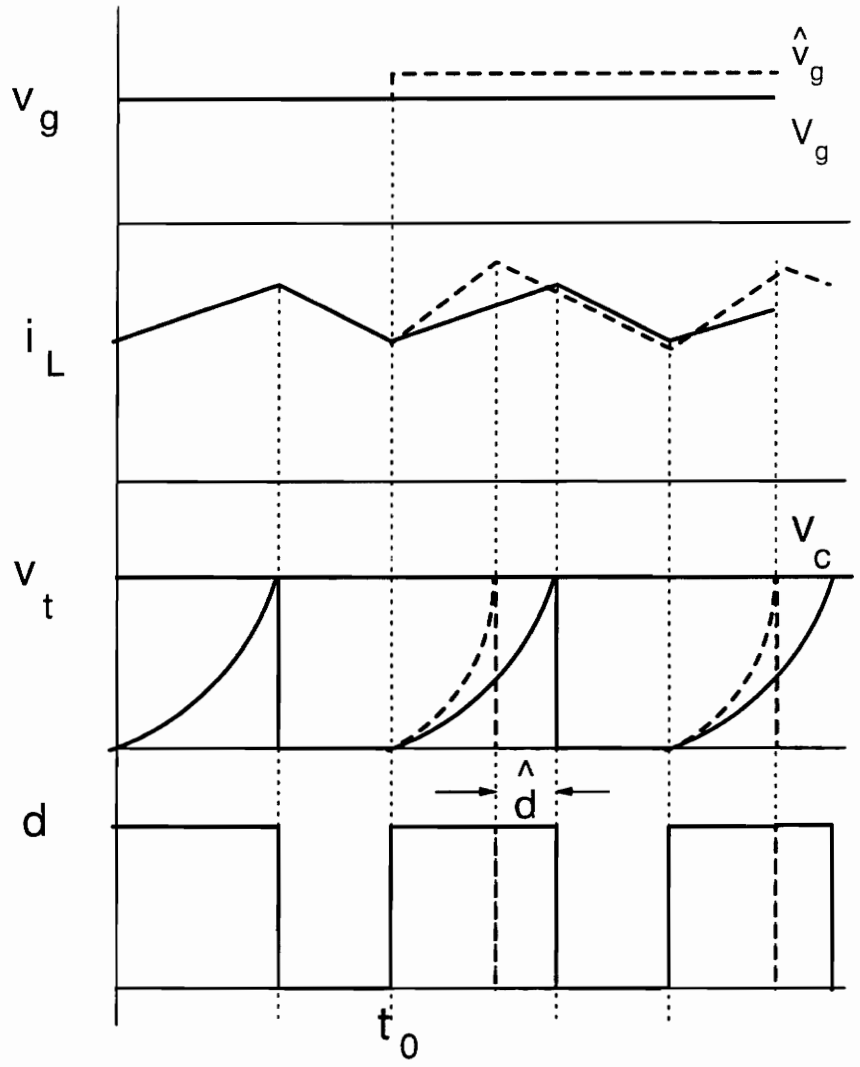

Figure 3.7. Input voltage feedforward in charge control: *A perturbation on the line voltage changes the on-time slope of the inductor current and it produces a change in the charge of the current during on-time and in the duty cycle immediately.*

$$v_c = \frac{1}{C_T} i_L \, d \, T_s, \tag{3.18}$$

where i_L denotes the average quantity of the inductor current, which is a function of the input and output voltages. By perturbing Eq. (3.18), with input and output voltages being fixed respectively, the input and output voltages to duty cycle transfer functions can be obtained, respectively. The same transfer function can also be obtained from the complete small-signal model shown in Fig. 3.8, with k_r and k_f as the unknowns. By comparing these transfer functions, k_r and k_f can be obtained.

The detailed derivations of k_r and k_f for basic PWM converters are included in Appendix B. The feedback and feedforward gains for three basic PWM converters are listed in Table 2.

Table 2. Feedforward and Feedback Gains for Charge Control

	BUCK	BOOST	BUCK/BOOST
k_f	$-\frac{R_i D D' T_s}{2L}$	$-\frac{R_i D' T_s}{2L}$	$-\frac{R_i D D' T_s}{2L}$
k_r	$\frac{R_i D' T_s}{2L}$	$\frac{R_i D'^2 T_s}{2L}$	$\frac{R_i D'^2 T_s}{2L}$

3.3.4 Complete Small-Signal Model

After feedback and feedforward gains are derived, the complete small-signal model for PWM converters employing charge control is obtained. The obtained model is uniform for all PWM converters.

3.4 Small-Signal characteristics

The small-signal characteristics of charge-controlled PWM converters are studied in this section. A buck converter is used as the power stage. To gain the physical insight into the control system, the approximate expressions of the characteristics are also derived.

3.4.1 Current Loop Gain

Ignoring the gain term k_r, the approximate expression of the current loop gain of charge control is as follows:

$$T_i(s) \simeq F_m R_i G_{id}(s)\, H_e(s), \tag{3.19}$$

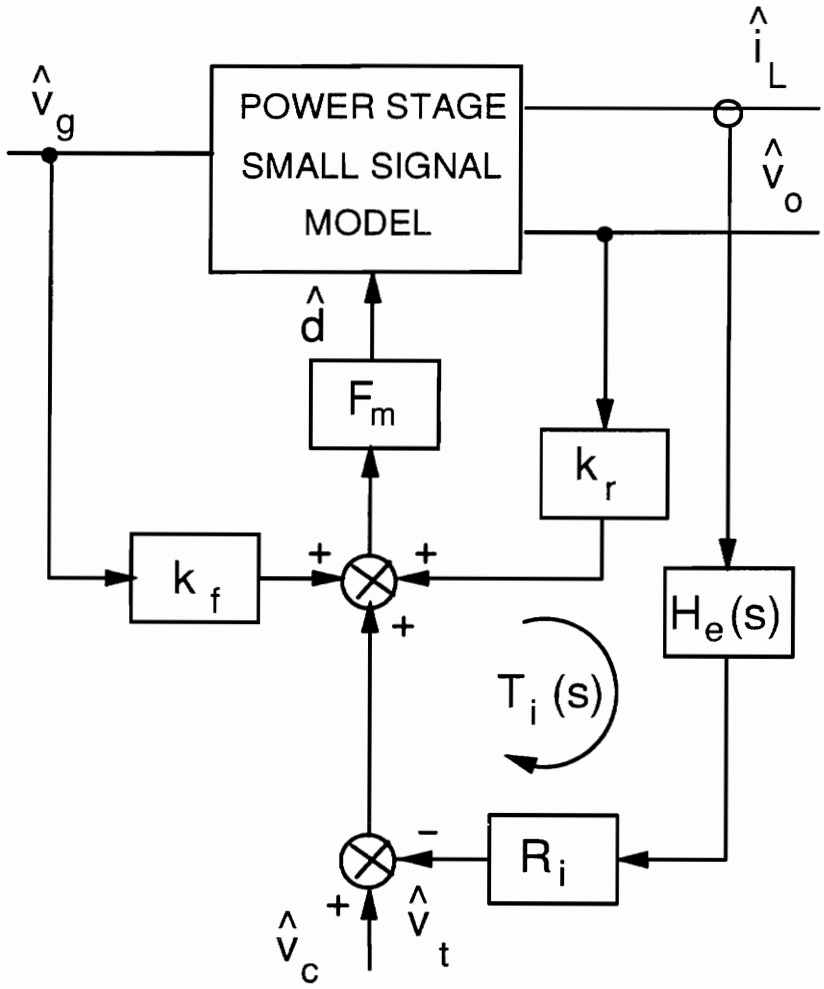

Figure 3.8. Complete small-signal model of charge control: *The obtained model can be used to analyze the stability of both current and voltage loops. It can also be used to study the dynamic performance of the system.*

where $G_{id}(s)$ is the power stage duty cycle-to-inductor current gain. $F_m R_i$ is given by Eq. (3.9), which has the following general form for all PWM converters:

$$F_m R_i = \frac{1}{\frac{I_c}{D} + \frac{D' V_{ap}}{2LF_s}}. \tag{3.20}$$

V_{ap} and I_c are terminal voltage and current of the three-terminal PWM switch model [23]. The current loop stability is determined by the high-frequency characteristics of the current loop gain. The high-frequency (after power stage resonant frequency) duty cycle-to-inductor current gain of all PWM converters is as follows:

$$G_{id}^{h}(s) \simeq \frac{V_{ap}}{sL}. \tag{3.21}$$

For three basic PWM converters with charge control, the high-frequency approximation of the current loop gain is as follows:

$$T_i^{h}(s) \simeq \frac{F_s}{\frac{F_s L}{R_e} + \frac{D'}{2}} \cdot \frac{H_e(s)}{s}, \tag{3.22a}$$

where for a buck converter:

$$R_e = R; \tag{3.22b}$$

for a boost converter:

$$R_e = DD'R; \tag{3.22c}$$

for a buck/boost converter:

$$R_e = D'R. \tag{3.22d}$$

By defining the normalized load resistance R_n as:

$$R_n = \frac{R_e}{LF_s}, \tag{3.23}$$

Eq. (3.22) becomes:

$$T_i^h(s) \simeq \frac{F_s}{\frac{1}{R_n} + \frac{D'}{2}} \frac{H_e(s)}{s}. \tag{3.24}$$

It can be seen that both line voltage and load current affect the current loop crossover frequency, and the current loop has higher gain, thus less phase margin at light load. Figure 3.9 shows current loop gain of charge-controlled buck converter with different operation conditions. It can be seen from Fig. 3.9 that at heavy load, the current loop has positive phase margin even the duty cycle is larger than fifty percent. At light load, the current loop gain does not has positive phase margin if the duty cycle is very large.

The relationship between the converter operation conditions and the current loop stability is found for the first time through the small-signal analysis. The results is quite different from both PCM and ACM control, where the current loop instability is independent of load current. To verify the small-signal predictions, the time-domain simulation is performed. The simulation results are shown in Fig. 3.10. They confirm the small-signal predictions.

3.4.2 Control-to-Output Gain

The control-to-output gain is defined as the control voltage to output voltage transfer function. An approximated expression of control-to-output gain for a buck converter is given as follows:

$$\frac{\hat{v}_o}{\hat{v}_c} \simeq \frac{R}{2R_i} \frac{(1 + R_c Cs)}{(1 + \frac{RC}{2} s)} F_h(s), \tag{3.25a}$$

where

$$F_h(s) = \frac{1}{1 + \frac{s}{\omega_n Q_p} + \frac{s^2}{\omega_n^2}}, \tag{3.25b}$$

$$\omega_n = \frac{\pi}{T_s}, \tag{3.25c}$$

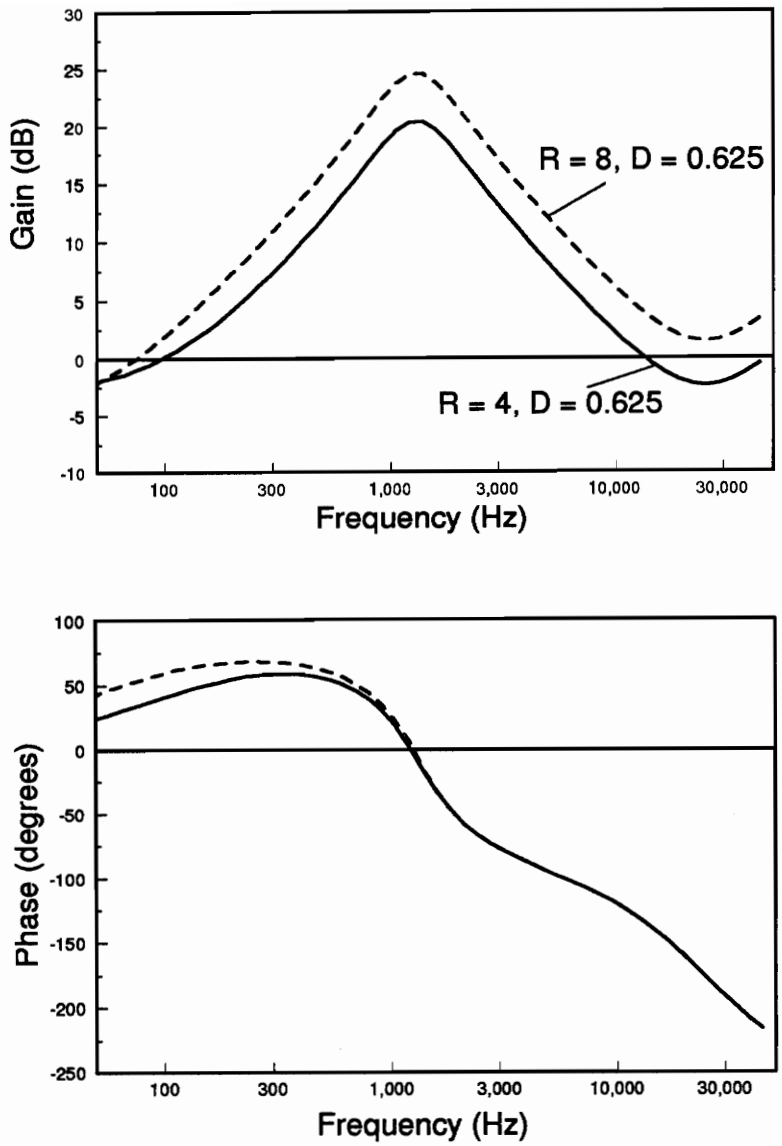

Figure 3.9. Current loop gain of a buck converter with different operation condition: *Both line voltage and load current affect the current loop crossover frequency. The low-line, light load operation causes current loop to be unstable.*

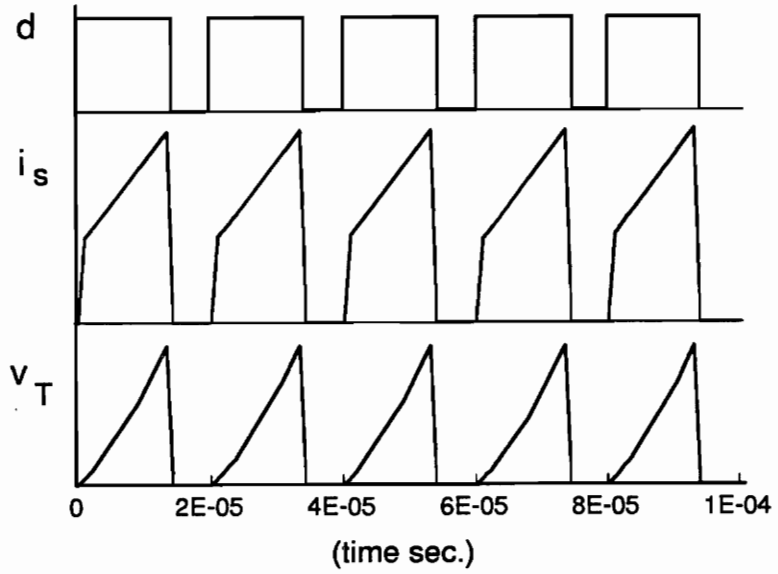

(a) R = 4, D = 0.625, L =37.5 uH, Fs = 50 kHz

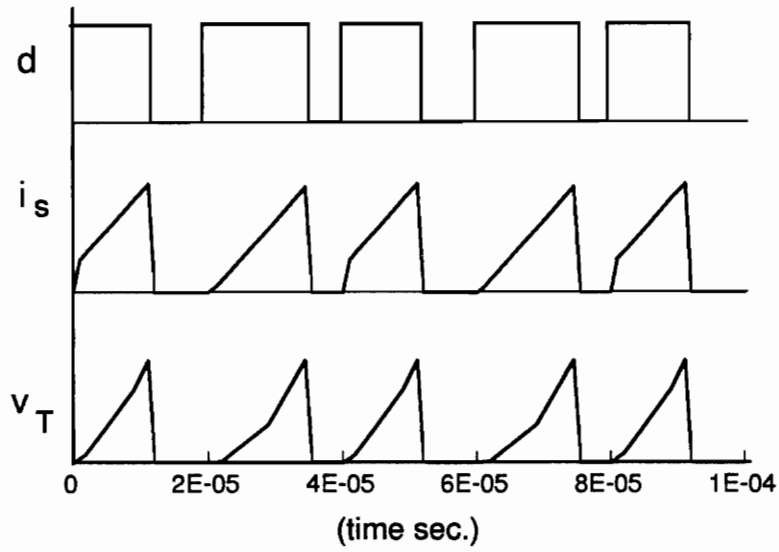

(b) R = 8, D = 0.625, L =37.5 uH, Fs = 50 kHz

Figure 3.10. Open loop time-domain simulation results of charge control: *At heavy load condition, the current loop is stable even the duty cycle is larger than fifty percent. This results is quite different from that of PCM control.*

and

$$Q_p = \frac{1}{\pi\left(\frac{LF_s}{R_e} - \frac{D}{2}\right)}, \qquad (3.25d)$$

where R_e is given by Eq. (3.22). The damping factor, Q_p, given by Eq. (3.24d) is general for all PWM converters. The detailed derivation of it can be found in Appendix B.

The control-to-output gain of charge control is shown in Fig. 3.11, with a buck converter as the power stage. As can be seen from Fig. 3.11, the transfer functions have a single pole at low-frequencies and a pair of complex poles at half the switching frequency. This is similar to the control-to-output transfer function of PCM control with the current loop closed. The low-frequency single pole characteristic makes the voltage loop compensation much easier than for voltage-mode control. Different from PCM and ACM control, the low-frequency characteristics are line-dependent, and high line operation gives the worst case condition for voltage feedback loop design.

Like in PCM and ACM control cases, Q_p can be used to predict the current loop instability. When Q_p is very large, the peaking of $F_h(s)$ is very large, which indicates that current loop has a small or even negative phase margin. It is more convenient to design current loop according to Q_p.

It can be seen from Eq. (3.25d), that when

$$\frac{LF_s}{R_e} < \frac{D}{2}, \tag{3.26}$$

Q_p becomes negative, the double poles move into the right-half plane, and the system becomes unstable. For PCM control, the subharmonic oscillation is only related to duty cycle. When duty cycle is larger than fifty percent, the subharmonic oscillation occurs. In charge control, it is related to duty cycle as well as to power stage filter inductance, switching frequency, and load resistance. The current loop has less phase margin when the converter is operating at light load. The current loop compensation is more difficult when converter operates in a wide load range.

3.4.3 Control-to-Switch Current Gain

The control-to-switch current gain is defined as the control voltage to average switch current transfer function. This transfer function indicates the control ability of the control scheme on the average switch current. The approximate expression of the transfer function, with buck converter as the power stage, is as follows:

$$\frac{\hat{i}_s}{\hat{v}_c} \simeq \frac{D}{R_i} F_h(s) = \frac{C_T}{T_s} F_h(s), \tag{3.27}$$

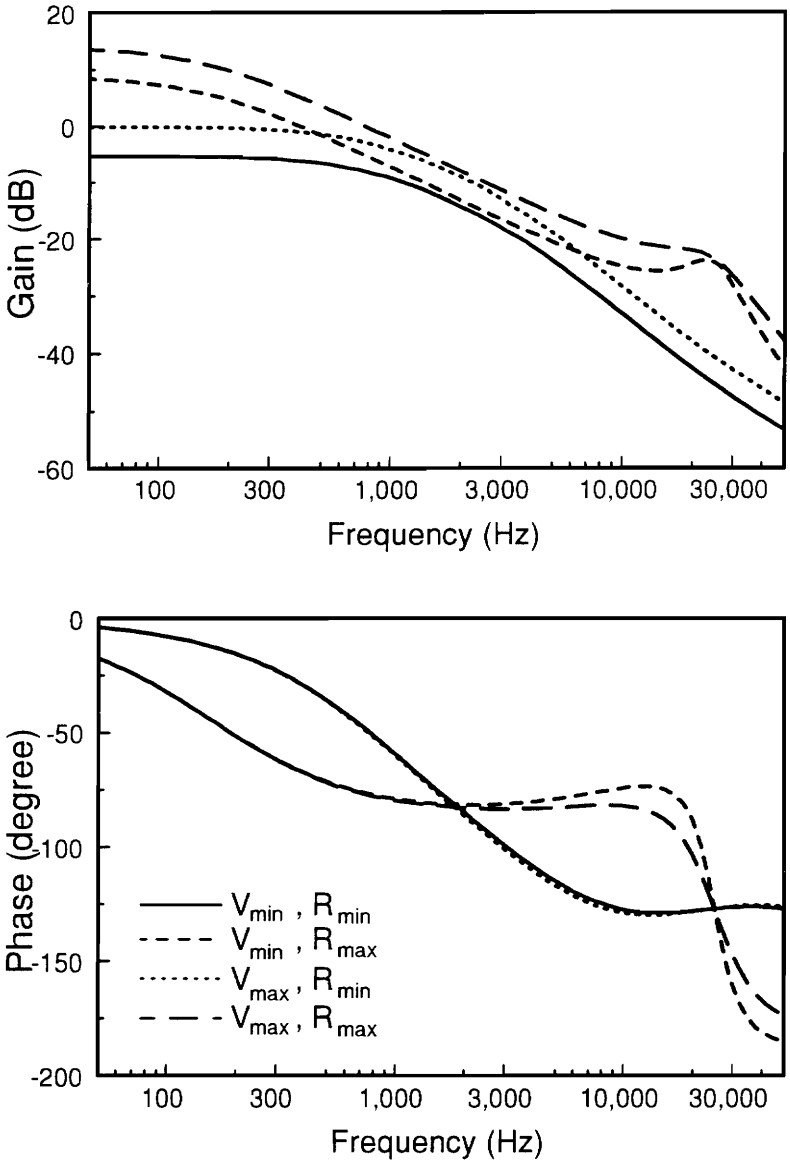

Figure 3.11. Control-to-output gain of a buck converter with charge control: *Both low-frequency and high-frequency characteristics are functions of the line voltage and load current. The middle-frequency characteristic is independent of the load.*

where $F_h(s)$ is given by Eq. (3.25). It can be seen from Eq. (3.27) that up to half the switching frequency, the control-to-switch current gain is only determined by capacitor C_T and the switching frequency of the converter. It means that no matter how the operation conditions change, the average switch current always follows the control voltage with no distortion. The control-to-switch current gain of a buck converter with charge control is shown in Fig. 3.12.

The reason that charge control can control average switch current is that the average switch current is proportional to the charge obtained by C_T. According to the definition, the average switch current equals:

$$i_s = \frac{1}{T_s}\int_0^{DT_s} i_s(t)dt \tag{3.28}$$

The charge of the switch current obtained by C_T:

$$v_t = \frac{1}{C_T}\int_0^{DT_s} i_s(t)dt \tag{3.29}$$

It can be seen from Eqs. (3.28) and (3.29) that i_s is proportional to v_t, and the ratio of them equals the gain of Eq. (3.27).

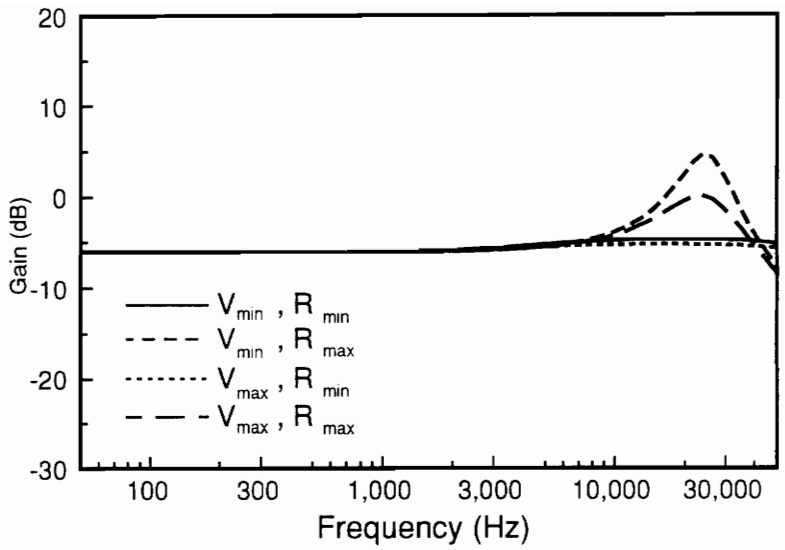

Figure 3.12. Control-to-switch current gain of charge control: *The characteristic of charge control is flat up to half the switching frequency. The magnitude of the gain characteristic is independent of converter operating conditions.*

3.5 Adding an External Ramp

In certain applications where the load range is very large, an external ramp is needed to stabilize the system. From a small-signal point of view, adding an external ramp only changes the modulator gain of the system.

The modulator gain of charge control with an external ramp added is derived in this section. The circuit diagram of charge control with external ramp is shown in Fig. 3.13 (a). The steady-state waveforms are shown in Fig. 3.13 (b) with solid lines. The following steady-state equation can be obtained:

$$V_c = \frac{1}{C_T}\int_0^{DT_s} i_L(t)\,dt + S_e D T_s, \tag{3.30}$$

where S_e is the external ramp slope. Assuming the control voltage is perturbed at time $t = t_o$, as shown in the dotted line of Fig. 3.13 (b), we have:

$$V_c + \hat{v}_c = \frac{1}{C_T}\int_0^{D+\hat{d}} i_L(t)\,dt + S_e(D+\hat{d})T_s. \tag{3.31}$$

Subtracting the steady-state from Eq.(3.31):

$$\hat{v}_c = \frac{1}{C_T} I_{Lp}\hat{d}T_s + S_e\hat{d}T_s, \tag{3.32}$$

the modulator gain is obtained:

$$F_m = \frac{\hat{d}}{\hat{v}_c} = \frac{D}{(I_{Lp} + S_e C_T)R_i}. \tag{3.33}$$

3.6 Design Guidelines

The current feedback loop of charge control has two parameters that need to be determined: the capacitor, C_T, and the external ramp slope, S_e.

The first step of the design is to determine capacitor, C_T. The value of the voltage across capacitor, C_T, is determined by both the integration of the on-time inductor current and capacitance, C_T:

$$v_t = \frac{1}{C_T}\int_0^{DT_s} i_L(t)dt, \tag{3.34}$$

For proper operation, v_t should never exceed the comparator supply voltage, v_{cs}, when the converter is operating in heavy load and low line case; hence, C_T is chosen as follows:

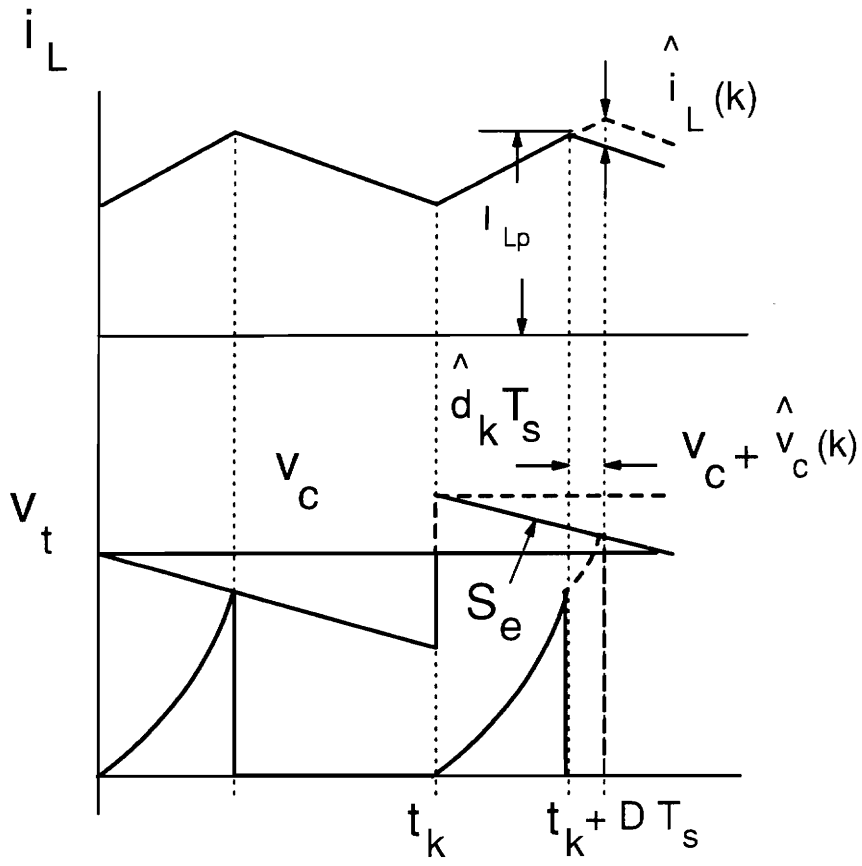

Figure 3.13. Modulator gain after an external ramp is added: *The external ramp is added to the modulator directly. After the external ramp is added, the charge of the switch current is now following the control voltage, subtracting the voltage drop, S_eDT_s*

$$C_T > \frac{1}{V_{cs}} \int_0^{D_{max}T_s} i_{L,\max}(t)dt. \tag{3.35}$$

The resonance at half the switching frequency in control-to-output gain is the frequency domain representation of subharmonic oscillation. To prevent subharmonic oscillation, this resonant peak needs to be damped, but over-damping the resonant peak is undesirable. It will split high frequency complex poles and push one of them to the lower frequency, causing a reduction of the phase margin of the voltage loop. To properly damp the resonant peak, the damping factor, Q_p, is set as less than or equal to one at high line and light load. From Eq. (3.25d), we have:

$$\frac{1}{\pi\left(\frac{LF_s}{R_{e,\max}} - \frac{D_{max}}{2}\right)} \leq 1. \tag{3.36}$$

The next step of the design is to check whether Eq. (3.36) is satisfied for the given power stage parameters. If Eq. (3.36) is satisfied, there is no need for an external ramp. If it is not satisfied, an external ramp is needed. The derivation of Q_p as the function of the external ramp slope, S_e, can be found in appendix B. For all PWM converters, it has the following general form:

$$Q_p = \frac{1}{\pi\left(\frac{LF_s}{R_e} + \frac{F_s LC_T S_e}{V_{cp}} - \frac{D}{2}\right)}. \tag{3.37}$$

By setting Q_p to be less than or equal to one, S_e is obtained:

$$S_e \geq \frac{V_{cp}}{F_s L C_T} \left(\frac{1}{\pi} + \frac{D}{2} + \frac{L F_s}{R_e} \right). \tag{3.38}$$

3.7 Experimental Verifications

A buck converter with charge control was built to verify the small signal model. The circuit components values are as follows:

$V_g = 15\ V$,

$L = 37.5\ \mu H$,

$C = 380\ \mu F$,

$R_c = 20\ m\Omega$,

$F_s = 90\ kHz$, and

$C_T = 733\ nF$.

To verify the prediction of current feedback loop, the current loop gain (shown in Fig. 3.8 as $T_i(s)$) was measured. The digital modulator was employed to ensure the correct sample data measurement. The measurement of the current loop gain of charge control is shown in Fig. 3.14. Its shape is the same as that of PCM control. The double right-half-plane zeroes, caused by the sample-and-hold effect of the current loop, can be observed from the measurement.

The measured and predicted control-to-output gains are shown in Fig. 3.15. Figure 3.16 shows the measurement and prediction of the control-to-inductor current gain. In both cases, the predictions agree well with the measurements.

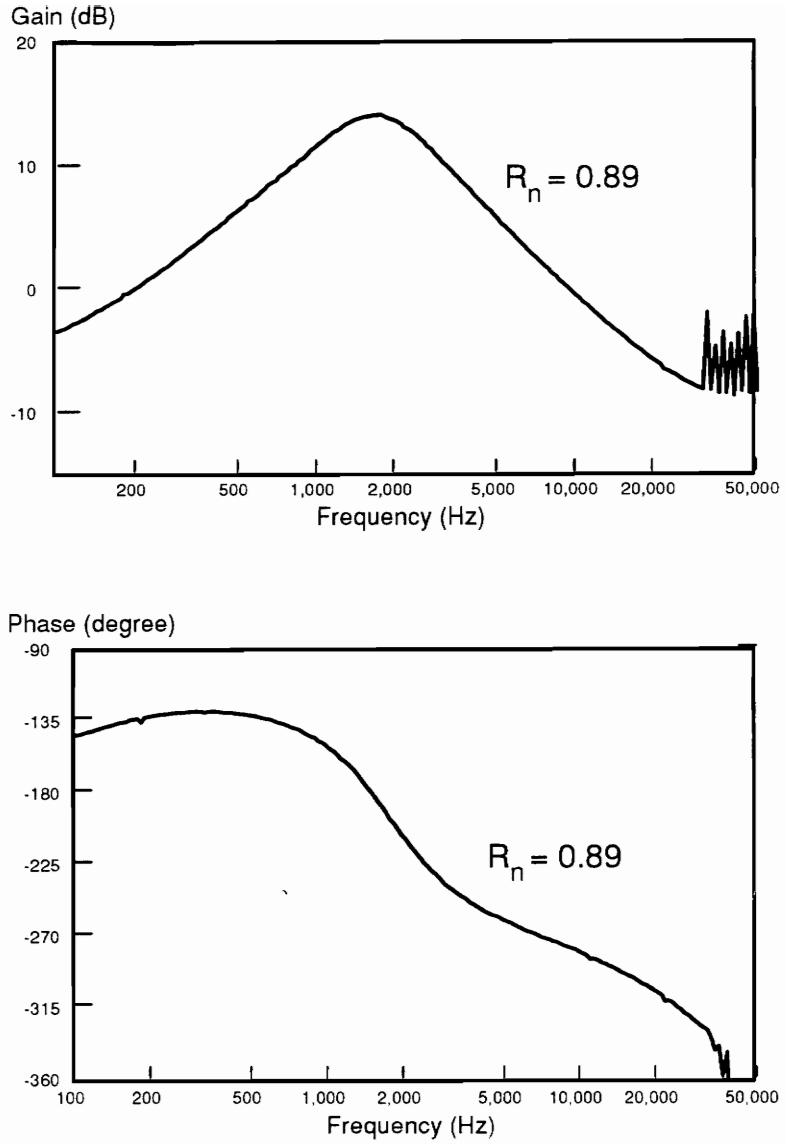

Figure 3.14. Measurement of the current loop gain of charge control: *The switching frequency of the experiment circuit is 90 kHz. The double right-half-plane zeroes at half the switching frequency caused by the sampling effect can be seen from the measurement.*

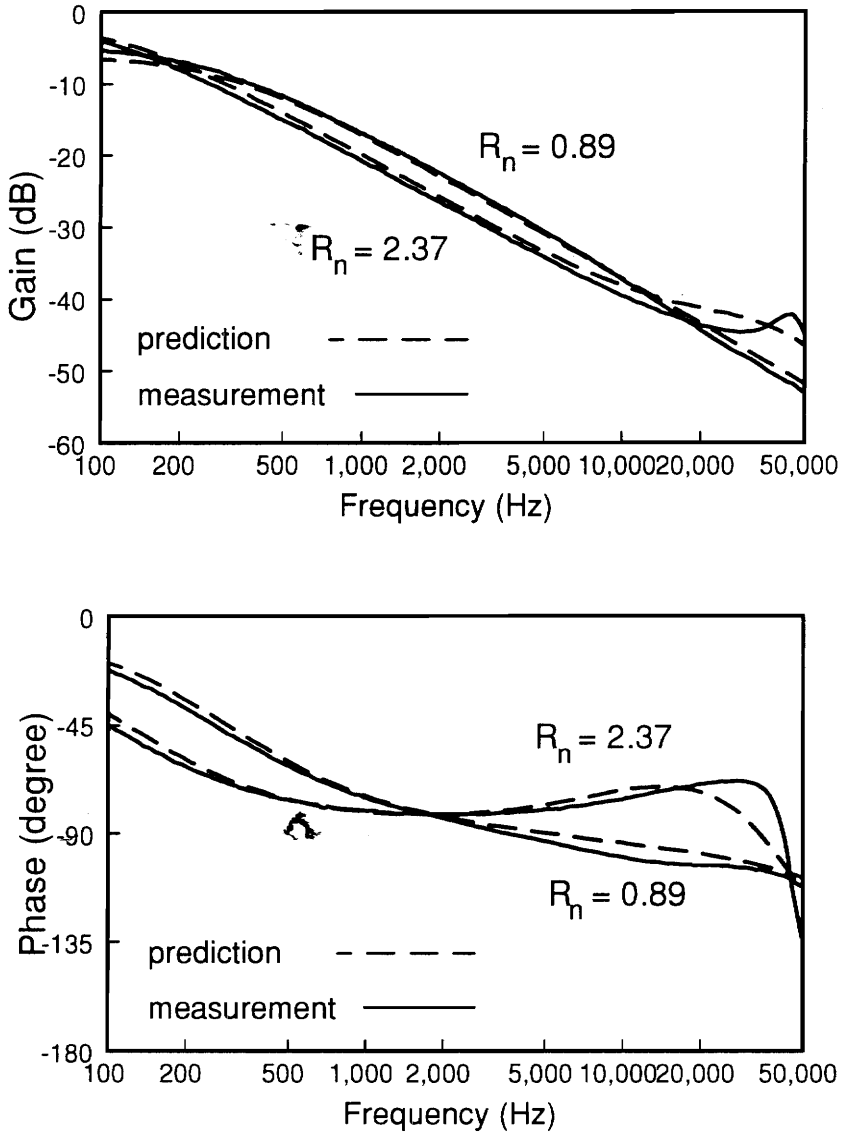

Figure 3.15. Measurement and prediction of the control-to-output voltage gain: *The switching frequency of the experiment circuit is 90 kHz.*

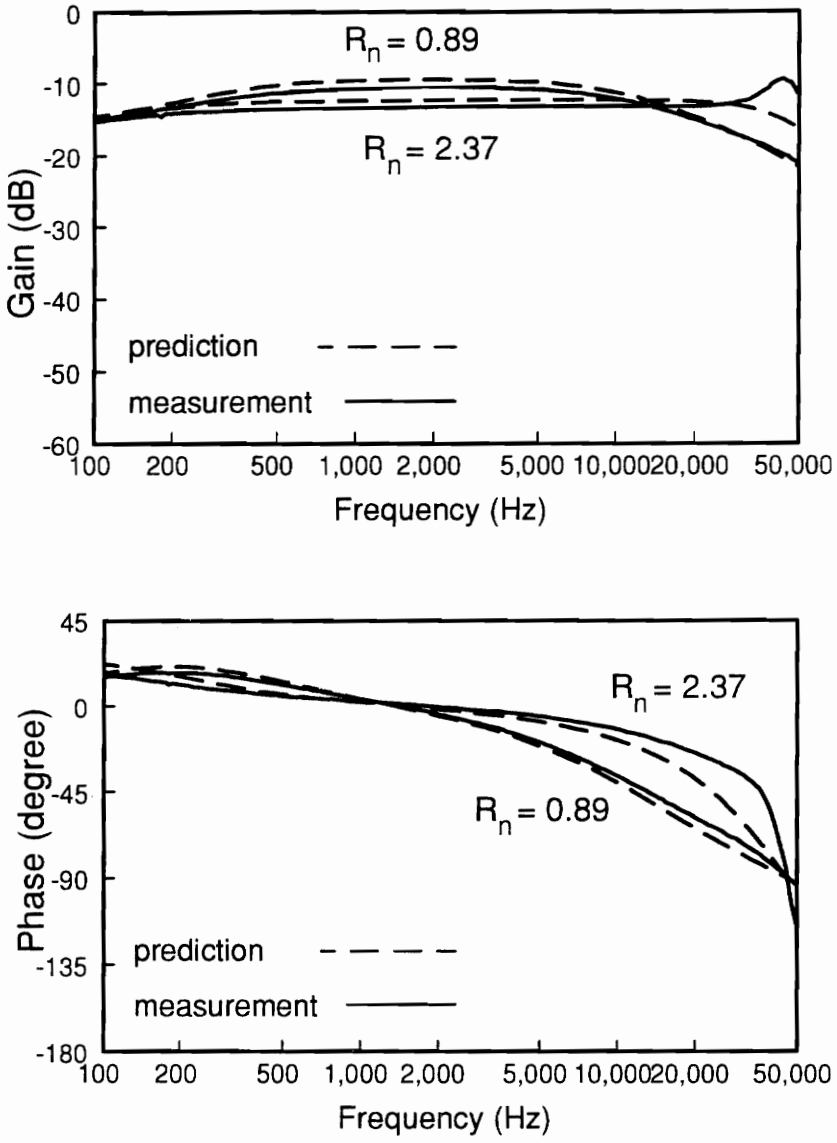

Figure 3.16. Measurement and prediction of the control-to-inductor current gain: *The switching frequency of the experiment circuit is 90 kHz.*

3.8 Summary

Charge control is a special type of current-mode control. It uses the integration of the on-time inductor current as the feedback control signal. The main feature of charge control is its ability to control the average switch current of a PWM converter. Due to this property, it can be applied to power factor correction circuit control when buck or flyback converter is used as the power stage. Charge control also solves the switching noise problem which exists in PCM control.

Unlike PCM and ACM controls, the current loop stability of charge control is both line- and load-dependent. The current loop has smaller phase margin when the converter operates in the light load. The control-to-output voltage transfer function of charge control also has single low-frequency pole characteristic which is common to all current-mode controls, but its low-frequency characteristic is both line- and load-dependent, which makes the voltage feedback loop optimum design more difficult.

Other applications of charge control can also be found. For certain converter topologies, such as multi-resonant-converters (MRC), the active switch does not turn off at the time when its switching current reaches its maximum value. Hence, the PCM control cannot be used to control these converters, while it is

possible to apply charge control to these converters, since the charge of the switching current always increases with time.

In this chapter, a complete small-signal model is developed for PWM converter with charge control. The relationship between current loop instability and converter operation conditions is found for the first time. The developed small-signal model is confirmed by both the time-domain simulation and the experiment. Based on the small-signal analysis, design guidelines for charge control are proposed which ensure the stability of the system under given line and load ranges. The application of charge control in flyback PFC will be detailed in Chapter IV.

4. AVERAGE CURRENT-MODE AND CHARGE CONTROLS FOR PFC APPLICATIONS

4.1 Introduction

Due to the ever-increasing requirements for improved power quality, the demand for the use of power factor correction (PFC) for switching ac-dc power supplies have dramatically increased. A variety of circuit topologies and control methods have been employed for the PFC application. Among them, boost and flyback converters are two frequently used topologies, since both converters have voltage step-up capability.

The circuit diagrams of both boost and flyback PFCs are shown in Fig. 4.1. The boost PFC can handle large output power. The input current of the boost PFC is continuous, and it has less switching harmonics compared to flyback topology. The limitations of boost PFC are: 1) no isolation; 2) start-up and short circuit problems; 3) high output voltage. For low power applications, flyback converter is more attractive than boost converter because of its simplicity. It solves the isolation, start-up, and short circuit protection problems by a single switch. Also, the line voltage is not necessarily lower than the output voltage, as in the boost converter case. The main limitation of flyback PFC is output power level. Another limitation of flyback PFC is its pulsating input current, which results in a large EMI filter.

Both ACM and PCM controls have been used to control boost PFC circuit. PCM control is easier to implement comparing to ACM control, but it introduces line current distortion to boost PFC circuit [33, 34, 36, 37]. ACM control is also applied to CCM flyback PFC system [8,26]. But due to the pulsating nature of the switch current, the current loop stability is difficult to maintain without sacrificing current loop bandwidth [8]. Low bandwidth in current loop results in a large distortion in line current [27]. Charge control controls the per cycle switch current charge of a PWM converter. This charge is proportional to the average switch current if the switching frequency is constant. Hence, charge control is a good candidate for flyback PFC control.

When current-mode controls are applied to PFC circuit, the current loop stability is difficult to maintain, since the line voltage of the PFC circuit varies from zero to its peak amplitude. The subharmonic oscillation in a PFC system introduces subharmonic contents into line current spectrum, which may affect the input EMI filter design. In the other hand, overcompensating subharmonic oscillation results in small current loop bandwidth and large line current distortion.

In this chapter, issues related to applications of ACM and charge controls to PFC circuits are studied. Different current-mode controls are compared each other for both boost and flyback PFC applications in Sec. 4.2. To justify the application of charge control to CCM flyback PFC, the efficiencies of CCM and DCM flyback PFCs are compared in Sec. 4.3. Subharmonic oscillation in PFC system and its effect on EMI filter design are addressed in Sec. 4.4, with CCM flyback PFC as an example. Section 4.5 discusses how to eliminate subharmonic oscillation while keeping line current distortion within specification.

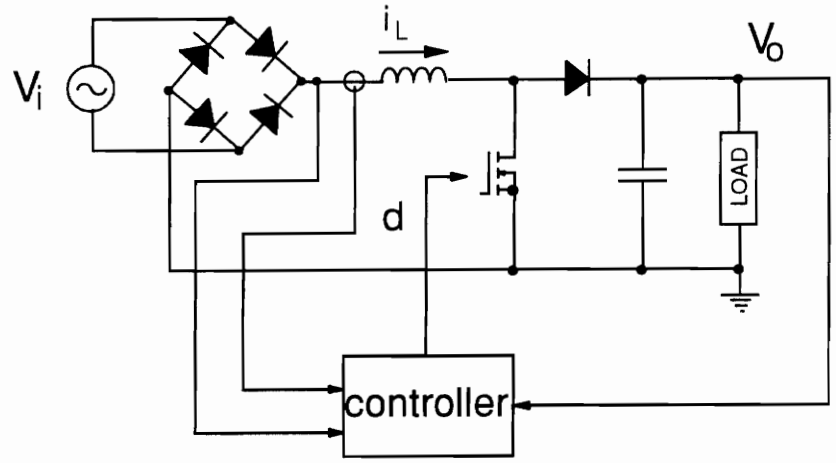

(a) boost PFC circuit diagram

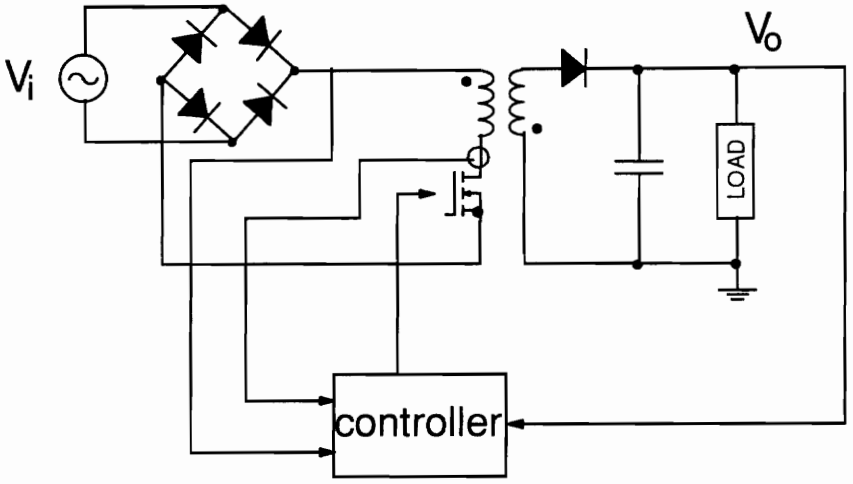

(b) flyback PFC circuit diagram

Figure 4.1. Circuit diagrams of the boost and flyback PFC circuits: *The input current of a boost converter is the inductor current which has less switching harmonics. The flyback topology provides isolation and voltage step up and down capability; it also has no current inrush problem.*

4.2 Comparison of Current-Mode Controls in PFC Applications

One important application of current-mode control is to control a PWM converter as an active PFC circuit. The block diagram of a PFC system with current-mode control is shown in Fig. 4.2. The rectified line voltage, $v_{in}(t)$, is scaled down and multiplied by the error voltage, v_e, to form a control reference, $v_c(t)$. The input current is sensed and processed in a way so that its average value can accurately follow the reference. Since the significant harmonics of $v_c(t)$ is up to its 8th harmonic (the 8th harmonic is only 0.5% of its peak value [27]), to accurately construct the average input current according to $v_c(t)$, the control voltage-to-average input current gain must be flat from dc up to 1 kHz.

In this section, the current-mode controls are compared for both boost and flyback PFC applications. The emaphasis is put on the flyback PFC, since charge control is applied to CCM flyback PFC for the first time.

4.2.1 Boost PFC Control

Both PCM and ACM controls have been used for boost PFC control. The PCM control only controls the peak inductor current of a PWM converter. There

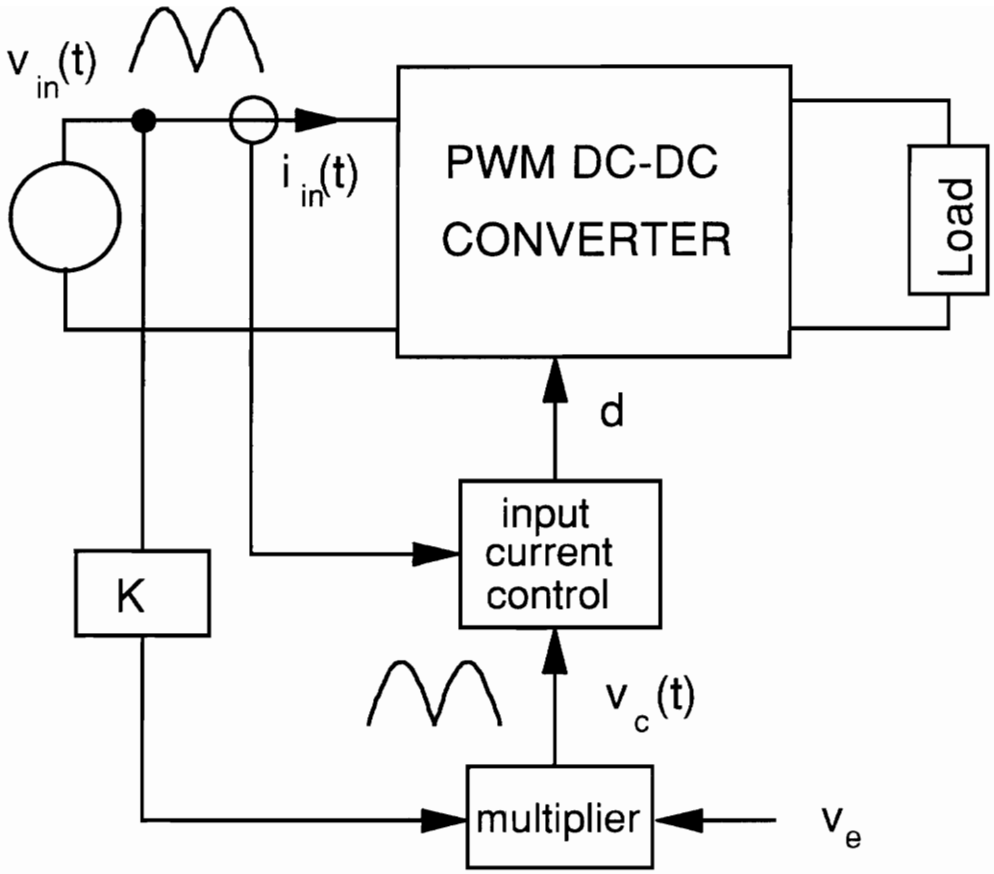

Figure 4.2. The circuit diagram of a PFC system with current-mode control: *The rectified line voltage, $v_{in}(t)$ is scaled down and multiplied by the error voltage, v_e, to form a control reference, $v_c(t)$. The input current of the PFC circuit is sensed and processed in a way so that its average value follows the control reference.*

exists difference between peak and average inductor currents of a PWM converter, especially when it operates in DCM. In PFC application, the DCM operation cannot be avoided, since the input current of the PFC circuit is very small near the line voltage zero-crossing. On the other hand, the duty cycle of a boost PFC circuit varies from its maximum value (usually 95%) to its minimum value, as the line voltage changes from zero to its peak amplitude. Hence, when PCM control is used, the current loop instability cannot be avoided if no external ramp is added. Adding an external ramp in PCM control introduces line current distortion, and design trade-offs have to be made when PCM control is used [33]. The more detail comparison between PCM and ACM controls in boost PFC applications can be found in [33, 34, 36, 37].

4.2.2 Flyback PFC Control

The ACM control scheme is used to control average switch current in [8]. The control scheme is shown in Fig. 4.3, where the switch current is sensed and averaged by the current compensator. The control scheme is called average switch current-mode (ASCM) control here since it is the switch current that is averaged by the current compensator. Unlike the inductor current, the switch current has a pulsating nature, which causes a large ac ripple at the current compensator output. The main problem of using ASCM control is its current

loop crossover frequency is limited by the zero in converter power stage duty cycle-to-switch current gain [26], which results an varying control-to-switch current gain over the interested frequency range. The other problem of using ASCM control is the low bandwidth in the current feedback loop, due to the pulsating feature of the switch current.

The control-to-switch current gain can be used to study the line current distortion of a flyback PFC circuit. The low-frequency control-to-switch current gain of a 500 W flyback PFC with both charge and ASCM controls are shown in Fig. 4.4 (a) and (b), respectively. The gains corresponding to charge control case are almost flat in the interesting frequency range, which means no current distortion is introduced in charge controlled flyback PFC. The control-to-switch current gain of ASCM controlled flyback PFC changes at higher frequency, which means high frequency distortion will be introduced into line current.

To estimate the line current distortion caused by the uneven gain, time-domain simulation is performed. To approximate the line current distortion, the rectified line voltage, shown in Fig. 4.5 (a) as the solid line, is applied to a system which possesses a gain as Fig. 4.4 (b) (in the simulation, the transfer function corresponding to D = 0.66 is used). The normalized system output which is the average input current of the flyback PFC circuit, is shown in Fig. 4.5 (a) with dotted line. The corresponding line current and its Fourier analysis results are shown in Fig. 4.5 (b) and (c), respectively. Fig. 4.5 (c) can

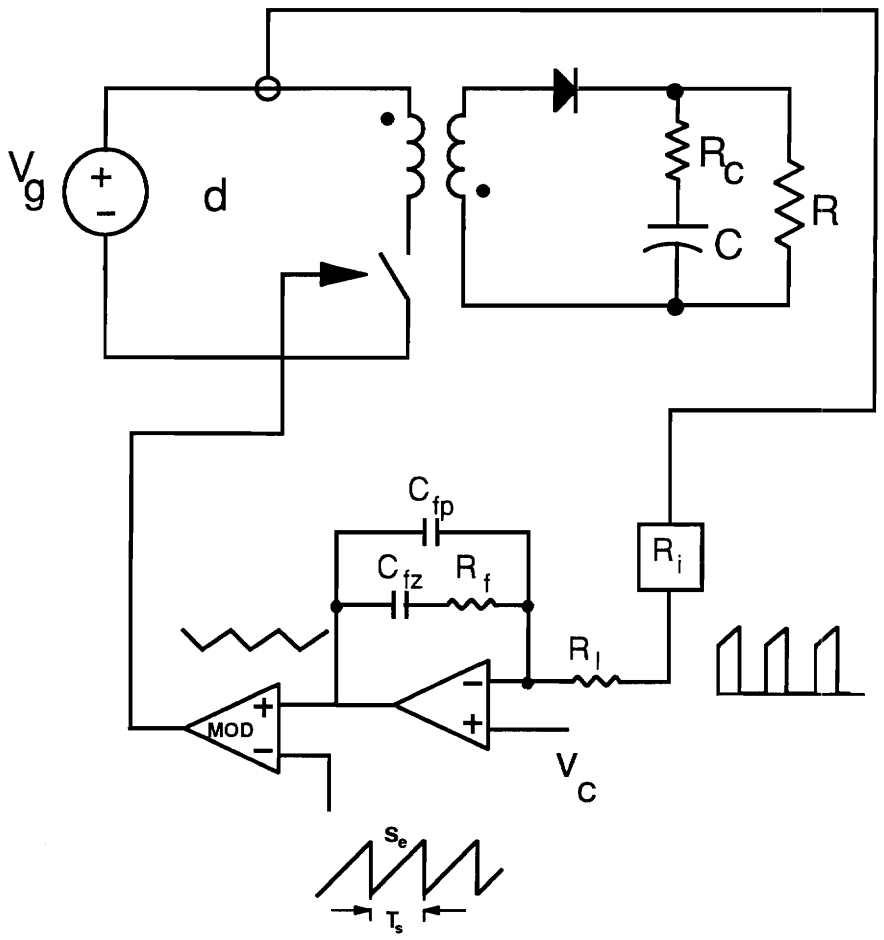

Figure 4.3. Circuit diagram of average switch current-mode (ASCM) control.: *The switch current is sensed and feed into the current compensator. The output of the current compensator is much more pulsating than at ACM control case.*

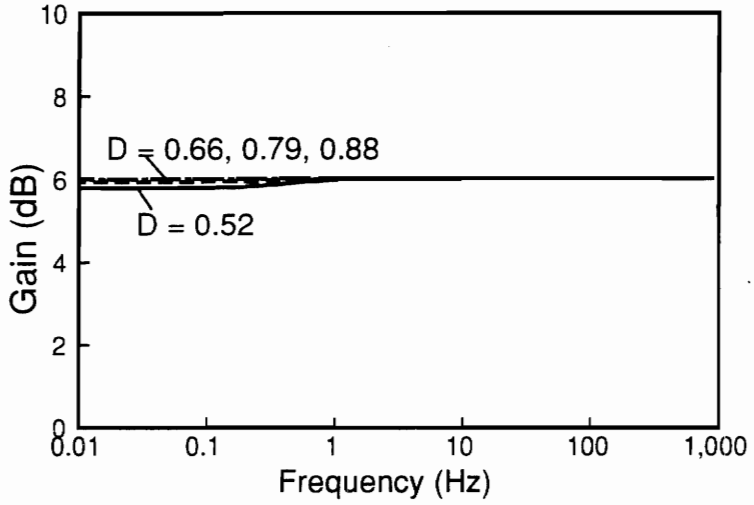

(a) charge control

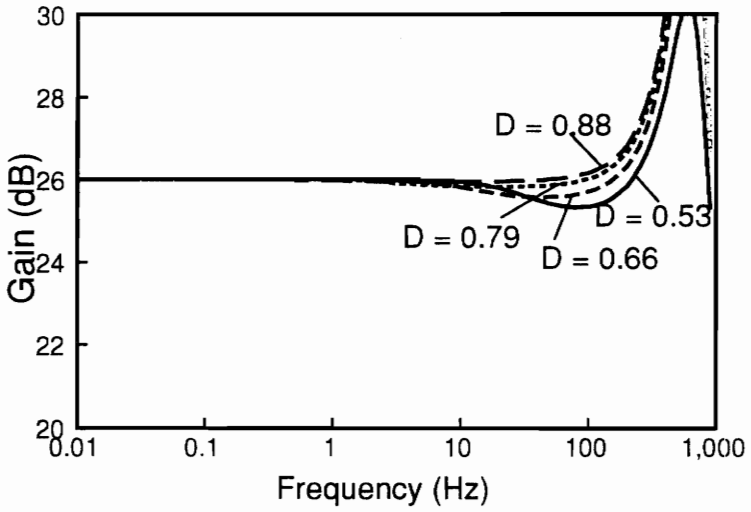

(b) ASCM control

Figure 4.4. The control-to-switch current gains of flyback PFC with ASCM and charge controls.: *The characteristics corresponding to charge control are flat in the interested frequency range, which insures average switch current follows the control voltage exactly. The characteristics corresponding to ASCM control are uneven at higher frequency, which means high frequency distortion will be introduced to the line current When ASCM control is used.*

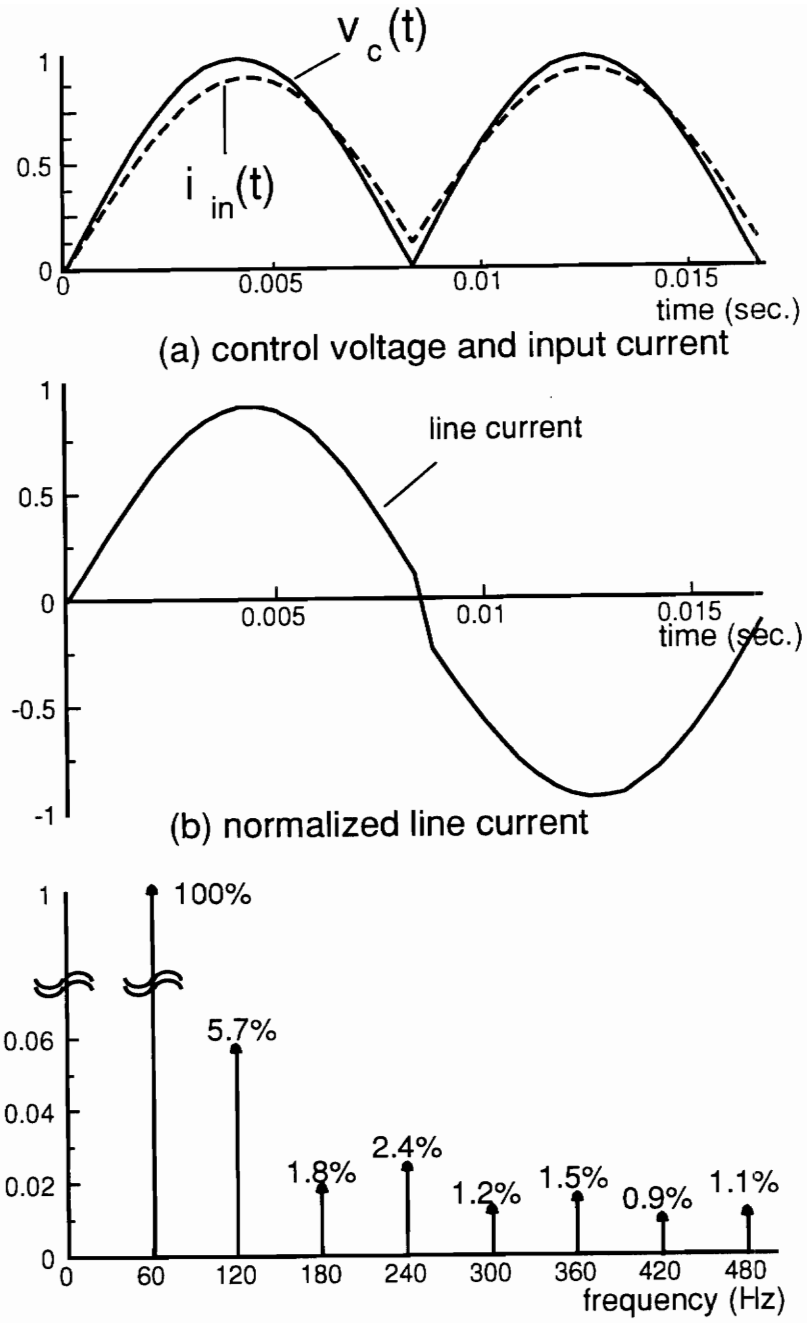

Figure 4.5. Simulation results of ASCM controlled flyback PFC: *The control reference and the normalized input current of the flyback PFC are shown in (a), and the current is distorted from the control; The line current and its spectrum are shown in (b) and (c), respectively.*

be used to estimate the line current distortion. For the 500 W flyback PFC, if the efficiency of the PFC circuit is assumed 85%, the input rms current is 6.5 A, then the second harmonic of the line current is 0.37 A, which is large than the allowed second harmonic distortion given in IEC555-2 specification.

Since the control-to-switch current gain of charge control is flat up to half of the switching and is independent of converter operation conditions, no distortion will be introduced to the line current of a flyback PFC if charge control is used.

4.3 Loss Comparison of CCM and DCM Flyback PFC

Due to its simplicity and low cost, flyback PFCs are more attractive for many applications. Both CCM and DCM operation flyback converters can be used as PFC circuits. When a flyback converter is operating in DCM, the converter automatically achieves unity power factor if the switch on-time is kept constant during one line cycle [28]. The control scheme for a DCM flyback PFC is very simple. No current loop is needed, and the duty cycle is kept constant during each cycle to maintain a unity power factor. The main drawback of DCM operation is the large instantaneous and rms input current, which results in large current stress and large switching and conduction losses.

As has been mentioned before, charge control can be used to control CCM flyback converter as PFC circuit. Compared to constant duty cycle control, charge control scheme is more complicated. It needs to sense the switch current as well as to form a line reference. The application of charge control to CCM flyback PFC is justified by comparing the efficiency of CCM flyback PFC with that of DCM flyback PFC. The losses considered in the comparison are the conduction and switching losses of the switch and the output rectifier, as well as the core and copper losses of the energy storage transformer. The detailed derivations for these losses are listed in Appendix C. The switch losses for both MOSFET and IGBT are calculated for the purpose of comparison. When the loss is a function of line voltage, it needs to be averaged in half a line cycle.

The comparison is carried out for a 300 W flyback PFC with 48 V output voltage. The line range is 85 V to 265 V. Both CCM and DCM flyback PFC designs are optimized. The efficiency versus output power characteristics are shown in Fig. 4.6, where the superscript denotes the mode of operation, and the subscript denotes which device is used for the switch (M for MOSFET, I for IGBT). It can be seen that whether MOSFET or IGBT is used, the efficiency of CCM operation is at least 3 percent higher than that of DCM operation. For DCM operation, if MOSFET is used as the switch, the conduction loss of the device is very large because of the large input rms current, and if IGBT is used as the switch, the switching loss of the device is very large due to the large peak input current. It can also be seen that MOSFET is more efficient for lower

power application, while IGBT is more efficient for higher power application. This is due to the dramatical increase in MOSFET conduction loss as the output power increases [29].

4.4 Effect of Subharmonic Oscillation in PFC Circuits

Subharmonic oscillation is a common property in all kinds of current-mode control. For a dc-dc converter, this oscillation is always avoided, even though it is bound by the controller and the non-linearity of the system. There are two main reasons that the subharmonic oscillation in dc-dc converters is unacceptable. The first one is that it introduces subharmonic frequency contents into the system. The ripple caused by subharmonic oscillation will be seen by the source and the load of the converter, since the input and output filters are designed to attenuate only the switching ripple. The second reason is that the oscillation may saturate the core of the isolation transformer, because during subharmonic oscillation, the duty cycle is much larger than that of the normal operation.

For a PFC circuit with current-mode control, the subharmonic oscillation is unavoidable since the rectified line voltage can be as small as zero. Hence, it is necessary to study the effects of this oscillation on the PFC circuit

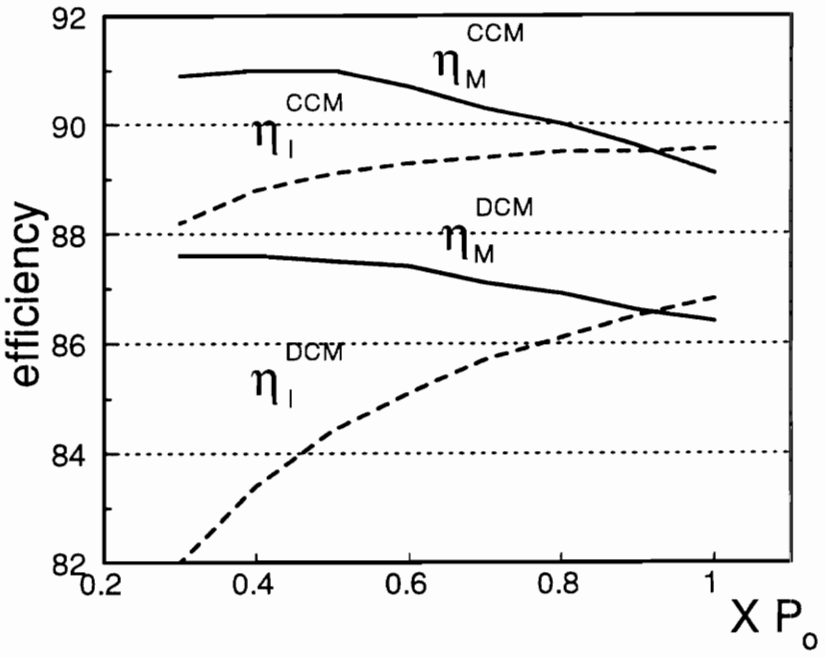

Figure 4.6. Efficiency of CCM and DCM flyback PFCs as a function of the output power: *The superscript denotes the mode of operation. The subscript denotes which device is used as the switch. No matter what device is used, the efficiency of CCM operation is much higher than that of DCM operation, which justifies the preference for CCM flyback PFC.*

performance. The isolation transformer of a PCM controlled boost PFC can hardly be saturated since subharmonic oscillation occurs only at low line voltage. Because the bulk capacitor exists at the output of the PFC circuit, the ripple voltage caused by subharmonic oscillation will not be seen by the load. However, subharmonic oscillation will introduce a subharmonic component into the input current spectrum and may affect the input EMI filter design. To study the effect of subharmonic oscillation on the input filter design, the flyback PFC with charge control is used as an example. A 300 W CCM flyback PFC with charge control is simulated to obtain its input current spectrum. The input current spectra at low line (worst case) and different load are shown in Fig. 4.7. The switching frequency of the circuit is 70 kHz. Several observations can be made from Fig. 4.7. First, the spectrum corresponding to subharmonic oscillation is smaller than that at the switching frequency because subharmonic oscillation only exists in a small region over a line cycle. Second, the subharmonic oscillation in charge control is load dependent. The subharmonic oscillation at half load is more severe than that at full load, since subharmonic oscillation in charge control occurs at light load. When the load is very light, the converter operates in DCM during most of the line cycle, which does not contain subharmonic oscillation.

To examine whether subharmonic oscillation will adversely affect the input filter design, a two-stage filter, shown in Fig. 4.8, is designed for the 300 W flyback PFC. The largest spectra at half and the switching frequency are shown in Fig. 4.9. The VDE 0871 EMI specification of the interested frequencies and

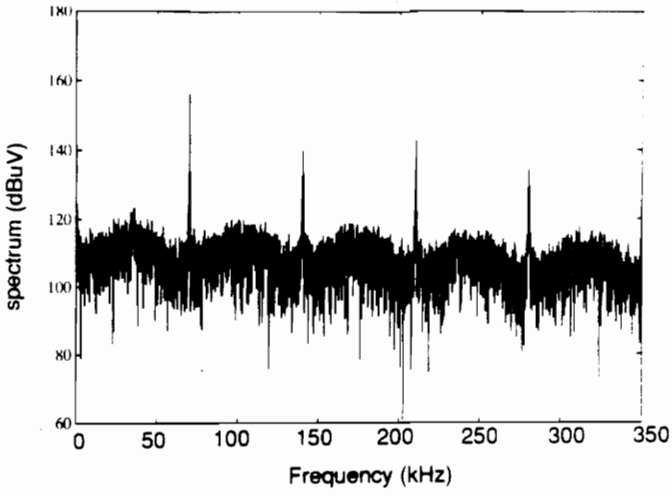

(a) low line and full load

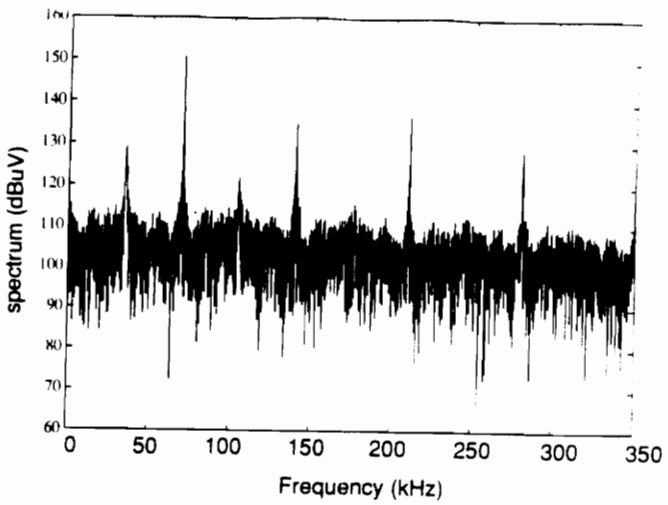

(b) low line and half load

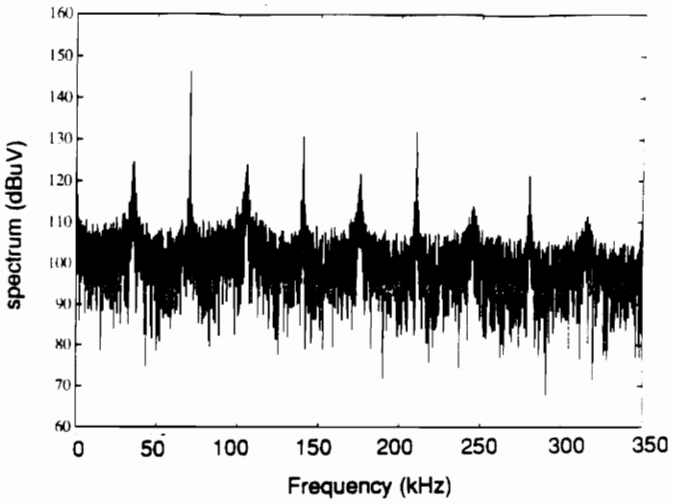

(c) low line and 30% load

Figure 4.7. Input current spectrum of a 300 W CCM flyback PFC with charge control: *The switching frequency is 70 kHz. The maximum switching frequency spectrum appears at low line and full load operation. The low line and half load operation gives the maximum subharmonic spectrum.*

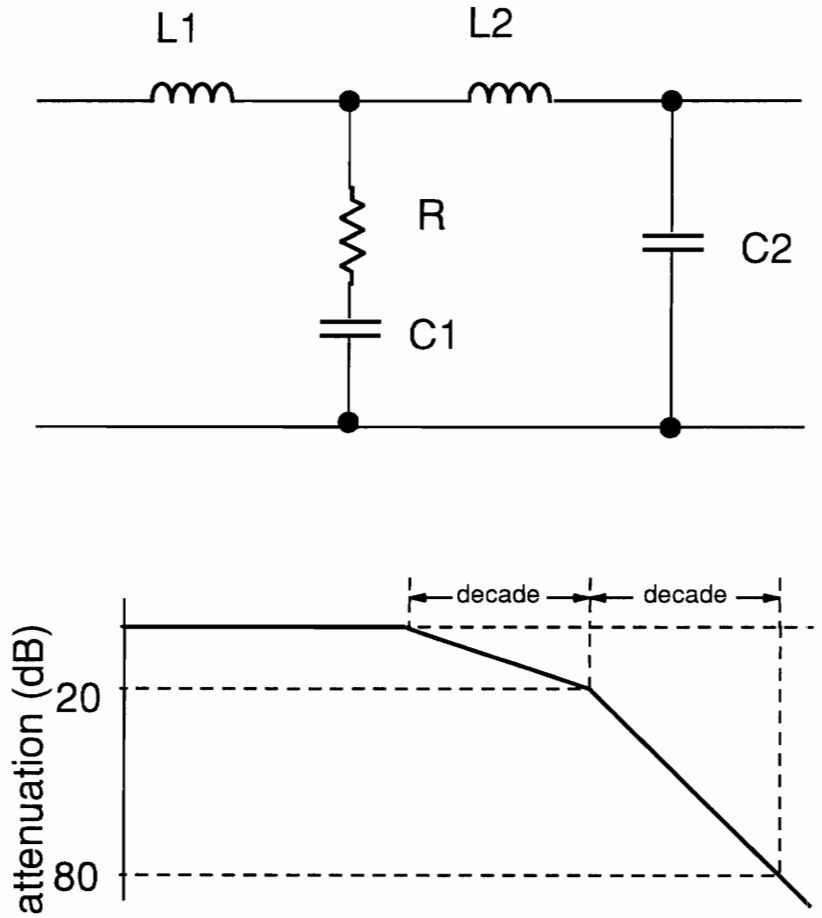

Figure 4.8. Two-stage input filter and its characteristic:

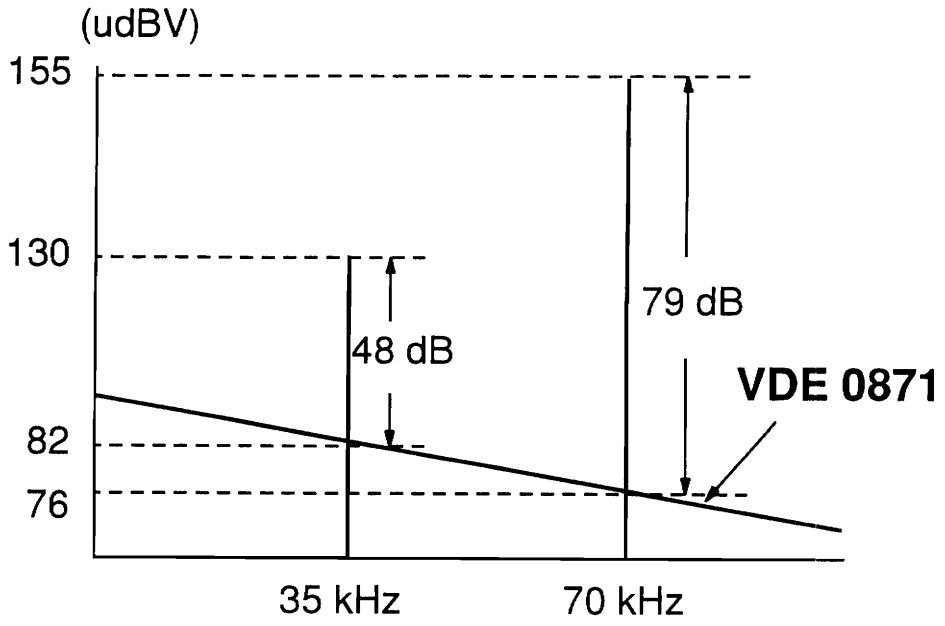

Figure 4.9. Worst case input current spectra of 300 W CCM flyback PFC: *The worst case spectra at half and the switching frequency are much higher than the given EMI specification. To meet the EMI specification, 48 dB attenuation is needed at 35 kHz, and 79 dB attenuation is needed at 70 kHz.*

the required attenuation of the filter to meet the EMI specification are also shown in Fig. 4.9. The filter is designed to have 80 dB attenuation at 70 kHz. The design results are as follows:

$$L1 = 6.4\,mH, \quad L2 = 0.64\,mH$$

$$C1 = 8\,\mu F, \quad C2 = 0.8\,\mu F, \quad R = 40$$

The designed filter gives 62 dB attenuation at 35 kHz, which is more than necessary to attenuate the spectrum caused by subharmonic oscillation. So, for the 300 W flyback PFC, subharmonic oscillation has no effect on the size of the two-stages input filter. For input filter which has steep attenuation characteristic [30], the subharmonic oscillation will affect the filter design.

To increase the output power lever of flyback PFC, interleaving technique can be applied. Interleaving more than one power stages also increases the input current ripple frequency and reduces the magnitude of the ripple current, which results in a smaller input EMI filter. The simulation results of the input current spectra of a 600 W interleaved (two 300 W modules) CCM flyback PFC are shown in Fig. 4.10. It can be seen from Fig. 4.10 that the switching frequency (70 kHz) harmonic is totally cancelled. At low line, the ripple frequency (140 kHz) spectra are smaller than those at high line. This is because at low line the duty cycle is larger than fifty percent, and the input currents of each module overlap, which greatly reduces the magnitude of the

ripple current. The subharmonic oscillation occurs at low line and light load, as shown in Fig. 4.10. The worst case spectra at different frequencies are shown in Fig. 4.11. The EMI specification and the required attenuation of the filter are also shown in Fig. 4.11. The two-stage filter shown in Fig. 4.8 is designed to meet the required attenuation. The first design only considers the harmonic component at ripple frequency. It can be seen from Fig. 4.11 that 80 dB attenuation is needed at 140 kHz. The designed filter's characteristic is shown in Fig. 4.8(a). The design results are as follows:

$$L1 = 1.6\,mH, \quad L2 = 0.16\,mH$$

$$C1 = 8\,\mu F, \quad C2 = 0.8\,\mu F, \quad R = 15$$

It can be seen from Fig. 4.12(a) that the design only has 43 dB attenuation at 35 kHz, which does not meet the requirements given by Fig. 4.11. To satisfy all the requirement, a second design is performed, which gives 55 dB attenuation at 35 kHz. The designed filter's characteristic is shown in Fig. 4.12(b), and the design results are as follows:

$$L1 = 3.9\,mH, \quad L2 = 0.39\,mH$$

$$C1 = 8\,\mu F, \quad C2 = 0.8\,\mu F, \quad R = 22.4$$

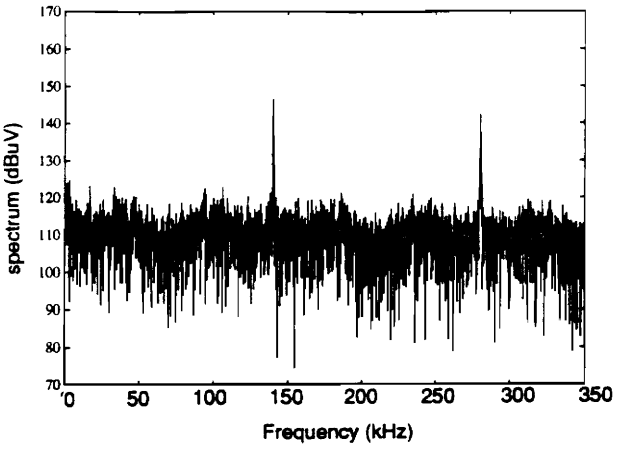

(a) low line and full load

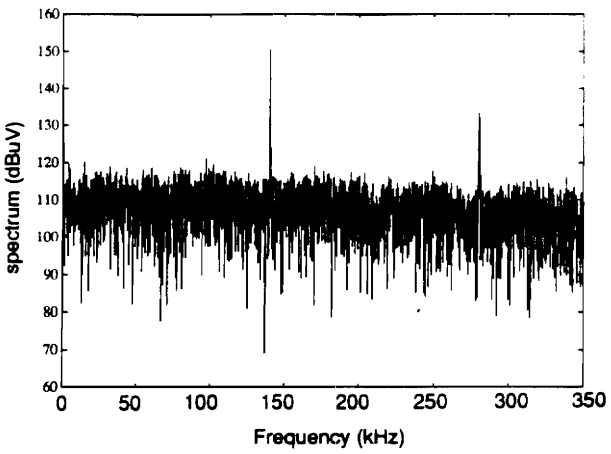

(c) high line and full load

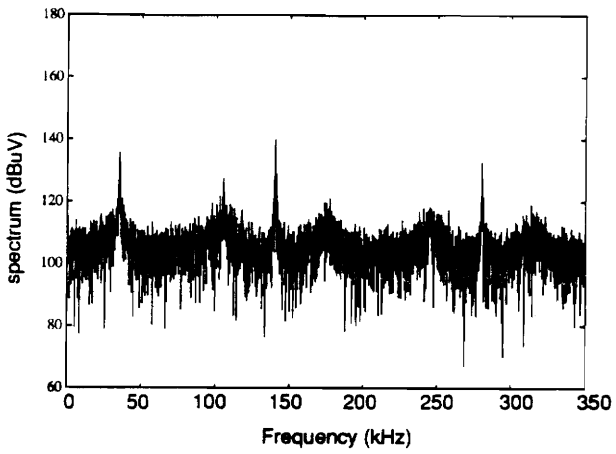

(b) low line and half load

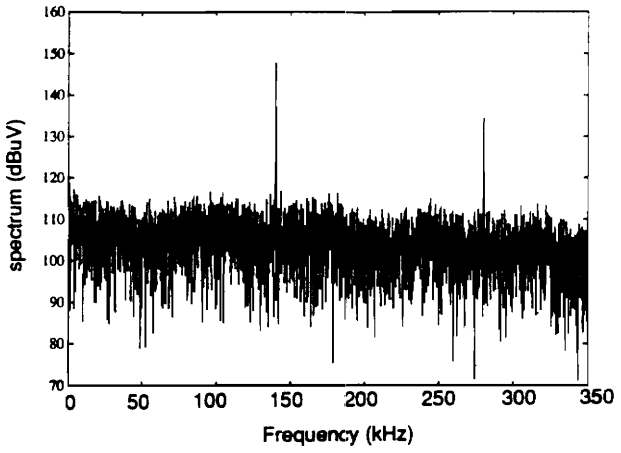

(d) high line and half load

Figure 4.10. Input current spectrum of a 600 W interleaved CCM flyback PFC: *The spectrum at switching frequency (70 kHz) is totally cancelled. The maximum ripple frequency (140 kHz) spectrum occurs at high line and full load. The subharmonic oscillation is severe at low line and half load.*

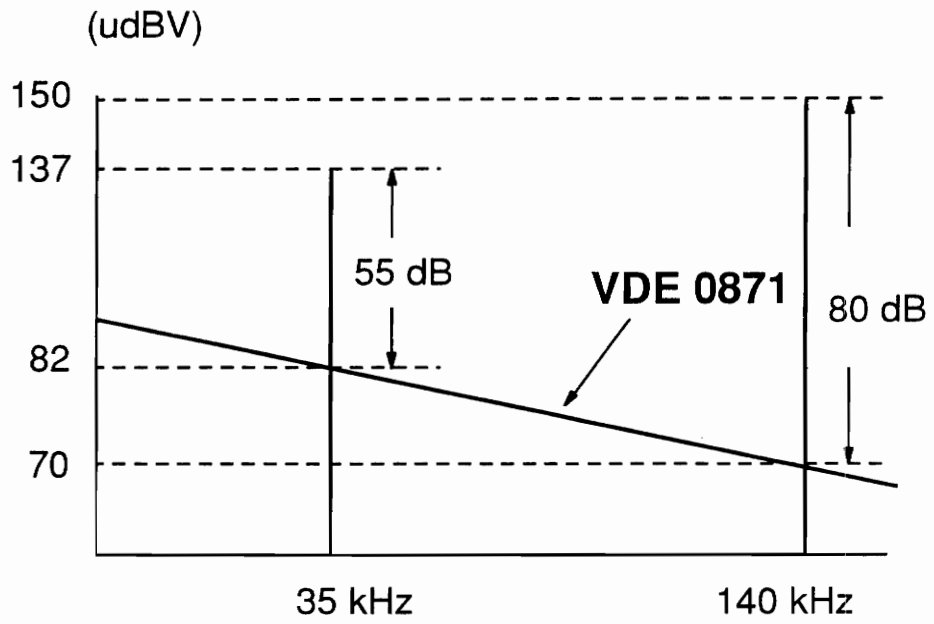

Figure 4.11. Worst case input current spectra of 600 W interleaved CCM flyback PFC: *The spectra at half the switching frequency and the ripple frequency are much higher than the EMI specification. To meet the EMI specification, 55 dB attenuation is needed at 35 kHz. 80 dB attenuation is needed at 140 kHz.*

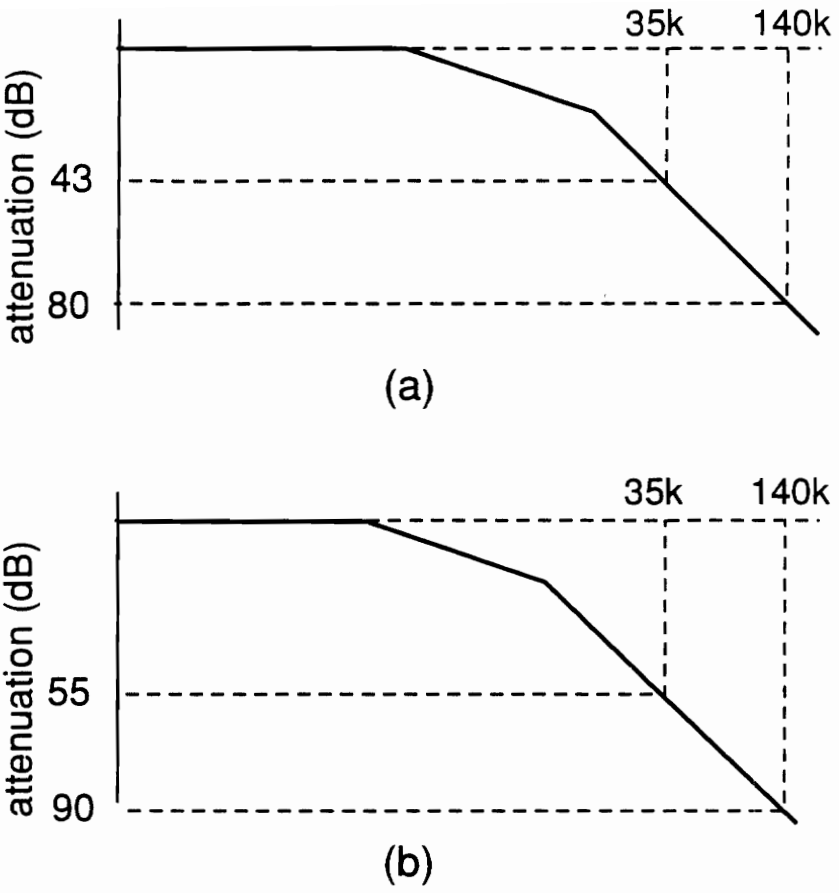

Figure 4.12. Two-stage filter design results: *The first design only gives 43 dB attenuation at 35 kHz, which does not meet the requirement given in Fig. 4.11. The second design satisfies all the requirements given in Fig. 4.11.*

The second design meets the required attenuation at all frequencies. But the size of it is at least two times larger than the first design. By comparing the input filter sizes of the 300 W non-interleaved and the 600 W interleaved flyback PFCs, one can conclude that the interleaving technique greatly reduces the size of the input filter. It is also found that the EMI filter size of an interleaved flyback PFC can be greatly reduced if subharmonic oscillation is eliminated.

4.5 Eliminate Subharmonic Oscillation for ACM and Charge Controls

Subharmonic oscillation is caused by the current loop instability. To investigate subharmonic oscillation, the current loop small-signal characteristic needs to be analyzed. The current loop gain of a PWM dc-dc converter with ACM or charge control has the following general form:

$$T_i(s) \simeq F_m R_i G_i(s) G_{id}(s) H_e(s), \tag{4.1}$$

where F_m, R_i, and $H_e(s)$ are modulator gain, current gain, and sampling gain, respectively. $G_{id}(s)$ is the power stage duty cycle-to-inductor current transfer

function. $G_i(s)$ is the effective current loop compensator gain for ACM control, and it does not exist in charge control.

For PFC circuit, the input voltage is ac voltage, which varies from zero to its peak value during each line cycle. Since the switching frequency is much higher than the line frequency, the line voltage can be assumed constant within each switching cycle. This assumption is called quasi-static approach [31]. Under this assumption, F_m, R_i, and $G_{id}(s)$ are functions of the line voltage.

The current loop instability occurs at high-frequency. After power stage resonant frequency, the duty cycle-to-inductor current gain, $G_{id}(s)$, for all PWM converters has the following approximation:

$$G_{id}(s) \simeq \frac{V_{ap}}{Ls}, \tag{4.2}$$

Substituting Eq. (4.2) into Eq. (4.1), the high-frequency approximation of the current loop gain is obtained:

$$T_i(s) \simeq \frac{F_m R_i V_{ap} G_i(s)}{L} \frac{1}{s} H_e(s). \tag{4.3}$$

Since $G_i(s)$ can be approximated by a constant at high-frequency, the high-frequency current loop gains of ACM and charge controls have the same shape. It forms by an integration and a pair of right-half-plane zeroes centered at half the switching frequency. Since the phase characteristic is independent

of converter operation conditions and the current loop compensation, the current loop stability margin is determined by the current loop crossover frequency, ω_c, as shown in Fig. 4.13. ω_c has following general forms:

$$\omega_c = \frac{F_m R_i V_{ap} G_i(s)}{L}. \tag{4.4}$$

By substituting corresponding F_m, R_i, $G_i(s)$ of ACM control and V_{ap} of the boost converter into Eq. (4.4), the current loop crossover frequency of ACM control boost PFC is obtained:

$$\omega_c = \frac{F_s}{\omega_z DD'T_s + D'(1 - \frac{\omega_z}{\omega_{hp}})(1 - e^{-\omega_{hp}DT_s}) + \frac{LS_e\omega_z}{V_o\omega_i}}. \tag{4.5}$$

ω_c varies with line voltage, and at line voltage zero crossing, line voltage equals zero, which gives the maximum crossover frequency, ω_c^{max}:

$$\omega_c^{max} = \frac{F_s V_o \omega_i}{S_e \omega_z}. \tag{4.6}$$

Equation (4.6) can be used to design boost PFC current loop compensation. To avoid subharmonic oscillation, for a fixed sawtooth ramp slope, S_e, the integrator gain, ω_i, is selected so as to allow the current loop to cross the zero dB before half the switching frequency. Overcompensating reduces the current loop bandwidth of ACM control, which results in large line current distortion [33].

By substituting corresponding F_m, R_i, $G_i(s)$ of charge control and V_{ap} of the flyback converter into Eq. (4.4), the current loop crossover frequency of charge control flyback PFC is obtained:

$$\omega_c = \frac{V_o}{(I_{Lp} + S_e C_T)L}, \tag{4.7}$$

where I_{Lp} is the peak inductor current, which is a function of the line voltage and load current. Hence, ω_c varies with line and load. At line voltage zero-crossing, the peak inductor current equals zero, which gives maximum crossover frequency:

$$\omega_c^{\max} = \frac{V_o}{S_e C_T L}. \tag{4.8}$$

To avoid subharmonic oscillation, the external ramp is selected so as to allow the current loop to cross zero dB before half the switching frequency.

In charge control, the compensation ramp introduces distortion to the line current, since the average line current is following the control voltage subtracting the voltage drop, $S_e D T_s$. Large compensation ramp slope produces large line current distortion, and the distortion is more severe near the line voltage zero-crossing.

Since large external ramp introduces large current distortion in charge control, there exists a trade-off between current loop stability and line current

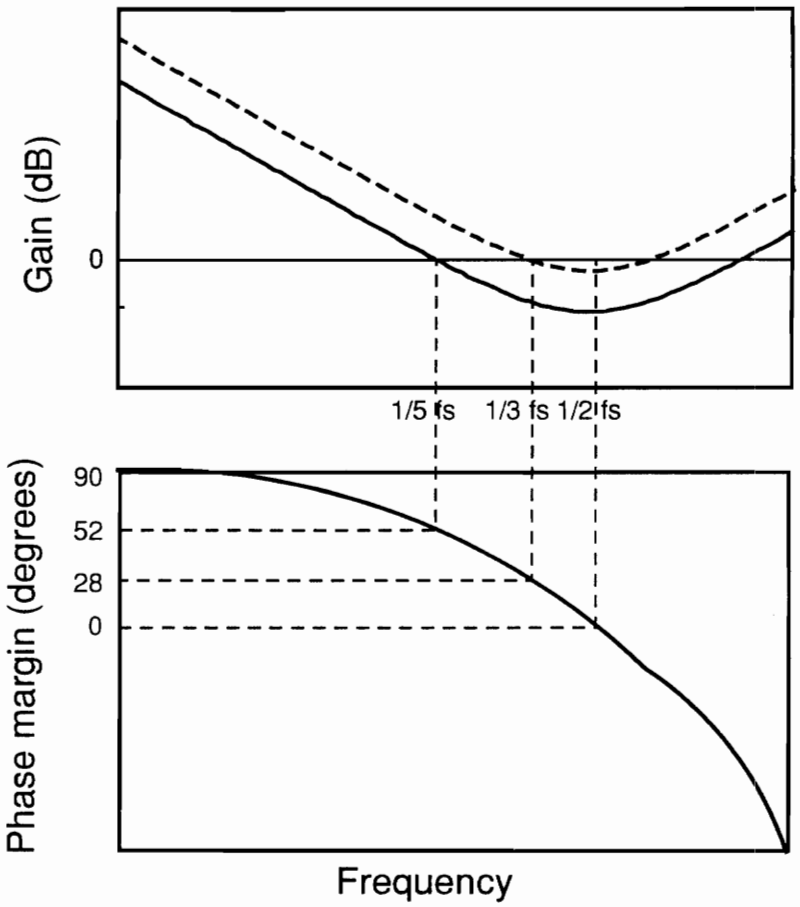

Figure 4.13. Relationship between the current loop crossover frequency and its phase: *The high-frequency phase characteristics are fixed for both ACM and charge controls. Larger crossover frequency gives a smaller phase margin. When the crossover frequency is larger than half the switching frequency, there are no phase and gain margins in the current loop.*

distortion. It can be seen from Fig. 4.13 that the current loop has 52 degrees phase margin if the current loop is closed at one-fifth of the switching frequency. Figure 4.14 shows the simulation results of the 600 W interleaved flyback PFC when the current loop of each module is closed at one fifth of the switching frequency. The high frequency spectrum of the input current at low line and half load (worst case) is shown in Fig. 4.14(a), and the input current low frequency distortion at full load is shown in Fig. 4.14(b). It can be seen from Fig. 4.14 that the subharmonic oscillation is eliminated, but the line current 5th harmonic is too close to the IEC555-2 specification. To reduce the line current distortion, the external ramp slope, S_e, has to be reduced. The current loop crossover frequency is increased from one-fifth to one-third of the switching frequency in order to reduce S_e. The simulation results with a smaller S_e are shown in Fig. 4.15. It can be seen from Fig. 4.15 that the high frequency spectrum remains almost unchanged, since the current loop still possesses a positive phase margin, while the low frequency distortion is greatly reduced due to the decreasing of S_e. So, to eliminate subharmonic oscillation and to keep the line current distortion within specification, the maximum current loop crossover frequency should be between one-third to one-half of the switching frequency.

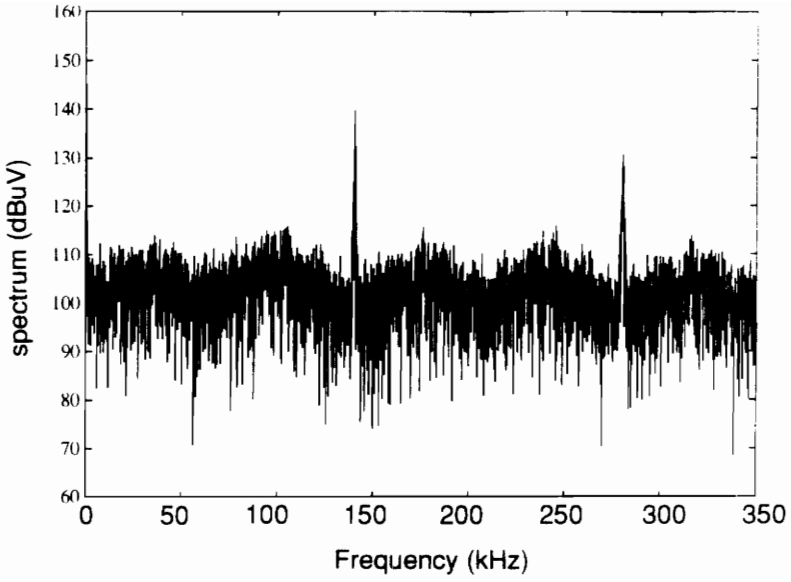

(a) input current spectrum

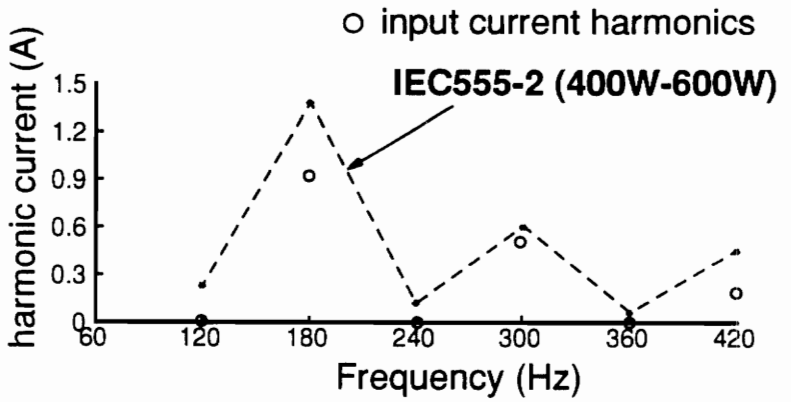

(b) line current distortion

Figure 4.14. Simulation results of 600 W interleaved flyback PFC with large S_e: *The current loop closed at one-fifth of the switching frequency. The line current fifth harmonic is too large. To reduce line current distortion, the external ramp slope S_e, has to be reduced.*

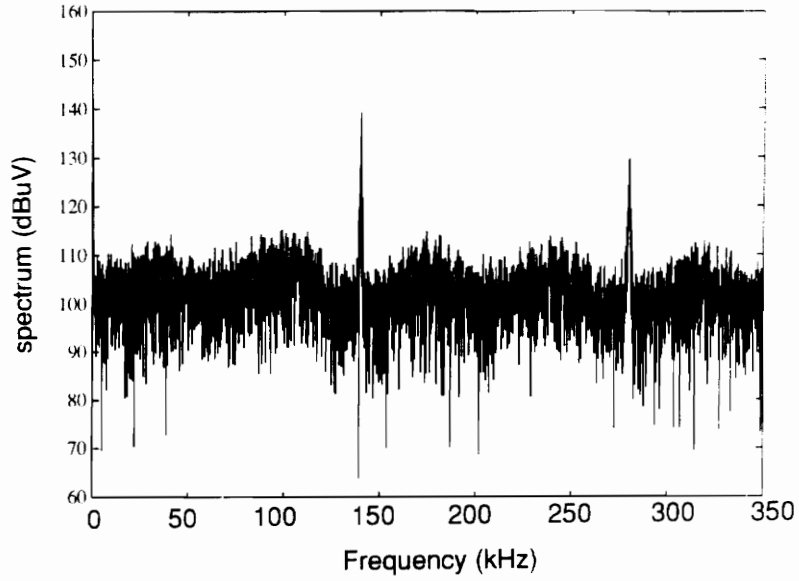

(a) input current spectrum

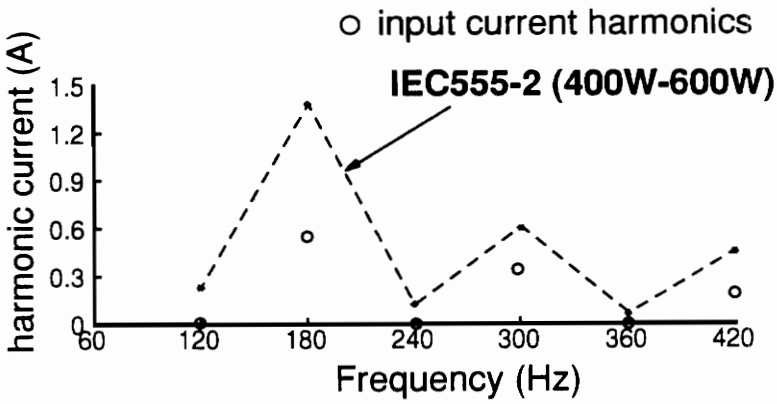

(b) line current distortion

Figure 4.15. Simulation results of 600 W interleaved flyback PFC with small S_e: *To reduce the external ramp slope, the current loop is closed at one-third of the switching frequency. The high frequency spectrum is almost the same as in Fig. 4.14, but the line current distortion is reduced.*

4.6 Summary

In this chapter, The issues related to the application of current-mode control on PFC circuit are studied. It is found that charge control is more suitable for CCM flyback PFC control. The efficiencies of both CCM and DCM flyback PFCs are compared to each other in order to justify the application of charge control to CCM flyback PFCs. It is found through the comparison that the CCM flyback PFC is much more efficient than the DCM flyback PFC.

Subharmonic oscillation will affect the input EMI filter design, if the difference between the subharmonic spectrum and the EMI specification is larger than the attenuation of the filter at that frequency. In such case, a larger filter has to be used.

To eliminate subharmonic oscillation from boost and flyback PFC systems, the small-signal models, developed for dc-dc converter with ACM and charge controls, are used based on quasi-static assumption. The current loop design equations for both boost PFC with ACM control and flyback PFC with charge control are provided. For boost PFC, the current loop stability margin can be increased by reducing the integrator gain of the current compensator, or increasing the external ramp slope. For flyback PFC, the current loop stability can be ensured by properly selecting an external ramp.

For both boost and flyback PFC systems, overcompensating current loop results in a large line current distortion. To satisfy both EMI and line current distortion specifications, the current loop maximum crossover frequency should be around one-third of the switching frequency.

5. CONCLUSION

A complete study on average current-mode and charge controls is conducted in this dissertation. The small-signal models of PWM converters with ACM and charge controls are derived. The derived models are accurate up to half the switching frequency. The models are easy to use, since they are in the continuous-time forms. The sampled-and-hold effect in the current feedback loop is included in the modeling process for both controls; hence, the current loop stability can be accurately predicted by the models. The derived models are verified by experiments and time-domain simulations.

The relationships between current loop stability and converter operation conditions for both controls are found for the first time. For ACM control, the current loop stability is line-dependent. Unlike PCM control, the current loop

has a smaller stability margin for both large and small duty cycles. Based on the small-signal analysis, the current loop optimum design procedures for ACM control are established. The current loop stability of charge control is both line- and load-dependent. The current loop has less stability margin when it operates at light load. Like peak current-mode control, the current loop instability of charge control can be compensated by an external ramp.

The small-signal characteristics of both ACM and charge controls are studied and compared with those of PCM control. All three controls have only a single low-frequency pole in their control-to-output gains, which makes voltage loop optimum compensation easier. The current loop gains of the three current-mode controls have the same shape at high frequency, which indicate that all current-mode controls can develop current loop instability if the current loops are not properly designed. The control-to-inductor current gain of ACM control, as well as the control-to-switch current gain of charge control are flat up to half the switching frequency, which indicate these two controls' ability to control average inductor and switch currents, respectively.

One important application of ACM and charge controls is to control PWM converters as PFC circuits. ACM, PCM and charge controls are compared for both boost and flyback PFC applications. It is concluded that ACM control is more suitable for boost PFC application, while charge control is most suitable for flyback PFC. The flyback PFCs are more suitable for low power applications, since its implementation is much simpler compared to boost PFC.

The CCM flyback PFC is much more efficient compared to the DCM flyback PFC. The current loop instability of a PFC circuit and its effect on the input EMI filter design are studied. Current loop instability should be avoided if the subharmonic oscillation frequency is several times smaller than the switching frequency (such as in the interleaved PFC case). The current loop design guidelines are given for both boost PFC with ACM control and flyback PFC with charge control. Trade-offs in current loop stability margin and line current distortion are also studied.

Depending on the application, one control scheme may be more suitable than the others. PCM control provides good dynamic performance and stability margins for dc-dc converters. Its cycle-by-cycle peak current limiting ability and easy-to-implement features also make it an attractive control scheme for dc-dc converters. ACM control is more suitable for applications where the average inductor current needs to be controlled, as in battery charger and boost PFC control. ACM control also provides good noise immunity and average current sharing ability. Charge control can accurately control the average switch current of a PWM converter; hence, it is the best choice for buck and flyback PFC control.

The small-signal characteristics of discontinuous conduction-mode operation PWM converter with both average current-mode and charge controls are not studied in the dissertation. These studies are useful for both dc-dc converter

and power factor correction circuit control applications. Furthermore, studies should be continued on finding more applications for both controls.

Appendix A. DERIVATIONS FOR AVERAGE CURRENT-MODE CONTROL

A.1 Introduction

This appendix provides some derivations for Chapter II. It includes the turn-on time slope of the current compensator output, feedback and feedforward gains of the small-signal model, and the damping factor of the double pole $F_h(s)$ of the small-signal characteristics when current loop is closed. The derivations are carried in a general way, so that the obtained results are valid for all PWM converters.

A.2 Derivation of S'_n

The current loop compensation network of ACM control and its input and output waveforms are shown in Fig. A.1. The gain of the circuit is:

$$G_c(s) = -\frac{\omega_i\,(1+\frac{s}{\omega_z})}{s\,(1+\frac{s}{\omega_p})}, \qquad (A.1a)$$

where

$$\omega_i = \frac{1}{R_i\,(C_{fp}+C_{fz})}, \qquad (A.1b)$$

$$\omega_z = \frac{1}{R_f\,C_{fz}}, \qquad (A.1c)$$

$$\omega_p = \frac{C_{fz}+C_{fp}}{R_f\,C_{fz}\,C_{fp}}. \qquad (A.1d)$$

The on-time expression of the sensed inductor ripple current is as follows:

$$i_L(t) = S_n\,t, \qquad (A.2)$$

where S_n is the sensed inductor current on-time slope. The ripple of the output of the compensation network, $\tilde{i}_L(t)$, during the on-time can be obtained:

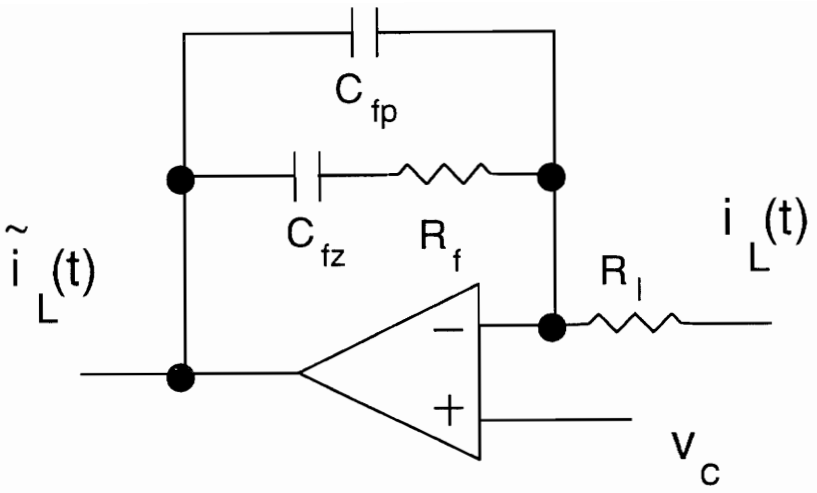

(a) current loop compensator

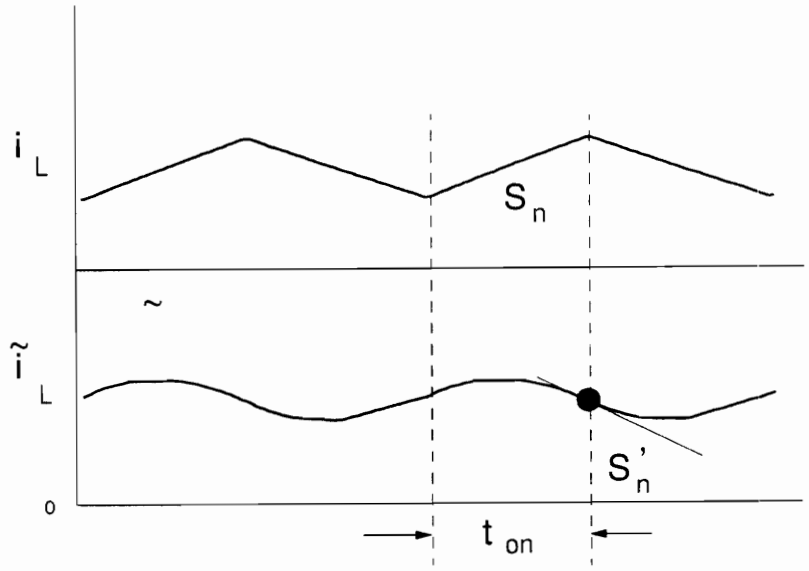

(b) input and output waveforms

Figure A.1. Current loop compensator and its input and output waveforms: *The output of the current compensator, $\tilde{i}_L(t)$ and the sawtooth ramp determine the control. Hence the modulator gain is determined by the sawtooth ramp slope and the slope of $\tilde{i}_L(t)$ at time T_s.*

$$\tilde{i}_L(t) = L^{-1}\{G_c(s)i_L(s)\}$$
$$= -S_n\left[\frac{\omega_i}{2}t^2 + \omega_i\left(\frac{1}{\omega_z} - \frac{1}{\omega_p}\right)t - \frac{\omega_i}{\omega_p}\left(\frac{1}{\omega_z} - \frac{1}{\omega_p}\right)\left(1 - e^{-\omega_p t}\right)\right] \quad (A.3)$$

S'_n is the absolute value of the slope of $\tilde{i}_L(t)$ at $t = DT_s$:

$$S'_n = |\tilde{i}_L'(DT_s)| = S_n\,\xi, \quad (A.4a)$$

where

$$\xi = \omega_i D\,T_s + \omega_i\left(\frac{1}{\omega_z} - \frac{1}{\omega_p}\right)\left(1 - e^{-\omega_p DT_s}\right). \quad (A.4b)$$

A.3 Derivation of Feedback and Feedforward Gains

To derive the feedback and feedforward gains, k_r and k_f, for all PWM converters employing ACM control, the describing function for the average inductor current in terms of the control voltage and operation conditions, derived in 2.2.2, needs to be perturbed with respect to the input and output voltages, separately. Then the input voltage and the output voltage to the average inductor current transfer functions are obtained, respectively. The same transfer functions can also be obtained from the small-signal model shown in Fig. 2.12, with k_r and k_f as the unknown parameters. By comparing these functions, k_r and k_f can be obtained.

All the PWM topologies with current-mode controls have something in common. When the switch is turned on, the dc voltage, V_{on}, is applied across the inductor. When the switch is off, the dc voltage, V_{off}, is applied to the inductor. It means that a generic current-mode cell [20,37] can be used to represent all the PWM converters employing current-mode control. The small-signal model for the generic current-mode cell is shown in Fig. A.2. It is unique for all PWM converters with current-mode controls.

Since all PWM topologies with current-mode controls have a uniform structure, it is wise to perturb the describing function with respect to v_{on} and v_{off}, and then to construct a model which feedforwards $\hat{v}_{on}$ and $\hat{v}_{off}$ through the feedforward gains, k'_r and k'_f. The constructed model for ACM control is shown in Fig. A.3. k'_r and k'_f are invariant for all PWM topologies. The purpose of introducing this generic model is to simplify the derivations of k_r and k_f for different PWM topologies. Since for any PWM converter, the input and output voltages are linear combinations of V_{on} and V_{off}, the k_r and k_f are then linear combinations of k'_r and k'_f.

The describing function derived in Chapter II is rewritten here:

$$K\,(R_i\,i_L - v_c) = -\,S_e\,dT_s, \qquad (A.5a)$$

where d can be expressed as a function of v_{on} and v_{off}:

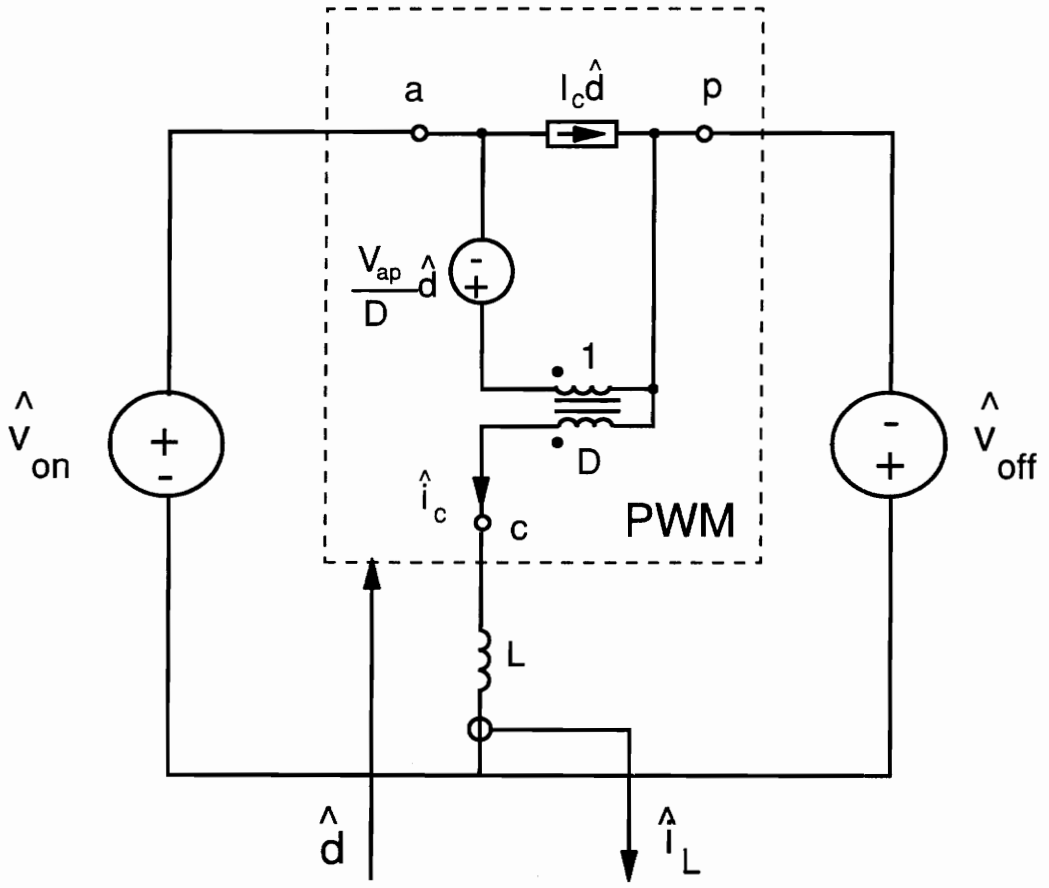

Figure A.2. Small-signal model for the generic current cell: *The input and output voltages of the generic current cell are $\hat{v}_{on}$ and $\hat{v}_{off}$, respectively. They are linear combinations of the input and output voltages of any PWM converter. $\hat{i}_L$ is the output of the cell which is used as the feedback signal. The cell is controlled by duty cycle $\hat{d}$*

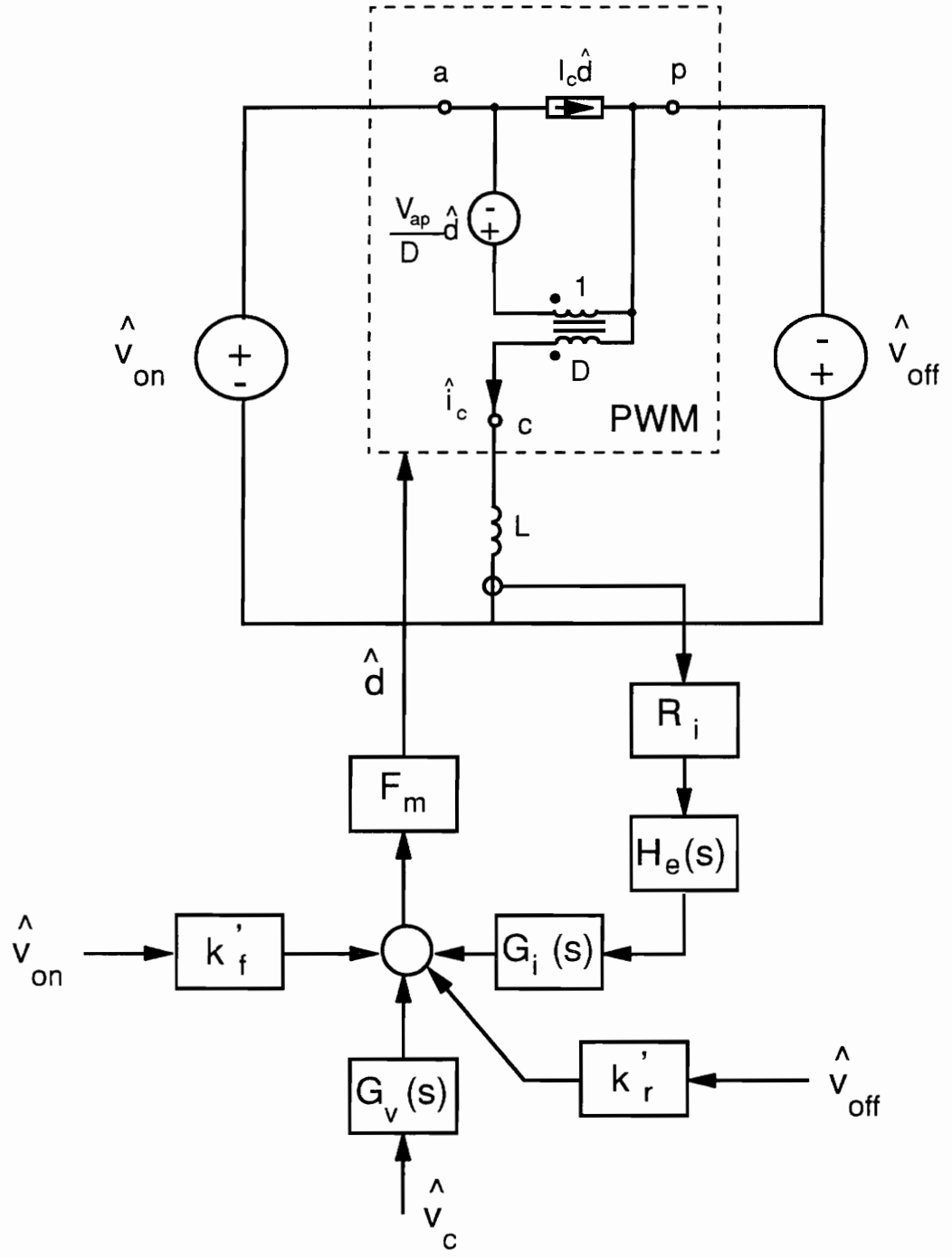

Figure A.3. Small-signal model of ACM control with generic current cell: *By replacing the power stage with the generic current cell model and using k'_r and k'_f as the feedforwad gains, a generic small-signal model for ACM control is obtained. The model is valid at both low- and high-frequencies.*

$$d = \frac{v_{off}}{v_{on} + v_{off}} . \qquad (A.5b)$$

By perturbing Eq. (A.5) against v_{on} and v_{off}, respectively, the $\hat{v}_{on}$ and $\hat{v}_{off}$ to $\hat{i}_L$ transfer functions can be obtained.

$$\frac{K R_i \hat{i}_L}{\hat{v}_{on}} = \frac{S_e D T_s}{V_{ap}} , \qquad (A.6)$$

and

$$\frac{K R_i \hat{i}_L}{\hat{v}_{off}} = -\frac{S_e D' T_s}{V_{ap}} , \qquad (A.7)$$

where

$$V_{ap} = V_{on} + V_{off} \qquad (A.8)$$

is the voltage drop across active and passive switches [22].

The same transfer functions can also be obtained from the small-signal model shown in Fig. A.3, with k'_r, k'_f as the unknowns. At low-frequency, $G_i(s)$ and $G_c(s)$ are large gain, K, and $H_e(s)$ equal to one:

$$\frac{K R_i \hat{i}_L}{\hat{v}_{on}} = \frac{D}{F_m V_{ap}} + k'_f , \qquad (A.9)$$

$$\frac{K R_i \hat{i}_L}{\hat{v}_{off}} = -\frac{D'}{F_m V_{ap}} + k'_r. \qquad (A.10)$$

By comparing Eq. (A.6-A.10), k'_r and k'_f are obtained:

$$k'_f = -\frac{D T_s S'_n}{V_{ap}}, \qquad (A.11)$$

and

$$k'_r = \frac{D' T_s S'_n}{V_{ap}}. \qquad (A.12)$$

For any PWM converter, the inductor current on-time slope is:

$$S_n = \frac{R_i V_{on}}{L} = \frac{R_i D' V_{ap}}{L}. \qquad (A.13)$$

By substituting Eqs.(A.4), (A.13) into Eqs. (A.11), (A.12), we have:

$$k'_f = -\frac{D' D T_s R_i}{L}\ \xi, \qquad (A.14)$$

and

$$k'_r = \frac{D'^2 T_s R_i}{L}\ \xi. \qquad (A.15)$$

As mentioned before, the on-time and off-time voltages of a PWM converter are the linear combinations of the input and output voltage of the converter. The relationships between these voltages are summarized in Table A.1 for three basic PWM converters. The feedforward and feedback gains for these three converters are listed in Table A.2.

Table 3. Input and Output Voltage Relationship

	BUCK	BOOST	BUCK/BOOST
V_{on}	$V_g - V_o$	V_g	V_g
V_{off}	V_o	$V_o - V_g$	V_o
k_f	k'_f	$k'_f - k'_r$	k'_f
k_r	$-k'_f + k'_r$	k'_r	k'_r

Table 4. Feedforward and Feedback Gains for Average Current-Mode Control

	BUCK	BOOST	BUCK/BOOST
k_f	$-\frac{R_i D D' T_s}{L}\,\xi$	$-\frac{R_i D' T_s}{L}\,\xi$	$-\frac{R_i D D' T_s}{L}\,\xi$
k_r	$\frac{R_i D' T_s}{L}\,\xi$	$\frac{R_i D'^2 T_s}{L}\,\xi$	$\frac{R_i D'^2 T_s}{L}\,\xi$

A.4 Derivation of Q_p

To derive the damping factor Q_p for the double pole in all transfer functions of ACM control with current loop closed, the small-signal model shown in Fig. A.3 is used. By ignoring k_r, we have:

$$\hat{d} = -F_m[R_i G_i(s) H_e(s)\,\hat{i}_L + G_c(s)\hat{v}_c], \qquad (A.16a)$$

and

$$\hat{i}_L = G_{id}(s)\hat{d}, \qquad (A.16b)$$

where $G_{id}(s)$ is the power stage duty cycle-to-inductor current transfer function. Since the double pole locates at high frequency, the model in Fig. A.3 can be simplified. At high frequency,

$$G_i(s) = \frac{\omega_i}{\omega_z}, \qquad (A.17a)$$

$$G_c(s) = \frac{\omega_i}{\omega_z}\frac{1}{(1+\frac{s}{\omega_p})}, \qquad (A.17b)$$

and

$$\hat{i}_L \simeq \frac{V_{ap}}{s\,L}\,\hat{d}. \qquad (A.17c)$$

From Eqs. (A.16-17), the control-to-inductor current transfer function high-frequency expression is obtained:

$$\frac{\hat{i}_L}{\hat{v}_c} \simeq \frac{1}{F_m R_i \frac{\omega_i}{\omega_z}\left[\frac{s\,L}{V_{ap} F_m R_i}\frac{\omega_z}{\omega_i} + H_e(s)\right]\left(1 + \frac{s}{\omega_p}\right)}. \qquad (A.18)$$

The sampling gain $H_e(s)$ is given by Eq. (2.2), and the modulator gain is given by Eqs. (2.5). By letting:

$$\frac{s\,L}{V_{ap} F_m R_i}\frac{\omega_z}{\omega_i} + H_e(s) = 1 + \frac{s}{\omega_n Q_p} + \frac{s^2}{\omega_n^2}, \qquad (A.19)$$

Q_p can be solved from Eq. (A.19):

$$Q_p = \frac{1}{\pi\left(\frac{LF_s}{V_{ap} R_i F_m}\frac{\omega_z}{\omega_i} - \frac{1}{2}\right)}. \qquad (A.20)$$

The modulator gain can be rewritten in the following form:

$$F_m = \frac{1}{S_n m'_c T_s}, \qquad (A.21a)$$

where

$$m'_c = \xi + \frac{S_e}{S_n}. \qquad (A.21b)$$

Substitute Eq (A.13) into Eq. (A.21a) and then Eq. (A.21a) into Eq. (A.20):

$$Q_p = \frac{1}{\pi(D'm'_c \frac{\omega_z}{\omega_i} - \frac{1}{2})}. \qquad (A.22)$$

The obtained Q_p is general for all PWM converters

Appendix B. DERIVATIONS FOR CHARGE CONTROL

B.1 Introduction

This appendix contains derivations for Chapter III. It includes feedback and feedforward gains, and the damping factor of the double pole $F_h(s)$ of charge control. The derivations are carried in a general way so that the obtained results are valid for all PWM converters.

B.2 Derivation of Feedback and Feedforward Gains

To derive the feedback and feedforward gains, k_r and k_f, for all PWM converters employing charge control, the describing function for the average inductor current in terms of the control voltage and operation conditions, derived in 3.2.2, needs to be perturbed with respect to input and output voltages, separately. Then, the input voltage and output voltage to average inductor current transfer functions can be obtained, respectively. The same transfer functions can also be obtained from the small-signal model shown in Fig. 3.8, with k_r and k_f as the unknown parameters. By comparing these functions, k_r and k_f can be obtained.

To simplify the derivation, the same approach as in Appendix A. is adopted. The generic current cell model, shown in Fig. A. 2, is used for charge control. For charge control, the small-signal model with k'_r and k'_f as the feedforward gains is shown in Fig. B.1.

The describing function derived in Chapter III is rewritten here:

$$v_c = \frac{1}{C_T} i_L \, dT_s, \qquad (B.1)$$

where v_c and i_L denote the average quantity of $v_c(t)$ and $i_L(t)$. Perturbing Eq. (B.1) with respect to i_L and v_{on}, with v_c being fixed, we have:

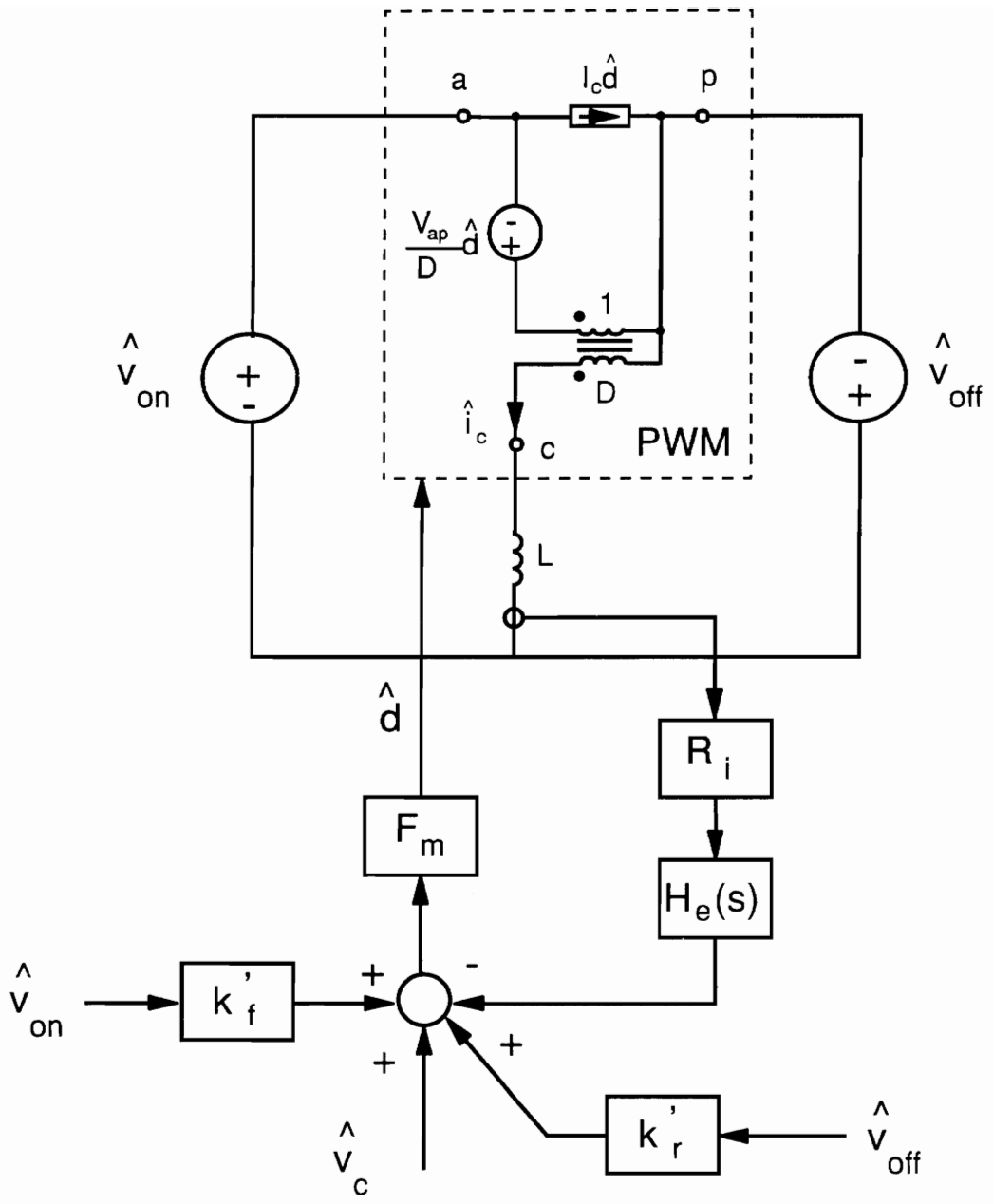

Figure B.1. Small-signal model of charge control with generic current cell: *By replacing the power stage with the generic current cell model and using k'_r and k'_f as the feedforward gains, a generic small-signal model for charge control is obtained. The model is valid at both low- and high-frequencies.*

$$\frac{\hat{i}_L}{\hat{v}_{on}} = \frac{I_L}{V_{ap}}, \tag{B.2}$$

where I_L is the average inductor current of PWM converters. Similarly, by perturbing Eq. (B.1) with respect to i_L and v_{off}, we have:

$$\frac{\hat{i}_L}{\hat{v}_{off}} = -\frac{D' I_L}{D V_{ap}}. \tag{B.3}$$

The same transfer function can also obtained from Fig. B.1:

$$\frac{\hat{i}_L}{\hat{v}_{on}} = \frac{1}{R_i}\left[\frac{D}{F_m V_{ap}} + k'_f\right], \tag{B.4}$$

and

$$\frac{\hat{i}_L}{\hat{v}_{off}} = \frac{1}{R_i}\left[-\frac{D'}{F_m V_{ap}} + k'_f\right] \tag{B.5}$$

k'_f can be solved from Eq. (B.2), (B.4):

$$k'_f = \frac{R_i I_L}{V_{ap}} - \frac{D}{F_m V_{ap}}. \tag{B.6}$$

For charge control without external ramp, we have:

$$F_m = \frac{D}{I_{Lp} R_i}, \tag{B.7}$$

where I_{Lp} is the peak inductor current of PWM converters. From Eq. (B.6-7):

$$\begin{aligned} k'_f &= \frac{R_i}{V_{ap}} (I_L - I_{Lp}) \\ &= \frac{R_i}{V_{ap}} \left(- \frac{V_{on} D T_s}{2L} \right). \\ &= - \frac{R_i D D' T_s}{2L} \end{aligned} \tag{B.8}$$

By comparing Eq. (B.3) and (B.5), k'_r is solved:

$$\begin{aligned} k'_r &= - \frac{R_i D' I_L}{V_{ap} D} + \frac{D'}{V_{ap} F_m} \\ &= \frac{R_i D'}{V_{ap} D} (I_{Lp} - I_L) \\ &= \frac{R_i D'^2 T_s}{2L} \end{aligned} \quad . \tag{B.9}$$

The relationships between input and output voltages, and V_{on}, V_{off} of PWM converters are listed in Table 3. According to Table 3, k_r and k_f for three basic PWM converters are obtained. They are listed in Table 5.

Table 5. Feedforward and Feedback Gains for Charge Control

	BUCK	BOOST	BUCK/BOOST
k_f	$-\frac{R_i D D' T_s}{2L}$	$-\frac{R_i D' T_s}{2L}$	$-\frac{R_i D D' T_s}{2L}$
k_r	$\frac{R_i D' T_s}{2L}$	$\frac{R_i D'^2 T_s}{2L}$	$\frac{R_i D'^2 T_s}{2L}$

B.3 Derivation of Q_p

To derive the damping factor Q_p for the double pole in control-to-output voltage and control-to-inductor current gains, the small-signal model shown in Fig. 3.8 is used. From Fig. 3.8:

$$\hat{d} = -F_m R_i H_e(s)\hat{i}_L + \hat{v}_c \qquad (B.10a)$$

and

$$\hat{i}_L = G_{id}(s)\,\hat{d}. \qquad (B.10b)$$

At high-frequency:

$$\hat{i}_L \simeq \frac{V_{ap}}{s\,L}\,\hat{d}. \tag{B.11}$$

From Eqs. (B.10) and (B.11):

$$\frac{\hat{i}_L}{\hat{v}_c} \simeq \frac{1}{F_m R_i[\frac{s\,L}{V_{ap} F_m R_i} + H_e(s)]}. \tag{B.12}$$

Let:

$$\frac{s\,L}{V_{ap} F_m R_i} + H_e(s) = 1 + \frac{s}{\omega_n Q_p} + \frac{s^2}{\omega_n^2}. \tag{B.13}$$

If there is no external ramp added:

$$F_m R_i = \frac{D}{I_{Lp}}. \tag{B.14}$$

Then Q_p is solved from Eq. (B.13)

$$Q_p = \frac{1}{\pi(\frac{L F_s I_{Lp}}{D V_{ap}} - \frac{1}{2})}, \tag{B.15}$$

where:

$$I_{Lp} = I_L + \frac{V_{on}}{2\,L} D T_s. \tag{B.16}$$

By substituting Eq. (B.16) to Eq. (B.15):

$$Q_p = \frac{1}{\pi(\frac{LF_sI_L}{DV_{ap}} - \frac{D}{2})} = \frac{1}{\pi(\frac{LF_s}{R_e} - \frac{D}{2})}, \quad (B.17a)$$

where

$$R_e = \frac{DV_{ap}}{I_L}; \quad (B.17b)$$

for buck converter:

$$R_e = R; \quad (B.17c)$$

for boost converter:

$$R_e = DD'R; \quad (B.17d)$$

and for buck/boost converter:

$$R_e = D'R. \quad (B.17e)$$

If there is an external ramp added to the system, we have:

$$F_m R_i = \frac{D}{I_{Lp} + S_e C_T} . \qquad (B.18)$$

Substituting Eq. (B.18) to (B.13), Q_p can be solved:

$$Q_p = \frac{1}{\pi\left(\frac{LF_s}{R_e} - \frac{D}{2} + \frac{LF_s C_T S_e}{V_{cp}}\right)}, \qquad (B.19)$$

where V_{cp} is the voltage from common terminal to passive terminal of the three-terminal PWM switch [22].

Appendix C. LOSS DERIVATION FOR CCM AND DCM FLYBACK PFC

C.1 Introduction

In this appendix, the general loss expressions for both CCM and DCM operation flyback PFCs are derived. The expressions for calculating rms, peak and average currents are also derived.

C.2 RMS, Peak and Average Currents of CCM Flyback PFC

The line current and the input current of CCM operation flyback converter are shown in Fig. C.1. For PFC circuit, the peak and average currents vary with the time, since they are functions of line voltage. From Fig.C.1 we have:

$$I_1(t) = I_x(t) - \frac{1}{2}\Delta I(t), \tag{C.1}$$

and

$$I_2(t) = I_x(t) + \frac{1}{2}\Delta I(t), \tag{C.2}$$

where

$$I_x(t) = \frac{I_p \sin(\omega_l t)}{D}(t), \tag{C.3}$$

and

$$\Delta I(t) = \frac{V_p \sin(\omega_l t) D(t) T_s}{L}, \tag{C.4}$$

and

$$D(t) = \frac{n\,V_o}{n\,V_o + V_p\,\sin(\omega_l t))}, \tag{C.5}$$

where V_p and I_p are peak line voltage and current, respectively. The squire of the rms primary current averaged over a line cycle equals:

$$(I'_{prms})^2 = \frac{2}{T_l}\int_0^{\frac{T_l}{2}} D(t) I_x^2(t)\,dt. \tag{C.6}$$

The squire of the rms secondary current averaged over a line cycle is:

$$(I'_{srms})^2 = \frac{2}{T_l}\int_0^{\frac{T_l}{2}} (1 - D(t))(n I_x(t))^2\,dt. \tag{C.7}$$

The average primary current over the line cycle is:

$$I'_{pave} = \frac{2}{T_l}\int_0^{\frac{T_l}{2}} D(t) I_x(t)\,dt. \tag{C.8}$$

The average secondary current over the line cycle is:

$$I'_{save} = \frac{2}{T_l}\int_0^{\frac{T_l}{2}} (1 - D(t)) n I_x(t)\,dt. \tag{C.9}$$

C.3 RMS, Peak and Average Currents of DCM Flyback PFC

The primary and secondary current waveforms of DCM operation flyback converter are shown in Fig. C.2. For PFC circuit, the peak and average currents vary with the time, since they are functions of line voltage. From Fig.C.1 we have:

$$I_1(t) = 0, \tag{C.10}$$

and

$$I_2(t) = \frac{V_p \sin(\omega_l t) D T_s}{L}, \tag{C.11}$$

where

$$D = \frac{nV_o}{V_p}\sqrt{2K}, \tag{C.12}$$

and

$$K = \frac{2L}{R_{\min} T_s \eta}. \tag{C.13}$$

Both primary and secondary rms currents averaged over a line cycle are given in [31]. They are:

$$I'_{prms} = \frac{V_p D T_s}{L} \sqrt{\frac{D}{6}}, \tag{C.14}$$

and

$$I'_{srms} = \frac{2}{3} (2K)^{0.75} \frac{V_o T_s n^2}{L} \sqrt{\frac{1}{\pi}}. \tag{C.15}$$

The average primary current over the line cycle is:

$$I'_{pave} = \frac{2}{T_l} \int_0^{\frac{T_l}{2}} \frac{D^2 T_s V_p \sin(\omega_l t)}{2L} \, dt, \tag{C.16}$$

and the average secondary current over the line cycle is:

$$I'_{save} = \frac{2}{T_l} \int_0^{\frac{T_l}{2}} \frac{D_2^2(t) T_s V_o}{2L} \, dt, \tag{C.17}$$

where

$$D_2(t) = D \frac{V_p \sin(\omega_l t)}{n V_o}. \tag{C.18}$$

C.4 Loss Expressions for CCM and DCM Flyback PFC

For both CCM and DCM operation flyback PFCs, the voltage across the active switch at off-time is:

$$V_{ds}(t) = V_p \sin(\omega_l t) + nV_o, \tag{C.19}$$

and the voltage across the rectifier diode is:

$$V_d(t) = V_o + \frac{1}{n} V_p \sin(\omega_l t). \tag{C.20}$$

Both CCM and DCM operations have the same equations for loss calculation. When MOSFET is used as the switch, the conduction loss, P_M^{on}, and switching loss, P_M^s, are as follows:

$$P_M^{on} = R_{ds} \ (I_{prms}^l)^2, \tag{C.21}$$

and

$$P_M^s = \frac{2}{T_l} \int_0^{\frac{T_l}{2}} \frac{V_{ds}(t) f_s}{6} (I_1(t) t_r + I_2(t) t_f) \, dt + \frac{2}{T_l} \int_0^{\frac{T_l}{2}} C_{ds} V_{ds}(t) dt. \tag{C.22}$$

If IGBT is used as the switching device, the conduction loss, P_l^{on}, and switching loss, P_l^s, are as follows:

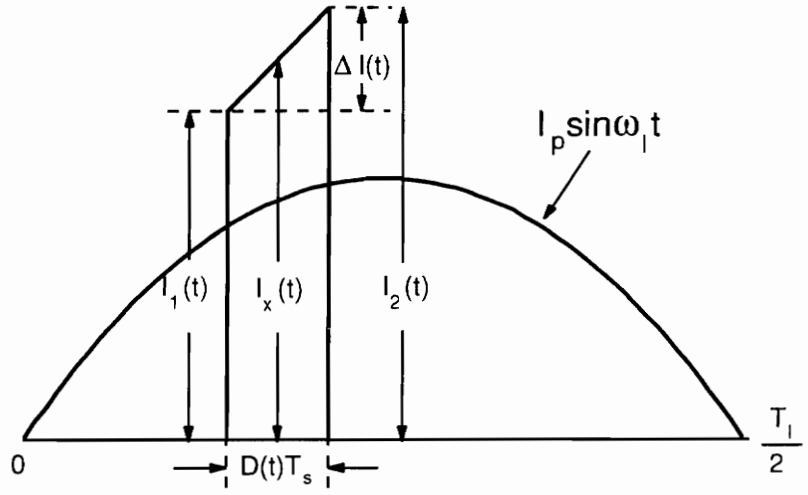

(a) CCM operation

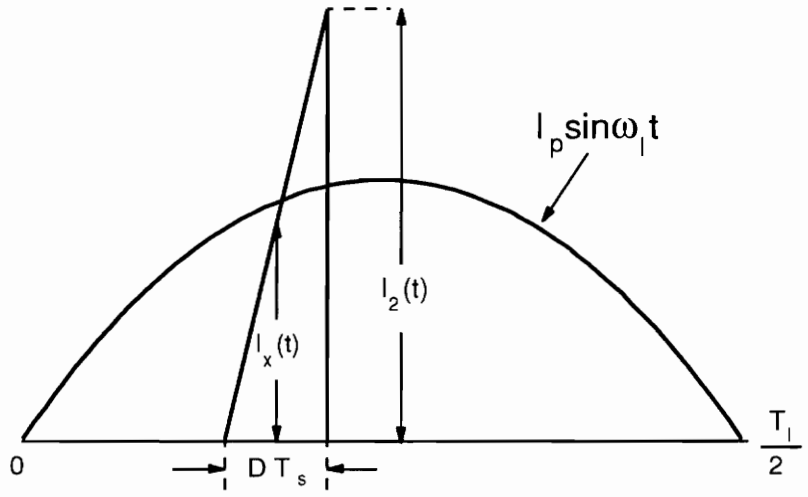

(b) DCM operation

Figure C.1. Input current of both CCM and DCM flyback PFCs: *For both DCM and CCM operation flyback PFCs, the peak, average, and rms input currents are functions of line voltage.*

$$P_l^{on} = V_{ces}\, I_{pave}^{l}, \tag{C.23}$$

and

$$P_l^{s} = \frac{2}{T_l}\int_0^{\frac{T_l}{2}} \frac{ETS\, V_{ds}(t)\, I_2(t)\, f_s}{V_{CEO}\, I_C}\, dt. \tag{C.24}$$

The diode loss is the sum of conduction loss, P_D^{on}, switching loss, P_D^{s}, and reverse recovery loss, P_D^{rr}:

$$P_D^{on} = V_d\, I_{save}^{l}; \tag{C.25}$$

$$P_D^{s} = \frac{2}{T_l}\int_0^{\frac{T_l}{2}} \frac{V_d(t)\, f_s}{6}\,(n\, I_2(t)\, t_{dr} + n\, I_1(t)\, t_{df})\, dt; \tag{C.26}$$

$$P_D^{rr} = \frac{2}{T_l}\int_0^{\frac{T_l}{2}} \frac{V_d(t)\, n\, I_2(t)\, f_s\, t_{rr}}{4}\, dt. \tag{C.27}$$

The inductor core loss is a function of switching frequency, flux, and core volume [38]:

$$P_C = k_\lambda \left(\frac{\Delta B}{2}\right)^{k_\alpha} f_s^{k_\beta}\, V_e, \tag{C.28}$$

where V_e is the core volume. Since ΔB is a function of the input voltage, it varies in a line cycle:

$$\Delta B(t) = \frac{V_p \sin(\omega_l t)\, D(t)\, T_s}{N_p A_e}. \tag{C.29}$$

The average core loss over half line cycle is:

$$P_C = \frac{2}{T_l} \int_0^{\frac{T_l}{2}} k_\lambda \left(\frac{\Delta B(t)}{2}\right)^{k_\alpha} f_s^{k_\beta} V_e \, dt. \tag{C.30}$$

The copper loss of the transformer is as follows:

$$P_W = (I'_{srms})^2 R_p + (I'_{drms})^2 R_s, \tag{C.31}$$

where R_p and R_s are primary and secondary winding resistances, respectively.

The total loss of flyback PFC when MOSFET is used as the switch is:

$$P_M = P_M^{on} + P_M^{s} + P_D^{on} + P_D^{s} + P_D^{rr} + P_C + P_W. \tag{C.32}$$

The total loss of flyback PFC when IGBT is used as the switch is:

$$P_I = P_I^{on} + P_I^{s} + P_D^{on} + P_D^{s} + P_D^{rr} + P_C + P_W. \tag{C.33}$$

REFERENCES

[1] A. Capel, G. Ferrante, D. O'Sullivan, A. Weinberg, "Application of the Injected Current Model for the Dynamic Analysis of Switching Regulators with the New Concept of LC3 Modulator," IEEE Power Electronics Specialists Conference Record, pp, 135-147, 1978.

[2] C. W. Deisch, "Simple Switching Control Method Changes Power Converter into a Current Source," IEEE Power Electronics Specialists Conference Record, pp, 300-306, 1978.

[3] F. C. Schwarts, "Analog Signal to Discrete Time Interval Converter (ASDTIC)," U. S. Patent 3,659,184, 1972.

[4] A. D. Schoenfeld, Y. Yu, "ASDTIC Control and Standardized Interface Circuit Applied to Buck, Boost, and Buck-Boost DC-to-DC Power Converters," NASA Report NASA CR-121106, Prepared by TRW System, Feb., 1973.

[5] Y. Yu, R. I. Iwens, F. C. Lee, L. Y. Inouye, "Development of a Standardized Control Module for DC-DC Converters," NASA Contract Report, NASA-18918, August 30, 1977.

[6] B. L. Wilkinson, J. Mandelcorn, "Unity Power Factor Supply," U. S. Patent #4,677,366, June, 1987.

[7] D. O'Sullivan, H. Spruyt and A. Crausaz, "PWM Conductance Control," IEEE Power Electronics Specialists Conference Record, pp 351-359, 1988.

[8] L. H. Dixon, "Average Current-Mode Control of Switching Power Supplies," Unitrode Power Supply Design Seminar Manual, SEM-700, 1990.

[9] A. Capel, "Charge Controlled Conversion Principle in DC/DC Regulators Combines Dynamic Performance and High Output Power," IEEE Power Electronics Specialists Conference Record, pp 264-276, 1979.

[10] I. Cohen, "Adaptive Control Method for Power Converter," US and Foreign Patents Pending, 1990.

[11] P. Maranesi, G. Naummi, "Computer-Aided Identification of the Small-Signal Model of Power-Electronics Systems," IEEE Power Electronics Specialists Conference Record, pp 62-65, 1991.

[12] S. P. Hsu, A. R. Brown, L. Rensink and R. D. Middlebrook, " Modelling and Analysis of Switching DC-to-DC Converter in Constant-Frequency Current-Programmed Mode," IEEE Power Electronics Specialists Conference Record, pp 284-301, 1979.

[13] F. C. Lee, Y. Yu, and M. F. Mahmond, "A Unified Analysis and Design Procedure for a Standardized Control Module for DC-DC Switching Regulators," IEEE Power Electronics Specialists Conference Record, pp 284-301, 1980.

[14] R. D. Middlebrook, "Topics in multiple-loop regulators and current-mode programming," IEEE Power Electronics Specialists Conference Record, 1985, pp. 716-732.

[15] A. R. Brown and R. D. Middlebrook, "Sampled-Data Modeling of Switching Regulators," IEEE Power Electronics Specialists Conference Record, pp 349-369, 1981.

[16] A. R. Brown, "Topics in the Analysis, Measurement, and Design of High-Performance Switching Regulators," Ph. D. Dissertation, California Institute of Technology, May 15, 1981.

[17] R. B. Ridley, "Continuous-Time Model for Current-Mode Control of Power Converters," IEEE Trans. on Power Electronics, Vol. 6, No. 2, April 1991.

[18] R. B. Ridley, "A New Small-Signal Model for Current-Mode Control," Ph.D. Dissertation, Virginia Polytechnic Institute and State University, Nov. 27, 1990.

[19] G. C. Verghese, C. A. Bruzos, K. N. Mahabir, "Average and Sampled-Data Models for Current Mode Control: A Reexamination," IEEE Power Electronics Specialists Conference Record, 1989.

[20] V. Vorperian, "Analysis of current-mode controlled PWM converters using the model of the current-controlled PWM switch," Power Conversion and Intelligent Motion Conference, PCIM'90, 1990.

[21] A. S. Kislovski, "Small-Signal Low-Frequency Analysis of a Buck Type PWM Conductance Controller," IEEE Power Electronics Specialists Conference Record, pp 88-95, 1990.

[22] A. S. Kislovski, R. Redl, N. O. Sokal, *Dynamic Analysis of Switching-mode DC/DC Converters* , New York, Van Nostrand Reinhold, 1991.

[23] V. Vorperian, "Simplified Analysis of PWM Converters Using the Model of the PWM Switch: Part I and II," IEEE Transactions on Aerospace and Electronic Systems, Vol. 26, No. 3, pp 490-505, May 1990.

[24] B. H. Cho, F. C. Lee, "Measurement of Loop Gain with the Digital Modulator," IEEE Power Electronics Specialists Conference, June 18-21, 1984.

[25] W. Tang, C. S. Leu, and F. C. Lee, "Charge Control for Zero-Voltage Switching Multi-Resonant Converters," IEEE Peak-Current-Controlled Boost Power-Factor Correctors," . 229-231.

[26] L. H. Dixon, Jr., "High Power Factor Preregulators for Off-Line Power Supplies," unitrode Power Supply Design Seminar, Manual SEM-600, 1988.

[27] F. C. Lee and M. M. Jovanovic, "Analysis and Design of Power Factor Correction Circuits," Lecture note, VPEC Power Electronics Professional Seminar, November, 1993.

[28] R. Erickson, M. Madigan and S. Singer, "Design of a Simple High-Power-Factor Rectifier Based on the Flyback Converter," IEEE Applied Power Electronics Conference, 1990, pp. 792-801.

[29] Y. Jiang, G. Hua E. Yang and F. C. Lee, "Soft-switching of IGBT's with the help of MOSFET's in bridge-type converters," IEEE Power Electronics Specialists Conference Record, 1993, pp. 151-157.

[30] V. Vlatkovic, D. Borojevic, and F. C. Lee, "Input filter design for power factor correction circuits," Virginia Power Electronics Center Seminar, 1993

[31] M. F. Schlecht, : A Line Interfaced Inverter with Active Control of the Output Current waveform," IEEE Power Electronics Specialists Conference Record, pp. 234-241, 1980.

[32] R. Redl and B. Brian P. Erisman, "Reducing Distortion in 8 Charger System," IEEE Applied Power Electronics Conference, 1994.

[33] C. Zhou and M. M. Jovanovic, "Design Trade-offs in Continuous Current-Mode Controlled Boost Power-Factor Correction Circuits," Proceedings of High-Frequency Power Conversion, pp. 209-220, 1992.

[34] M. M. Jovanovic, "Analysis and Design of Power Factor Correction Circuits," Laboratory manual, VPEC Power Electronics Professional Seminar, November, 1993.

[35] R. Watson, G. Hua, E. X. Yang, W. Tang, and F. C. Lee, "Evaluation of the Active-Clamp Flyback and Isolated Boost Converters as Single-Stage Power Factor Correction Topologies," VPEC fellowship report for Zytec Corp., July, 1993.

[36] W. E. Rippel, "Optimizing Boost Chopper Charger Design," Powcon'79, pp. D1.1-D1.20.

Vita

Wei Tang was born in Nanjing, P. R. China, on October 20, 1959. He received the B.S. and M.S. degrees in electrical engineering from Tsinghua University, Beijing, China, in 1982 and 1985. From 1985 to 1988 he was employed as a Senior Engineer in Sichuan Research Center of Computer Applications, where he worked on computer-aided analysis of electrical and electronic systems.

He began studying at Virginia Polytechnic Institute and State University in 1988, and has been a Graduate Research Assistant since then. He is the recipient of the Lambda Fellowship from 1990 to 1993. He is actively involved in the researches on switching power supply control, modeling and design high-frequency converter, and power factor correction circuit design and control. He is now working as a senior development engineer at Martin Marietta Astro Space in Princeton, New Jersey.